Small-Scale Liquid-State Dynamics in Nanometer Size Devices

Thesis by

David Nicholas Barsic

In Partial Fulfillment of the Requirements

for the Degree of

Doctor of Philosophy

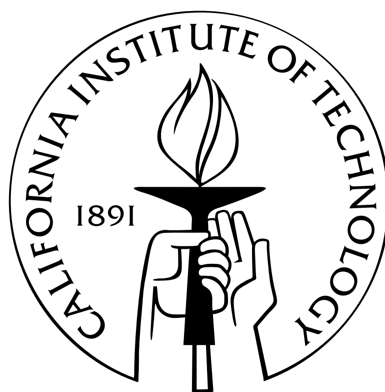

California Institute of Technology

Pasadena, California

2004

(Defended December 12, 2003)

© 2004
David Nicholas Barsic
All Rights Reserved

To my parents, and all of my brothers and sisters.

Acknowledgements

I would like to thank Professor Axel Scherer for his continual guidance, support, and encouragement throughout this work. Also appropriate are thanks to Caltech for providing a stimulating learning environment and excellent facilities, without which this research would not have been possible. To my undergraduate advisers: Helen Na, Peter Schwartz, Norbert Malik, John Robinson, and Winston Chan whose guidance, advice, and support were key to my important career choices.

I would like to thank all of the members of the Nanofabrication lab: Mark Adams, Tom Baehr-Jones Mladen Barbic, Chuan Chen Cheng, Hou-Pou Chou, Guy Derose, Oliver Dial, Theodore Doll, Teresa Emery, Kate Finnigan, Michael Hochberg, Ali Husain, Reynold Johnson, Thomas Krauss, Yves Lassailly, Marko Loncar, George Maltezos, Brett Maune, Marlene Moncada, Terrell Neal, Koichi Okamoto, Oscar Painter, Jörg Schilling, Michelle Vine, Jelena Vucović, Chris Walker, Jeremy Witzens, Joyce Wong, Tomoyuki Yoshie, Zhaoyu Zhang. All of you have made my time at Caltech enjoyable. I am honored to have had the chance to work with and learn from all of you.

I am very much in debt to Bill Bing, Brad Jensen, and Mark Weber who helped me to get back in the groove at times when I was a little off key and behind the beat. To my adopted family in California: Jason, Sabrina, and Alexandra Feldman, thank you for your encouragement and hospitality.

To all of my heroes and role models: Jeff Bergthorson, Will Green, Victor Hristov, Ali Husain, Michael Johnson, Reynold Johnson, Conrad Josias, Reginald Lee, Guillaume Lessard, Shelly Levy-Tzedek, Scott Mehrens, Nick Papadakis, Clara Reis, Miguel Remondes, Joseph Schmidt, Ben Shapiro, and Danielle Svhela; your steady, unfaltering friendship means the world to me.

Without continual support, encouragement, and love of my family none of this would have been possible. Thank you Mom, Dad, Mary, Jayson, Paul, Tessa, Sarah, Angie, and Tony for always being there to support me no matter how great the geographical distances separating us have been.

Abstract

This dissertation will present research on state-of-the-art micrometer- and nanometer-scale machining techniques to fabricate fluid channels with integral sensing electrodes. The motivation for this project is to create new instruments for investigating the behavior and properties of particles or molecules in solution and confined in a fluid channel with cross-sectional dimensions ranging from less than 50 nanometers to one micron.

The objective of this research is to develop techniques for building fluid analysis systems which combine fluid channels with sensing electrodes. Design of physical devices and the measurement circuit are both important steps in accomplishing this task. The design issues necessary for optimizing these aspects are investigated in detail. The size scale of these systems is at the lower limit achievable with current technology. Such devices require critical dimensions of less than 100 nanometers in order to perform measurements on small-scale fluid systems. Applications of this type of system include detection of both the presence and the motion of particles and molecules suspended in the small volume of fluid confined within the fluid channel. The motion of particles in the fluid channel is detected by measuring the change in electrode capacitance as particles move past the electrodes. Typical fluid volumes used in this type of system range from 50 femtoliters ($50x10^{-15}$ l) to less than one femtoliter.

Accomplishing this task required a careful look at the machining techniques for making microscopic devices. The approach is to use lithographic and circuit manufacturing techniques to make small fluid channels on either side of which are sets of electrodes. Existing techniques for making small-scale devices were modified to provide the required performance. In some cases the development of entirely new techniques was necessary.

Contents

Acknowledgements **iv**

Abstract **v**

1 Introduction **1**

1.1 Introduction 1

1.2 Previous Work 2

1.3 Nanometer-Scale Fluid Channels 3

1.4 Pumping Fluid in Nanometer Channels 3

1.5 Nanometer-Scale Sensing Electrodes 4

References 6

2 Lithography Techniques for Nanometer Sized Fluid Channels and Electrodes **9**

2.1 Introduction 9

2.2 Sub-micron Scale Lithography 9

2.3 Photolithography 10

2.4 Shadow Mask Lithography 12

2.5 Electron-Beam Lithography 17

2.6 Electron Image Projection System 21

2.7 Conclusion 21

References 23

3 Fabrication Procedure for Nanometer-Sized Fluid Channels and Electrodes **25**

3.1 Introduction 25

3.2 Thin Film Deposition 25

3.2.1 Thermal Evaporation 25

3.2.2 Electron-Beam Evaporation 26

3.2.3 Sputtering 27
3.3 Etching 28
3.3.1 Reactive Ion Etching 28
3.3.2 Ion-Beam Etching 29
3.3.3 Chemically Assisted Ion-Beam Etching 32
3.4 Surface Cleaning 34
3.4.1 Radio Corproation of America (RCA) Cleaning Process 36
3.5 Conclusion 37
References 38

4 Nanometer Fluid Channels 39
4.1 Introduction 39
4.2 Lithography 40
4.2.1 Electron-Beam Lithography 40
4.3 Etching Nanometer Fluid Channels 42
4.3.1 Transferring the Resist Pattern to the Metal Mask Layer 42
4.3.2 Etching Techniques for Fused Silica Fluid Channels 43
4.3.3 Etching Techniques for Silicon Fluid Channels 45
4.3.4 Etching Techniques for Polymer Channels 45
4.4 Methods of Sealing Nanometer Fluid Channels 50
4.4.1 Surface Preparation 50
4.4.2 Anodic Bonding 52
4.4.3 Fusion Bonding 52
4.4.4 Room Temperature HF Bonding 52
4.5 Imaging Techniques for Fused Silica Fluid Channels 53
4.6 Fluorescent Confocal Microscope Measurements 53
4.7 Conclusion 57
References 58

5 Pumping Liquids at Nanometer-Size Scales 59
5.1 Introduction 59
5.2 Methods of Pumping Fluid in Nanometer Channels 59

5.3 Conditions for Electro-Osmotic Flow (EOF) in Fluid Channels . . . 64
5.3.1 Controlling the Properties of the Electric Double Layer . . . 66
5.3.2 Design of Electro-Osmotic Flow Channels . . . 67
5.3.3 Building the EOF Test Setup . . . 69
5.3.4 Measurement Circuit . . . 70
5.3.5 Experimental Results of the EOF test setup . . . 70
5.4 Conclusion . . . 72
References . . . 74

6 Nanogap Capacitive Sensing Electrodes 78
6.1 Introduction . . . 78
6.2 Nanogap Electrode Overview . . . 78
6.3 Nanogap Electrode Capacitance Calculations . . . 79
6.3.1 Analytic Calculations . . . 79
6.3.2 Finite Element Modeling of the Capacitance Between Two Spheres . . . 81
6.3.3 Finite Element Modeling of the Capacitance Between a Pair of Nanogap Electrodes . . . 82
6.3.4 Change in Nanogap Electrode Capacitance in the Presence of a Nano-particle 84
6.4 Nanogap Electrode Design . . . 85
6.5 Conclusion . . . 87
References . . . 88

7 Electrical Measurement 89
7.1 Introduction . . . 89
7.2 Types of Measurement Circuits . . . 89
7.2.1 Charge/Discharge Technique . . . 89
7.2.2 Oscillator Circuit Methods . . . 91
7.2.3 Inductive-Capacitive Resonator Circuit . . . 91
7.2.4 AC Bridge Circuit . . . 92
7.3 Precision Ratio Transformer Balancing of the AC Capacitance Bridge . . . 93
7.4 Capacitance Measurement Circuit Results . . . 96
7.5 Nanogap Electrode Measurements of Gold Particles in Solution . . . 97

7.6 Conclusion 100
References 102

8 Conclusions **103**

References 104

List of Figures

2.1 Screen printing process: a. The screen is attached to a rigid frame and patterned with pore-blocking paint. b. The screen is held against the work piece. c. Ink is forced through the pores and onto the surface of the work piece. d. The finished result is a pattern in the ink. 10

2.2 Photolithography process steps: a. Align mask with the photoresist coated substrate. b. Bring the mask and substrate together, and expose the photoresist to ultra violet light through the mask. c. Develop the photoresist to remove exposed areas. d. After developing the substrate is ready for subsequent processing steps. 11

2.3 Cross-sectional view of photoresist stripes on a silicon wafer. 11

2.4 Shadow mask process: a. Begin with a photoresist feature. b. Evaporate the metal etch mask at an angle Θ from normal. c. Pattern is transferred into the substrate with a directional etch. d. Final result after removal of the etch mask and photoresist. . . . 12

2.5 Cross-section of a fluid channel made with a shadow mask technique. 13

2.6 Line made using shadow mask technique. 14

2.7 Undercut etch technique: a. Begin with a photoresist feature on top of a mask material. b. Etch exposed mask areas with an isotropic etch to remove the mask material just under the photoresist edges. c. Deposit a second etch mask layer. The overhanging edge of the photoresist will create a small gap. d. Pattern is transferred into the substrate with a directional etch. 15

2.8 Results of the chrome undercutting technique. 16

2.9 Electron-beam lithography system. 18

2.10 a. Electron-beam resist exposure. b. Electron-beam resist development. 18

2.11 Caltech logo machined in a thin gold film on a silicon wafer. 19

2.12 Etched lines in silicon patterned by electron-beam lithography and etching. 20

3.1 a. Thermal evaporation, b. Electron-beam evaporation. 26

3.2 Sputtering. 27
3.3 a. RIE etching chamber. b. Plasma potential profile between the capacitive plates of an RIE system. 29
3.4 Channels etched in a fused silica microscope slide with a C_2F_6 reactive ion etching process. 30
3.5 Schematic representation of an ion beam source. 31
3.6 Schematic of the position of the reactive gas nozzles in the ion beam path. 33
3.7 Oblique view of channels etched into silicon using an XeF_2 assisted ion beam etch. . . 34
3.8 Oblique view of a checkerboard test pattern etched in the top layer of an SOI wafer. . 35

4.1 Line defined in PMMA that has been transferred into the metal etch mask by ion beam etching. 42
4.2 Neutralizing arc damage on a fused silica wafer. 43
4.3 a. Etch profile of fused silica that would result from etching with hydrofluoric acid. b. Etch profile of fused silica resulting from RIE. 44
4.4 Channels in fused silica by a C_2F_6 reactive ion etching process. 44
4.5 Oblique view of the Caltech logo machined in the top layer of an SOI wafer using the same PMMA layer as the electron beam resist and the etch mask during XeF_2 CAIBE processing. 45
4.6 Entrance to a silicon fluid channel. The grid pattern on the left side of the image is a filter structure to prevent large particles from blocking the channel on the right. . . . 46
4.7 Channel defined in a polymethyl methacrylate layer by direct write electron-beam lithography. 47
4.8 Etch profile of *Mylar*® after 10 minutes in an Ar/O_2 reactive ion etch. 48
4.9 Channels etched in *Mylar*®using O_2 and Ar as the gas sources. 49
4.10 Etch profile of *Kapton*® after 10 minutes in an Ar/O_2 reactive ion etch. 50
4.11 Channels etched in *Kapton*® using RIE with O_2 and Ar as the gas sources. 51
4.12 Surface map of channels in silicon dioxide obtained by atomic force microscopy. 54
4.13 Fused silica fluid channels used in fluorescent confocal microscopy measurements. . . . 54
4.14 Fluorescent measurement on beads in the 100 nm wide, 100 nm deep channels shown in Figure 4.13. 55

4.15 Fused silica fluid channels used in fluorescent confocal microscopy measurements. The channels are one micron wide spaced five microns apart. The row of "+" marks across the middle of the image are used in aligning the channels with the confocal microscope. 55

4.16 Fluorescent measurements on 63 nm beads in the 1 μm wide, 100 nm deep channels of Figure 4.15. 56

4.17 Confocal microscope configuration. 56

5.1 Velocity profile of pressure-driven flow in a capillary channel. 61

5.2 Electric double layer adjacent to a surface. 64

5.3 Electro-osmotic flow schematic illustrating water molecules, specifically adsorbed ions and hydrated solute molecules. 65

5.4 Channel etched in a silicon wafer and sealed with PDMS (silicone rubber). 67

5.5 Channel etched in an SOI wafer and sealed with PDMS. 68

5.6 Scanning Electron Micrograph of the Channels. 69

5.7 Photograph of the measurement setup showing PDMS reservoirs and platinum wire electrodes. 71

5.8 Measurement circuit; FC = fluid channel, CE = control electrode, Vg = control voltage to the back side of the silicon chip, Vs = excitation signal from the function generator. 71

5.9 Conductivity of channels with 100 mM NaCl solution (x) and deionized water (o). . . 72

5.10 100 mM $NaSO_4$ solution (x) compared against a control experiment in which no channels were present on the silicon chip (o). 73

6.1 Electron-beam lithography used to define electrodes with a spacing of approximately 50 nm. 80

6.2 Geometry for electrode calculation. 80

6.3 Finite element model results showing the potential distribution between two spheres used to calculate their capacitance of 74.75289 aF. 82

6.4 Finite element model calculation of the potential distribution between two nanogap electrodes and the capacitance of the system. 83

6.5 Finite element model calculation of the potential distribution between two nanogap electrodes with a particle present between them offset 5 nm to the right of center. . . 84

6.6 Calculated capacitance change as a function of particle position between the nanogap electrodes from the finite element model simulations. 85

6.7 Possible configuration in which a reference gap electrode is machined on the chip at the same time as the sensing nanogap electrode. 86
6.8 Configuration using a pair of nanogap electrodes on the same fluid channel. 87
6.9 Example of a device containing a matched pair of nanogap electrodes with one electrode in common. The substrate material is Kapton®. 88

7.1 Charge/discharge circuit proposed by Lord Kelvin. 90
7.2 Oscillator capacitance measurement circuit. 91
7.3 Inductive-capacitive resonator circuit. 92
7.4 a. Wheatstone bridge for comparing resistances, G is a galvanometer. b. AC capacitance bridge for measuring capacitances, D is a phase sensitive detector. 92
7.5 Single decade ratio transformer. 94
7.6 Three decade ratio transformer showing connection scheme for cascading multiple decade transformers. 95
7.7 Ratio transformer balanced capacitance bridge. 95
7.8 Device for testing the capacitance circuit. 96
7.9 Circuit connections for capacitance circuit testing using a precision ratio transformer to balance the AC bridge. 97
7.10 Measurement results of circuit in Figure 7.9. 97
7.11 Circuit connections for capacitance circuit testing using a half bridge configuration with no means of balancing the bridge. 98
7.12 Measurement results of circuit in Figure 7.11. 98
7.13 Device used to test nanogap electrode sensing of gold particles in solution. 99
7.14 Circuit connection for performing measurements on the nanogap electrodes. 99
7.15 Electrical measurement of the nanogap electrodes in Figure 7.13. 100

Chapter 1

Introduction

1.1 Introduction

The objective of this research is to develop techniques for building electro-fluidic systems with dimensions less than 100 nm. These systems will be used to perform analytical measurements of fluid and particle dynamics at nano-scale physical dimensions. The foundation for accomplishing this task is to employ machining techniques typically used for building integrated circuits and micro-electromechanical systems. In this work, these traditional methods are further developed and adapted for making sub-micron fluidic devices. In addition some important new techniques have been developed for both defining features and etching them. The undercut etching technique described in Chapter 2, Section 4 was developed in the course of this research to allow features less than 100 nm to be made using photoresist features larger than 1 μm. One very useful etching technique developed in this research is the xenon diflouride chemically assisted ion beam etching technique presented in Chapter 3, Section 3. This method allows etching of features approaching 10 nm into silicon using only organic resist films as an etch mask.

Chapter 4 reviews the fabrication and design of electrically interrogated nanofluidic systems. Lithography and etching of the flow channels is described for a number of different material systems which are promising candidates for the fabrication of nanochannels.

An additional goal of this work is to develop techniques by which fluids and particles can be moved through sub-micron channels. In micron-scale fluidic systems, the most common method for moving fluid volumes through micro-channels is with pressure driven flow. However many alternative methods are worth exploring. In Chapter 5 various methods of driving fluids are compared for their utility in nanometer size channels.

Electrodes with nanometer spacings are used to detect a number of properties of liquids and

suspended particles in nanofluidic channels. Chapter 6 discusses design issues important for maximizing nanogap electrode sensitivity in response to changing properties of material contained in nanofluidic channels. Chapter 7 discusses the measurement techniques necessary to detect small changes in nanogap electrode capacitance in the presence of metallic particles.

1.2 Previous Work

Nanometer-scale fluid systems have been developed to perform analysis of DNA molecules by studying and characterizing their motion in various devices. Professor Craighead's research group at Cornell studied the dynamics of entropic trapping of DNA in channels less than 100 nm in height [1, 2, 3]. Small pores machined in silicon nitride membranes are used to probe DNA molecules electrically by monitoring the ionic current between solutions on either side of the membrane as DNA molecules pass through the pore [4]. Professor Chu and his colleagues at Stanford have successfully built 10 nm wide fluid channels [5, 6, 7].

Nanometer sized ionic pores in biological membranes control some of the most fundamental processes of all organisms. They are in charge of regulating certain molecular reactions, transporting ions through membranes, and are responsible for electrical signaling in neurons [8]. The micro- and nano-structures of naturally occurring rocks and minerals result in a number of unique transport and diffusion properties. These have in the past been utilized in many different applications, including optics, electronics, filtration, data storage, and x-ray optics [9]. Materials such as carbon nanotubes [10], macroporous silicon [11, 12], and aluminum oxide [13, 14] are currently being used in a number of different experiments and engineering applications. The unique properties of zeolite materials that allow them to function as molecular sieves are a result of a multitude of nanometer size pores in the molecular structure [15, 16, 17, 18].

Methods of moving fluid through small-scale systems is an important area of research that is necessary for the development of commercial devices. Inducing fluid flow by controlling the motion of ions at liquid-solid interfaces is one of the more promising approaches.

Electrodes for sensing properties of the contents of fluid channels have been developed for micron-scale system in order to measure properties of living cells. The device designed and built by Sohn et al. demonstrated the ability to measure small capacitances of individual cells [19]. The externally measured capacitance of a cell was shown to be primarily due to the quantity of DNA in the cell. This was demonstrated by measurements performed on cells at different stages of mitosis.

Many different techniques have been developed for building electrodes with small physical sep-

aration. One approach is to begin with a gap larger than desired and then reduce it by adding material either through electro-deposition or shadow evaporation [20, 21]. An alternative approach is to begin with a fine wire defined lithographically. Gradually etching, breaking, or locally heating this wire eventually leads to the formation of a gap with molecular dimensions. In order to achieve this, it is necessary to monitor the conductivity of the wire during this process [22, 23, 24, 25].

1.3 Nanometer-Scale Fluid Channels

Common physical properties of small channels and pores have a significantly different behavior than their bulk counterparts. Physical and dynamic properties of small channels and pores deviate from governing theory based on macro-scale fluid dynamics [26].

In particular, the non-slip boundary conditions of the Navier-Stokes equations are no longer applicable when one is investigating the fluid dynamics very close to the boundary layer. Developing a platform in which the details of small-scale fluid dynamics can be investigated in an artificially controlled environment may be required to understand small-scale fluid dynamics and help discover new uses for nanoporous materials.

1.4 Pumping Fluid in Nanometer Channels

Classical fluid mechanics describes large-scale fluid dynamics quite accurately. One of the common assumptions is that non-slip conditions occur at the fluid boundary. This assumption is valid in classical fluid dynamics because boundary conditions represent a small fraction of the fluid motion. In the case of nanofluidics, this assumption is no longer valid, because the boundary flow comprises a significant portion of the fluid motion. Thus it is of interest to describe how fluid flow can be described in nanometer-sized channels.

In the case of this research, it is important to understand how particle motion can be influenced by external physical stimuli. Effects that occur naturally, such as Brownian motion, work together with methods for directing and controlling fluid flow. The overall motion is the superposition of all these effects.

Brownian motion refers to the random movement of small particles suspended in a fluid. This motion was first observed by early microscopists [27, 28]. Robert Brown, the Scottish botanist after whom this type of motion is named, took a great interest in this topic. His careful experiments and lucid explanations brought great attention to a phenomena observed by only a few prior to

himself. This motion was initially attributed to particles of biological origin, or “animacules.” Experiments showed that this type of motion can also be observed in particles of non-organic origin suspended in a fluid. Brown writes, “...extremely minute particles of solid matter, whether obtained from organic or inorganic substances, when suspended in pure water, or in some other aqueous fluids, exhibit motions for which I am unable to account, and which from their irregularity and seeming independence resemble in a remarkable degree the less rapid motion of some of the simplest animalcules of infusions [29].” The origin of Brownian motion was not satisfactorily explained until a physical description based on molecular thermal motion was postulated by Albert Einstein [30, 31].

In the experiments presented here, the nanofluidic channel wall proximity reduces the magnitude of observed Brownian movement [32, 33, 34]. In the extreme case, the particles are not able to pass each other in the channels. This situation is referred to as single file diffusion [35]. In the case of particles suspended in fluid channels, hydrodynamic coupling causes a correlation of particle position and velocity [36, 37].

For this research it is necessary to exercise some degree of control over particle motion in the channels. Ideally the particles can flow down the channel at a constant velocity. If this is not the case, the interpretation of the data will become challenging. The methods that can be used to drive the fluid flow at a constant rate include pressure differential [38, 39], temperature gradient [40], viscosity gradient [40], electrolytic gradient (osmotic flow), electrical potential gradient (electro-diffusion) [41], capillary action, acoustic waves [42, 43, 44, 45], rectified Brownian motion [46, 47, 48, 49], optical tweezers [50, 51, 52], and radio frequency electromagnetic wave driven flow.

1.5 Nanometer-Scale Sensing Electrodes

Fluidic channels are constructed to physically confine fluids to a small region in space near electrodes. The electrodes and the fluid between them make up an electrically coupled system used to perform measurements on fluid or particles suspended in fluid.

The fluid channel size scale is below the resolution limit of optical microscopy, yet fluorescent confocal microscopy is capable of detecting the motion of fluorescent particles or molecules in the channels. Electronic techniques such as nuclear magnetic resonance [53], ionic current measurements along the length of the channel [8], and capacitance measurements across the width of the channel [54] have been used to measure properties of fluids and suspended particles in micrometer- and nanometer-sized geometries. This research focuses on measuring changes in capacitance between electrodes on either side of the channel to detect the presence and motion of metallic particles.

By placing electrodes on either side of a nano-channel, it is possible to measure capacitance changes induced by metallic particles as they move past the electrodes. In order to maximize the signal, electrodes must be comparable in size to the metallic particles. In addition, if a high degree of spatial resolution is desired, it is necessary to make the electrodes as narrow as possible, without hindering particle movement.

References

[1] S. W. Turner, A. M. Perez, A. Lopez, and H. G. Craighead. Monolithic nanofluid sieving structures for DNA. *Journal of Vacuum Science and Technology*, 16(6):3835–3840, November/December 1998.

[2] J. Han and H. G. Craighead. Entropic trapping and sieving of long dna molecules in a nanofluidic channel. *Journal of Vacuum Science & Technology A-Vacuum Surfaces and Films*, 17(4):2142–2147, 1999.

[3] M. Foquet, J. Korlach, W. Zipfel, W. W. Webb, and H. G. Craighead. Dna fragment sizing by single molecule detection in submicrometer-sized closed fluidic channels. *Analytical Chemistry*, 74(6):1415–1422, 2002.

[4] Jiali Li, Derek Stein, Claran McMullan, Daniel Branton, Michael J. Aziz, and Jene A. Golovchenko. Ion-beam sculpting at nanometer length scales. *Nature*, 412:166–169, July 2001.

[5] W. L. Li, J. O. Tegenfeldt, L. Chen, R. H. Austin, S. Y. Chou, P. A. Kohl, J. Krotine, and J. C. Sturm. Sacrificial polymers for nanofluidic channels in biological applications. *Nanotechnology*, 14(6):578–583, 2003.

[6] H. Cao, J. O. Tegenfeldt, R. H. Austin, and S. Y. Chou. Gradient nanostructures for interfacing microfluidics and nanofluidics. *Applied Physics Letters*, 81(16):3058–3060, 2002.

[7] H. Cao, Z. N. Yu, J. Wang, J. O. Tegenfeldt, R. H. Austin, E. Chen, W. Wu, and S. Y. Chou. Fabrication of 10 nm enclosed nanofluidic channels. *Applied Physics Letters*, 81(1):174–176, 2002.

[8] Bertil Hille. *Ionic Channels of Excitable Membranes*. Sinauer, second edition, 1992.

[9] Mrs. E. J. Weichel-Moore and Dr. R. J. Potter. Fibre optical properties of ulexite. *Nature*, 200:1163–1165, 1963.

[10] J. Hone, M. C. Llaguno, M. J. Biercuk, A. T. Johnson, B. Batlogg, Z. Benes, and J. E. Fischer. Thermal properties of carbon nanotubes and nanotube-based materials. *Applied Physics A-Materials Science & Processing*, 74(3):339–343, 2002.

[11] J. Schilling, A. Birner, F. Muller, R. B. Wehrspohn, R. Hillebrand, U. Gosele, K. Busch, S. John, S. W. Leonard, and H. M. van Driel. Optical characterisation of 2-D macroporous silicon photonic crystals with bandgaps around 3.5 and 1.3 μm. *Optical Materials*, 17(1-2):7–10, 2001.

[12] J. Schilling, F. Muller, S. Matthias, R. B. Wehrspohn, U. Gosele, and K. Busch. Three-dimensional photonic crystals based on macroporous silicon with modulated pore diameter. *Applied Physics Letters*, 78(9):1180–1182, 2001.

[13] T. Doll, M. Hochberg, D. Barsic, and A. Scherer. Micro-machined electron transparent alumina vacuum windows. *Sensors and Actuators A-Physical*, 87(1-2):52–59, 2000.

[14] T. Doll, J. Vuckovic, M. Hochberg, and A. Scherer. Low-energy electron beam focusing in self-organized porous alumina vacuum windows. *Applied Physics Letters*, 76(24):3635–3637, 2000.

[15] J. M. D. MacElroy and S.-H. Suh. Equilibrium and nonequilibrium molecular dynamics studies of diffusion in model one-dimensional micropores. *Microporous and Mesoporous Materials*, 48:195–202, 2001.

[16] K. Hahn, J. Kärger, and V. Kukla. Single-file diffusion observation. *Physical Review Letters*, 76(15):2762–2765, April 1996.

[17] Volker Kukla, Jan Kornatowski, Dirk Demuth, Irina Girnus, Harry Pfeifer, Lovat V. C. Rees, Stefan Schunk, Klaus K. Unger, and Jörg Kärger. NMR studies of single-file diffusions in unidimensional channel zeolites. *Science*, 272:702–704, May 1996.

[18] Vishwas Gupta, Sririam S. Nivarthi, Alon V. McCormick, and H. Ted Davis. Evidence for single file diffusion of ethane in the molecular sieve $AlPO_4$-5. *Chemical Physics Letters*, 247:596–6000, December 1995.

[19] L. L. Sohn, O. A. Saleh, G. R. Facer, A. J. Beavis, R. S. Allan, and D. A. Notterman. Capacitance cytometry: Measuring biological cells one-by-one. *Biophysical Journal*, 80(1):144A–144A, 2001.

[20] Y. V. Kervennic, H. S. J. Van der Zant, A. F. Morpurgo, L. Gurevich, and L. P. Kouwenhoven. Nanometer-spaced electrodes with calibrated separation. *Applied Phyics Letters*, 80(2):321–323, January 2002.

[21] A. F. Morpurgo, C. M. Marcus, and D. B. Robinson. Controlled fabrication of metallic electrodes with atomic separation. *Applied Physics Letters*, 74(14):2084–2086, April 1999.

[22] Hongkun Park, Andrew K. Lim, A. Paul Alivisatos, Jiwoong Park, and Paul L. McEwen. Fabrication of metallic electrodes with nanometer separation by electromigration. *Applied Physics Letters*, 75(2):301–303, July 1999.

[23] X. E. He, S. Boussaad, B. Q. Xu, C. Z. Li, and N. J. Tao. Electrochemical fabrication of atomically thin metallic wires and electrodes separated with molecular-scale gaps. *Journal of the Electroanalytical Chemistry*, 522:167–172, 2002.

[24] J. L. Costa-Krämer, N. García, P. García-Mochales, and P. A. Serena. Nanowire formation in macroscopic metallic contacts: quantum mechanical conductance tapping a table top. *Surface Science*, 342:L1144–L1149, 1995.

[25] Henk van Houten and Carlo Beenakker. Quantum point contacts. *Physics Today*, pages 22–27, July 1996.

[26] Liudmila A. Pozhar. Structure and dynamics of nanofluids: Theory and simulations to calculate viscosity. *Physical Review E*, 61(2):1432–1446, 2000.

[27] B. J. Ford. Brown observations confirmed. *Nature*, 359(6393):265–265, 1992.

[28] Brian J. Ford. Brownian movement in clarkia pollen: A reprise of the first observations. *The Microscope*, 40(4):235–241, 1992.

[29] Robert Brown. Additional remarks on active molecules. *Philosophical Magazine*, 6(161), 1829.

[30] Albert Einstein. über die von der molekularkinetischen Theorie der Wärme gefordete Bewegung von in ruhenden Flüssigkeiten suspendierten Teilchen. *Annalen der Physik*, 17:549, 1905.

[31] Albert Einstein. *Investigations on the Theory of the Brownian Movement.* Dover, 1956.

[32] Hilding Faxén. Der Widerstand gegen die Bewegung einer starren Kugel in einer zähen Flüssigkeit, die zwischen zwei parallelen ebenen Wänden eingeschlossen ist. *Archiv För Mathematic, Astronomi och Fysik*, 18(29):1–52, 1924.

[33] Alec T. Clark, Moti Lal, and Gill M. Watson. Dynamics of colloidal particles in the vicinity of an interacting surface. *Faraday Discussions of the Chemical Society*, 83:179–191, 1987.

[34] Luc P. Faucheux and Albert J. Libchaber. Confined brownian motion. *Physical Review E*, 49(6):5158–5163, June 1994.

[35] David G. Levitt. Dynamics of a single-file pore: Non-fickian behavior. *Physical Review A*, 8(6):3050–3054, December 1973.

[36] Binhua Lin, Bianxiao Cui, Ji-Hwan Lee, and Jonathan Yu. Hydrodynamic coupling in diffusion of quasi-one-dimensional Brownian particles. *Europhysics Letters*, 57(5):724–730, March 2002.

[37] Q.-H. Wei, C. Bechinger, and P. Leiderer. Single-file diffusion of colloids in one-dimensional channels. *Science*, 287:625–627, January 2000.

[38] C. L. Hansen, E. Skordalakes, J. M. Berger, and S. R. Quake. A robust and scalable microfluidic metering method that allows protein crystal growth by free interface diffusion. *Proceedings of the National Academy of Sciences of the United States of America*, 99(26):16531–16536, 2002.

[39] Mark A. Unger, Hou-Pu Chou, Todd Thorsen, Axel Scherer, and Stephen R. Quake. Monolithic microfabricated valves and pump by multilayer soft lithography. *Science*, 288:113–116, April 2000.

[40] Phillip Espinasse. Light directs fluid flow. *OE Magazine*, 3(10):7,9, October 2003.

[41] Richard B. M. Schasfoort, Stefan Schlautmann, Jan Hendrikse, and Albert van den Berg. Field-effect flow control for microfabricated fluidic networks. *Science*, 286:942–945, 1999.

[42] C. Lee and A. Lal. Low-voltage high-speed ultrasonic chromatography for microfluidic assays. In *Proceedings of the Solid State Sensor and Actuator Workshop*, pages 206–209, Hilton Head Island, South Carolina, 2002.

[43] M. K. Araz, C. H. Lee, and A. Lal. Ultrasonic separations in microfluidic capillaries. In *Proceedings of the IEEE-UFFC Conference*, Hawaii, 2003. IEEE.

[44] R. B. Hastings and Yung-Yao Shih. Experiments with an electrically operated kundt tube. *American Journal of Physics*, 30:512–516, 1962.

[45] Robert A. Carman. Kundt tube dust striations. *American Journal of Physics*, 23:505–507, 1955.

[46] Deniz Ertas. Lateral separation of macromolecules and polyelectrolytes in microlithographic arrays. *Physical Review Letters*, 80(7):1548–1551, February 1998.

[47] Joel S. Bader, Richard W. Hammond, Steven A. Henck, Michael W. Deem, Gregory A. McDermott, James M. Bustillo, John W. Simpson, Gregory T. Mulhern, and Jonathan M. Rothberg. DNA transport by a micromachined Brownian ratchet device. *Proceedings of the National Academy of the Sciences of the United States of America*, 96(23):13165–13169, November 1999.

[48] Gary W. Slater, Hong L. Guo, and Grant I. Nixon. Bidirectional transport of polyelectrolytes using self-modulating entropic ratchets. *Physical Review Letters*, 78(6):1170–1173, February 1997.

[49] Alexander van Oudenaarden and Steven G. Boxer. Brownian ratchets: Molecular separations in lipid bilayers supported on patterned arrays. *Science*, 285:1046–1048, August 1999.

[50] Thomas T. Perkins, Stephen R. Quake, Douglas Smith, and Steven Chu. Relaxation of a single DNA molecule observed by optical microscopy. *Science*, 264:822–826, May 1994.

[51] Steven Chu. Laser manipulation of atoms and particles. *Science*, 253:861–866, August 1991.

[52] A. Ashkin. Optical trapping and manipulation of neutral particles using lasers. *Proceedings of the National Academy of Sciences of the United States of America*, 94:4853–4860, May 1997.

[53] Mladen Barbic. Magnetic resonance diffraction using the magnetic field from a ferromagnetic sphere. *Journal of Applied Physics*, 91(12):9987, 2002.

[54] L. L. Sohn, O. A. Saleh, G. R. Facer, A. J. Beavis, R. S. Allan, and D. A. Notterman. Capacitance cytometry: Measuring biological cells one-by-one. *Biophysical Journal*, 80(1):144A–144A, 2001.

Chapter 2

Lithography Techniques for Nanometer Sized Fluid Channels and Electrodes

2.1 Introduction

Integrated circuit technology became practical as a result of advances in lithographic techniques and development of thin film processing techniques [1]. These advances in lithography allowed circuit designers to define increasingly smaller sized physical structures of circuit components and connecting wires. Reducing component size not only allowed smaller circuits, but also enabled operating at higher frequencies while consuming less power. This is the foundation of Moore's scaling law [2]. Advances in processing techniques permit building new types of active and passive devices on a single semiconductor substrate. These techniques for building integrated circuits have been borrowed for manufacturing micro-electromechanical systems (MEMS), nano-electromechanical systems (NEMS), and microfluidic systems.

2.2 Sub-micron Scale Lithography

One of the most important technological advances in integrated circuits was the development of a method of defining microscopic circuit elements accurately and repeatably. Initially, integrated circuit components were fabricated by using a screen printing method originally designed for printing photo reproductions [1]. This process involves using a thick paint to block the pores on a fine mesh screen. Printing is performed by forcing a resist ink through the pores that are not blocked by the paint (Figure 2.1). This basic technique is still utilized in the mass production of circuit boards.

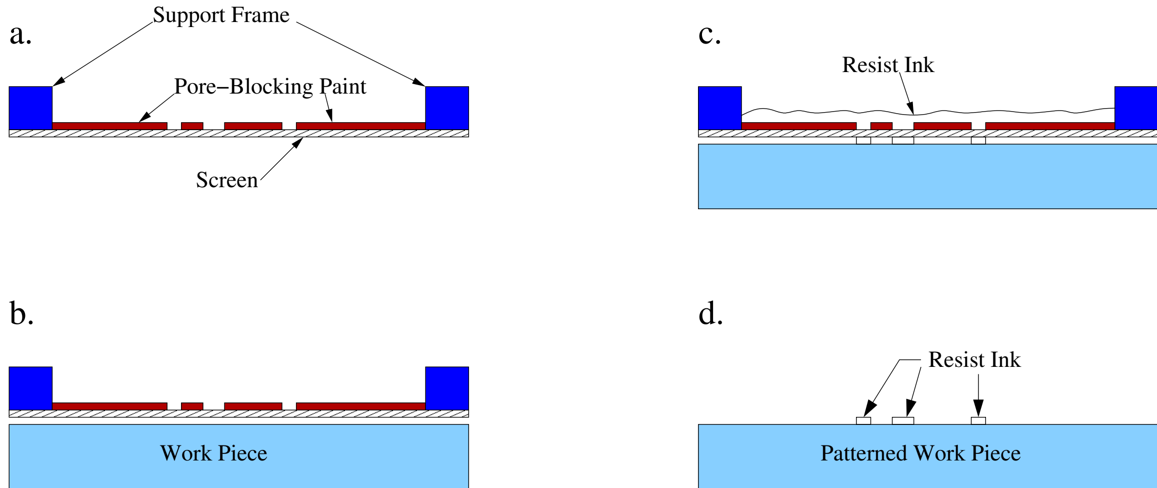

Figure 2.1: Screen printing process: a. The screen is attached to a rigid frame and patterned with pore-blocking paint. b. The screen is held against the work piece. c. Ink is forced through the pores and onto the surface of the work piece. d. The finished result is a pattern in the ink.

The smallest feature size that can be fabricated with this technique is limited by the size of the pores in the screen. Typical pore sizes used for this technique are around 100 μm. This technology is not capable of producing the micron-scale features required by modern microelectronics. However, recent developments in nanoporous materials [3] suggests that the screen printing technique could become useful in the mass production of nanopatterned media such as the magnetic storage surface of computer disk drives [4, 5]. This approach was superseded by development of photosensitive resist material capable of making smaller electronic devices integrated on a single chip [6, 7, 8, 9].

Advances in methods by which patterns are printed on semiconductor wafer surfaces was, and still is, a major driving factor governing the development of integrated circuits. Current technology is capable of producing features significantly smaller than the wavelength of light used for exposure by exploiting a number of basic optical and chemical properties of the photolithography process.

2.3 Photolithography

The first challenge in defining microscopic devices is to precisely control the shape of each part. In traditional machining, this is done by removing material with a cutting tool. In micro-machining, material is removed by chemical or physical dissolution or erosion methods that remove material from exposed surface areas. To machine specific shapes by etching requires patterned masks to protect areas that should not be removed. Such masks are made of photo-sensitive polymers, called photoresists, that are coated on part surfaces. Photolithography is the process of exposing photoresist

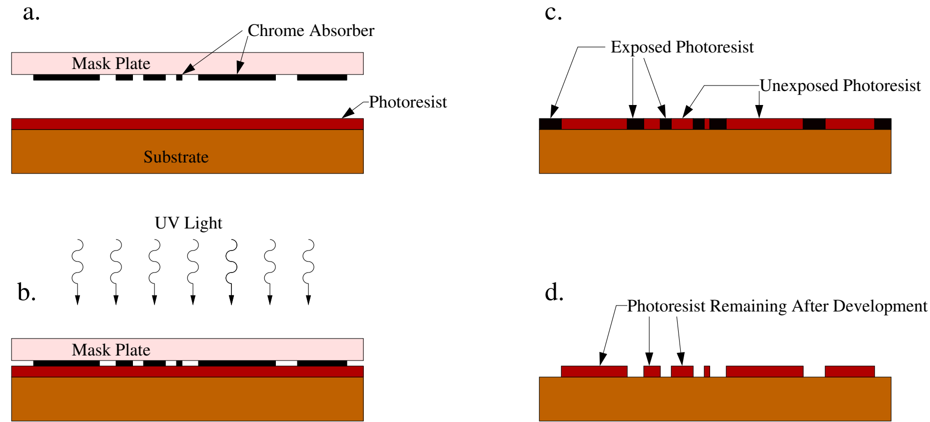

Figure 2.2: Photolithography process steps: a. Align mask with the photoresist coated substrate. b. Bring the mask and substrate together, and expose the photoresist to ultra violet light through the mask. c. Develop the photoresist to remove exposed areas. d. After developing the substrate is ready for subsequent processing steps.

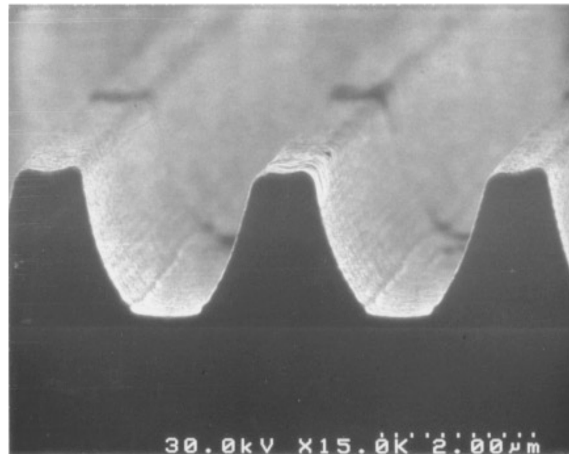

Figure 2.3: Cross-sectional view of photoresist stripes on a silicon wafer.

to light in selective regions and development in a chemical solution to define a pattern.

Photolithography is similar to developing a photographic emulsion. Light which falls on a piece of photographic film induces local changes in the chemistry of the emulsion. In photography the developing process causes the emulsion to change in areas exposed to light. Photoresists used in photolithography differ from photographic emulsions in that a resist developer will remove the exposed material rather than merely change its color. Once a pattern of resist has been defined on the surface, the entire surface can be etched to selectively remove material not protected by the resist, and transfer the resist pattern into the workpiece with high fidelity. The basic photoresist process is shown in Figure 2.2. Figure 2.3 shows a typical cross-section of stripes made in photoresist.

2.4 Shadow Mask Lithography

In some applications, it is necessary to create device features that are smaller than the minimum size obtainable with lithography processes that are commonly used. A number of techniques enable the fabrication of sub-resolution features. The geometries possible with this technique are limited, but, when used appropriately, surprising results are possible at little expense or effort. Moreover, no specialized equipment is needed, and it may even be feasible to introduce these techniques into commercial and manufacturable processes.

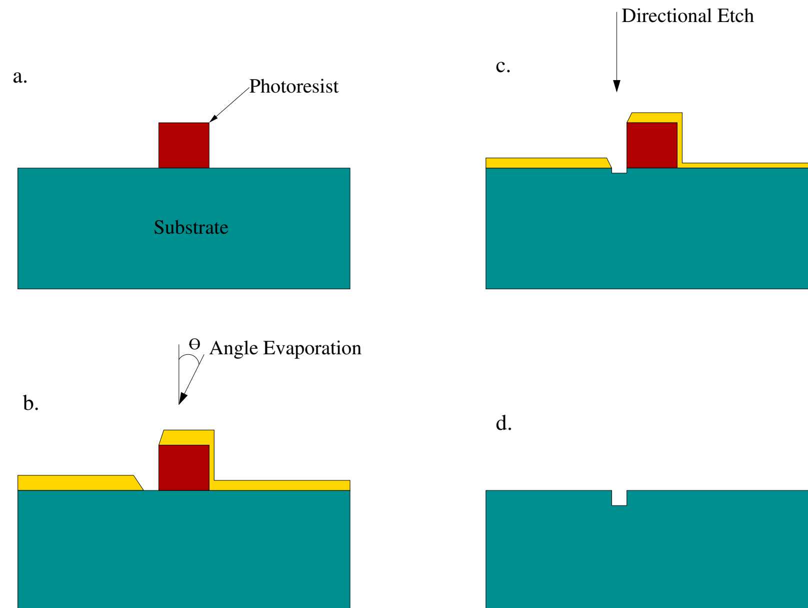

Figure 2.4: Shadow mask process: a. Begin with a photoresist feature. b. Evaporate the metal etch mask at an angle Θ from normal. c. Pattern is transferred into the substrate with a directional etch. d. Final result after removal of the etch mask and photoresist.

The term "shadow mask" refers to the physical shadowing of a flux of atoms as they are deposited onto the surface of the work piece. By placing the substrate at a given angle to the beam of material as it is deposited, the profile of the photoresist creates a small gap adjacent to the photoresist, where the substrate remains exposed [10]. Figure 2.4 shows a typical process which utilizes shadow masking to etch a narrow channel. Figure 2.4 a. and b. illustrate the shadowing effect of the photoresist during deposition of the evaporated material, Figure 2.4 c. illustrates the directional etch step, and 2.4 d. the final result. One important characteristic of shadow masking is that it will create a small shadow on one side of a feature made in photoresist. Figure 2.5 shows a cross section of a sample fabricated using the shadow masking technique. The substrate has been etched, but the photoresist and platinum etch mask have not yet been removed from the surface. Figure 2.6 shows a top view

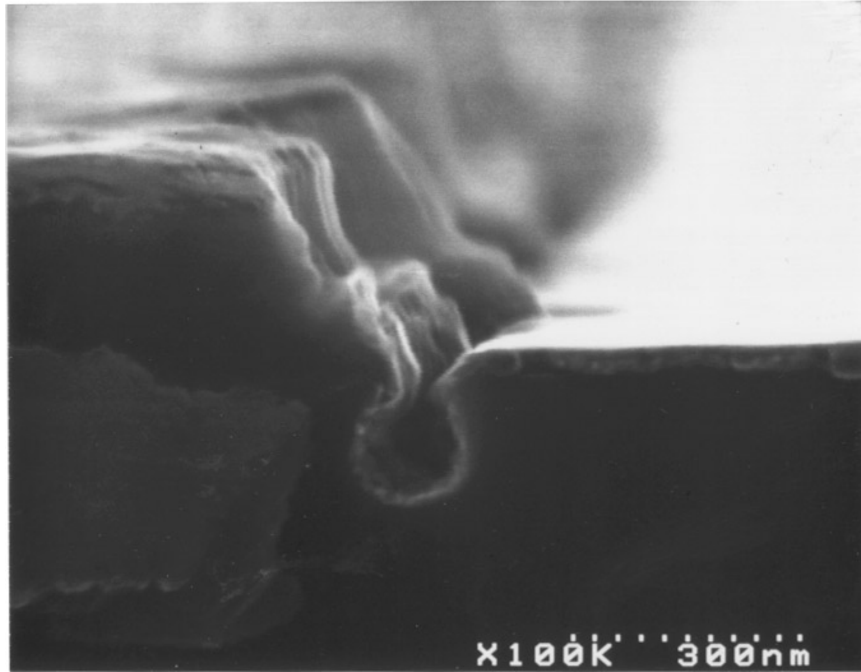

Figure 2.5: Cross-section of a fluid channel made with a shadow mask technique.

of the step depicted in Figure 2.4 c.

Processing steps for shadow mask lithography

1. Prepare and clean substrate[1].

2. Vapor coat with HMDS adhesion promoter.

3. Spin coat photoresist (Shipley SPR3010)

4. Soft bake the photoresist on a hot plate with a surface temperature of 95 °C for 60 seconds.

5. Expose the photoresist through a mask.

6. Post exposure bake on a hot plate set to 105 °C for 60 seconds. This step is specifically for SPR3010, some photoresists do not require a post exposure bake.

7. Develop the photoresist. For SPR3010 the developer used was MF-701 although a number of similar developers work equally well. The developing time was 30 seconds.

8. Rinse with deionized water for 30 seconds.

[1]Substrate cleaning and preparation are discussed in Chapter 3.

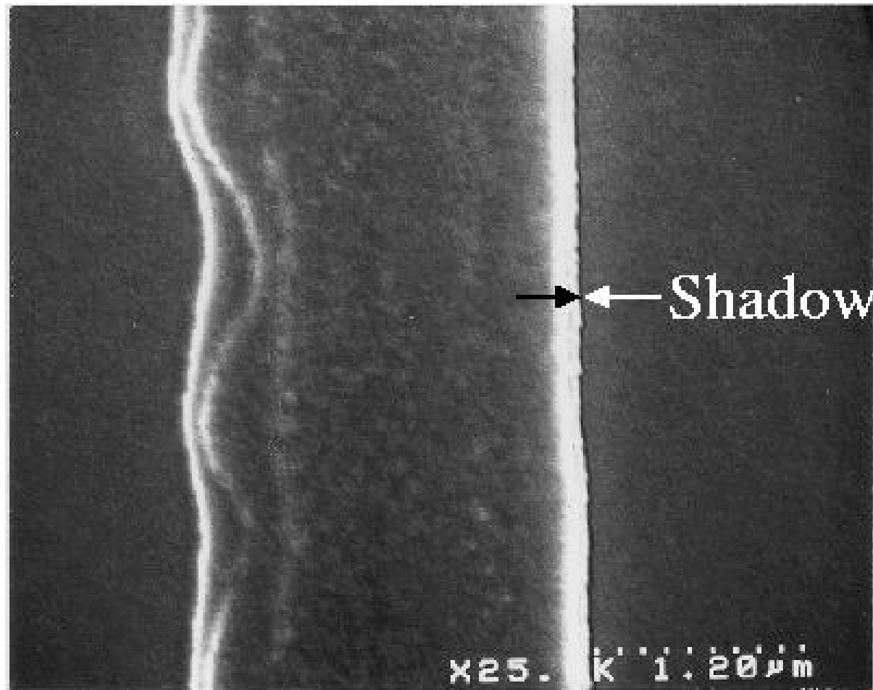

Figure 2.6: Line made using shadow mask technique.

9. Spin dry the wafer by placing it back on the spin coater and spinning it at 5,000 RPM for 20 seconds.

10. Hard-bake the photoresist at 120 °C for 60 seconds.

11. Load the wafer into a metal evaporator with the surface tilted at the desired angle. Orient the wafer to shadow the appropriate side of photoresist features.

12. Evaporate metal to deposit a layer only as thick as is absolutely necessary for future processing steps.

In Figure 2.6 the roughness of the photoresist edge is fairly typical for photolithography, and results from small pieces of photoresist that are either not removed in the developer, or that are redeposited onto the surface as the developer is rinsed away. These small pieces of remaining material can be removed by placing the sample in an oxygen plasma for a short time. This was not done in the case of the sample shown, because the oxygen plasma cleaning would also round off photoresist edges, and would result in a shadow with a less clearly defined edge.

Shadow masking has been found useful for making large numbers of devices with small features. The minimum device spacing is, however, limited by the resolution of the patterning method. This

method was found to be useful only for simple devices, and is not appropriate for building nanometer sized channels and electrodes along with larger connecting structures necessary for testing. The increase in the number of required processing steps, low repeatability, and limitations on design geometries make electron-beam lithography more practical for device prototyping.

Another technique closely related to shadow masking is an undercut etching technique. In this approach, a layer of material just beneath the photoresist is etched away to leave a small gap between the edge of the photoresist and the edge of the underlying layer (Figure 2.7 a, b). The overhanging edge of photoresist is then used to shadow the small area beneath the metal during a subsequent evaporation step (Figure 2.7 c). The evaporation is done with a beam of atoms incident perpendicular to the surface. Removal of photoresist then leaves small channels on either side of where the photoresist once was (Figure 2.7 d).

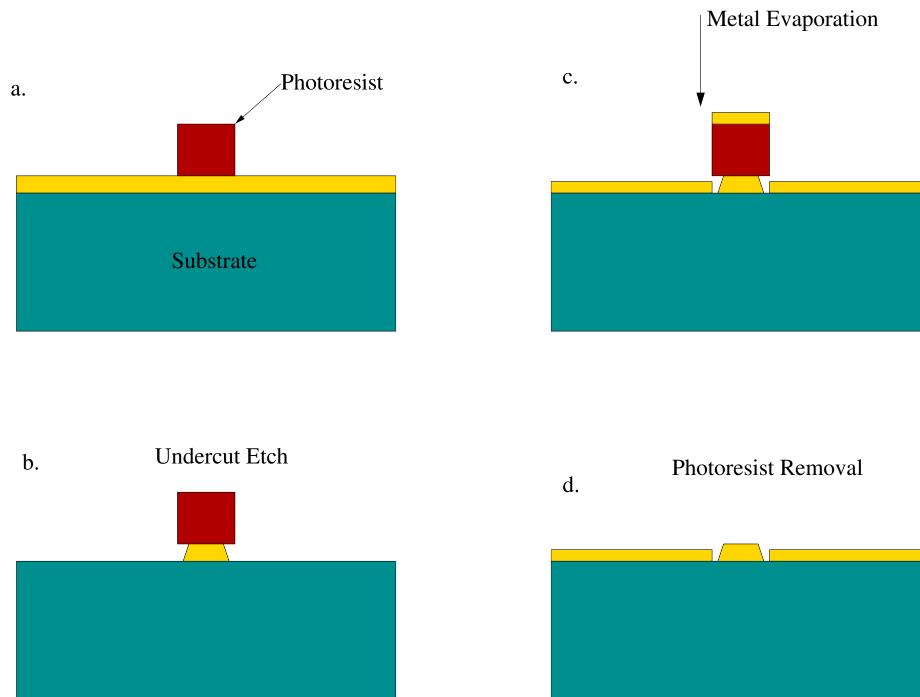

Figure 2.7: Undercut etch technique: a. Begin with a photoresist feature on top of a mask material. b. Etch exposed mask areas with an isotropic etch to remove the mask material just under the photoresist edges. c. Deposit a second etch mask layer. The overhanging edge of the photoresist will create a small gap. d. Pattern is transferred into the substrate with a directional etch.

The layer beneath the photoresist can be any material applied to the surface with a uniform thickness, and can be selectively etched with an etch that does not attack the photoresist or the substrate. Chrome works very well for this application despite its tendency to form small crystalline regions that create a rough surface. An example of this technique is pictured in Figure 2.8. The

chrome etch used to undercut the photoresist consists of a mixture of ceric ammonium and acetic acid manufactured by Transene Co. Inc [11]. The etch rate of this solution is very repeatable, and slow enough that the amount of undercut can be precisely controlled.

Processing steps for undercut etching and evaporation

1. Prepare and clean substrate[2].

2. Evaporate a thin layer of material to be undercut. The rate at which this material will be undercut depends upon its thickness. A thinner layer will take longer to undercut, therefore the amount of undercut can be controlled more precisely. In the case Figure 2.8 this layer consisted of 50 nm of chromium.

3. Spin coat photoresist (Shipley SPR3010)

4. Soft bake the photoresist on a hot plate with a surface temperature of 95 °C for 60 seconds.

5. Expose the photoresist through a mask.

6. Post exposure bake on a hot plate set to 105 °C for 60 seconds. This step is specifically for SPR3010, some photoresists do not require a post exposure bake.

[2]Substrate cleaning and preparation are discussed in Chapter 3.

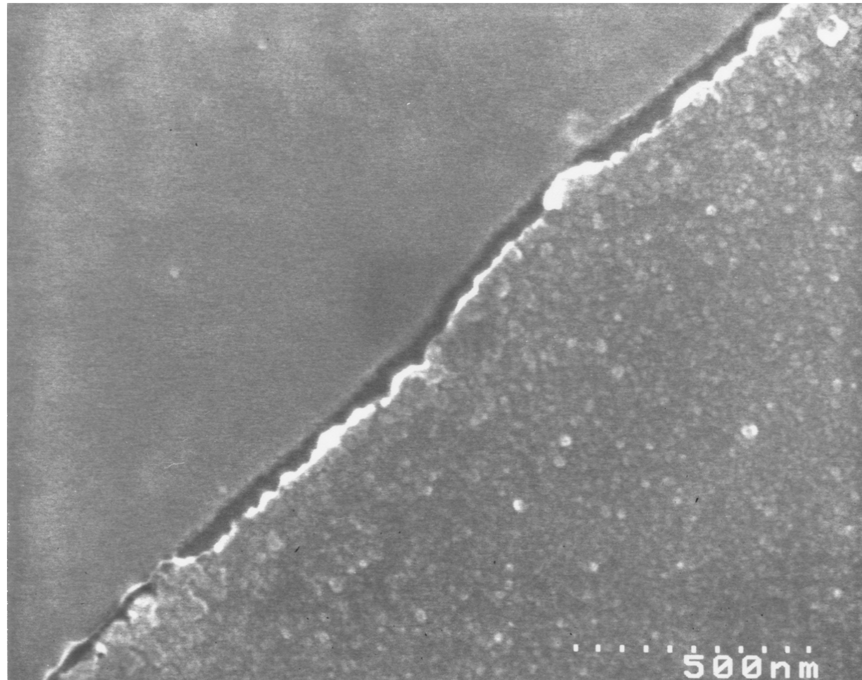

Figure 2.8: Results of the chrome undercutting technique.

7. Develop the photoresist. For SPR3010 the developer used was MF-701 although a number of similar developers work equally well. The developing time was 30 seconds.

8. Rinse with deionized water for 30 seconds.

9. Spin dry the wafer by placing it back on the spin coater and spinning it at 5,000 RPM for 20 seconds.

10. Hard-bake the photoresist at 120 °C for 60 seconds.

11. Etch the underlying chromium layer using chrome etch for 10 seconds.

12. Load the wafer into a metal evaporator with the surface normal to the source flux.

13. Evaporate metal to deposit a layer only as thick as is absolutely necessary for future processing steps.

14. Remove the photoresist using acetone.

In addition to metals, a few polymer materials have been specially designed to create an undercut profile. One that works quite well is the LOR series of chemicals manufactured by Microchem Corporation [12]. This polymer is compatible with most photoresist processes and developers. Because the LOR is etched by many common photoresist developers, a separate etch step to create the undercut profile is not necessary. The undercut profile is created by developing the photoresist for a time slightly longer than what is required for a normal process.

This method is not very dependent on the cross-sectional profile of the features made in the photoresist, which is often difficult to control. Additionally, the gap that is produced is uniform on all edges of a feature instead of only one side as in shadow masking.

2.5 Electron-Beam Lithography

Electron-beam lithography is a technique that uses a focused electron beam to change the properties of a resist layer [13]. Rather than using a mask as in optical lithography, the desired pattern is traced out by the electron-beam. The instrument employed to do this is an electron microscope with a few simple modifications which allow it to be used for electron-beam lithography. The X and Y scan coils of the electron microscope are disconnected from the scan circuitry for normal operation, and are instead controlled by a computer through a digital to analog converter. The desired pattern is

made with a computer drawing program, and converted to a series of X and Y beam movements that trace the pattern on the sample surface with the electron-beam (Figure 2.9) [14, 15, 16].

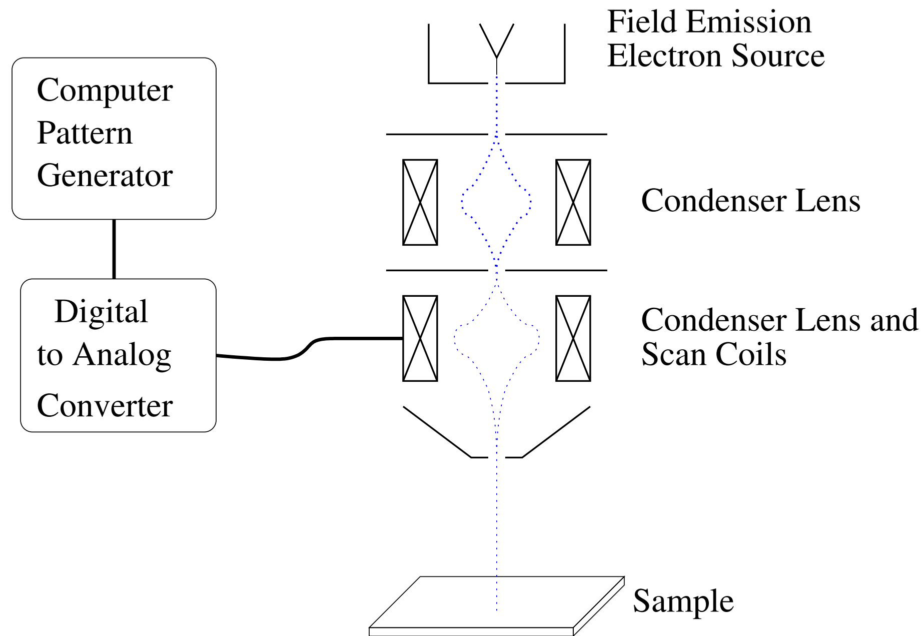

Figure 2.9: Electron-beam lithography system.

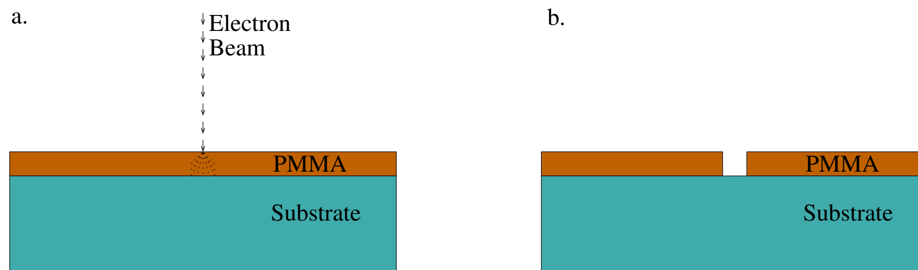

Figure 2.10: a. Electron-beam resist exposure. b. Electron-beam resist development.

The resist material in electron-beam lithography is exposed using electrons rather than photons as in photolithography (Figure 2.10 a.). The most commonly used resist material is PMMA, or polymethyl methacrylate. Some common names for this material are Plexiglas and acrylic. The developer used is an organic solvent such as methyl isobutyl ketone and isopropyl alcohol (Figure 2.10 b.) [17]. Figures 2.11 and 2.12 show examples of patterns made using electron-beam lithography.

Electron-beam lithography processing steps.

These were the processing steps used to create the Caltech logo in Figure 2.11.

1. Evaporate 10 nm of chromium followed by 35 nm of gold onto a silicon wafer.

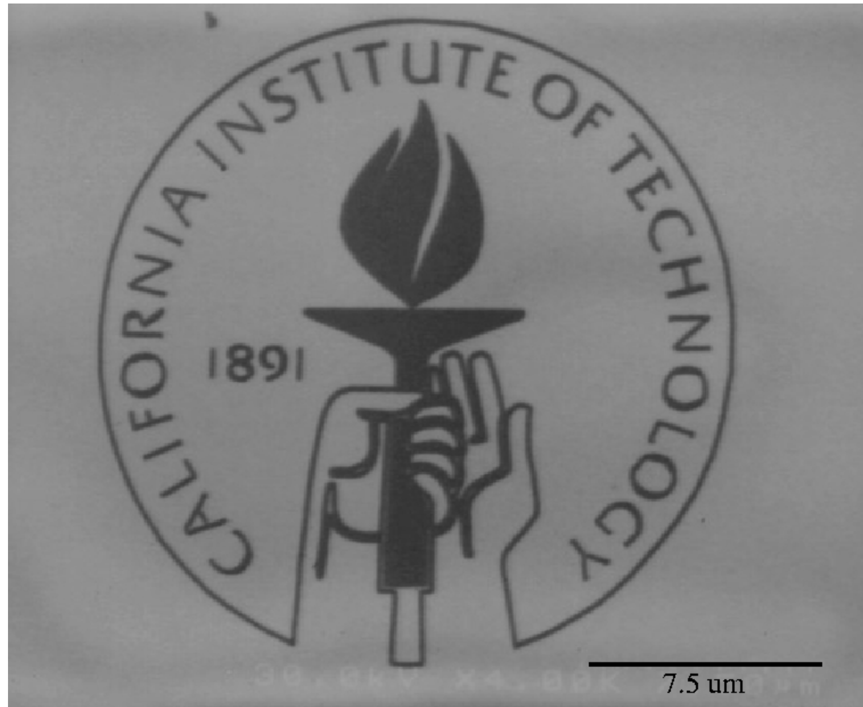

Figure 2.11: Caltech logo machined in a thin gold film on a silicon wafer.

2. Spin-coat PMMA at 10,000 RPM, resulting in a thickness of 90 nm for a solution of 2% 950K molecular weight PMMA in chlorobenzine.

3. Bake the PMMA an a hot plate set to 180 °C for 30 minutes.

4. Place the sample on the SEM sample holder and load into the SEM.

5. Carefully align the SEM electron column, focus the beam and adjust the stigmators to obtain the sharpest possible image.

6. Expose the pattern using a dose of 5 to 10 $\mu C/cm^2$ with the beam voltage set to 30 kV.

7. Develop the pattern with a solution of one part MIBK (methyl isobutyl ketone) and three parts IPA (isopropyl alcohol) for 30 seconds with gentle agitation.

8. Rinse with IPA for 30 seconds.

9. Blow the sample dry using compressed nitrogen.

10. Etch the chrome and gold using the patterned PMMA as the etch mask.

The resolution of electron-beam lithography is limited by the spot size of the electron-beam, and the amount of beam spreading once it enters the electron sensitive resist. The broadening of

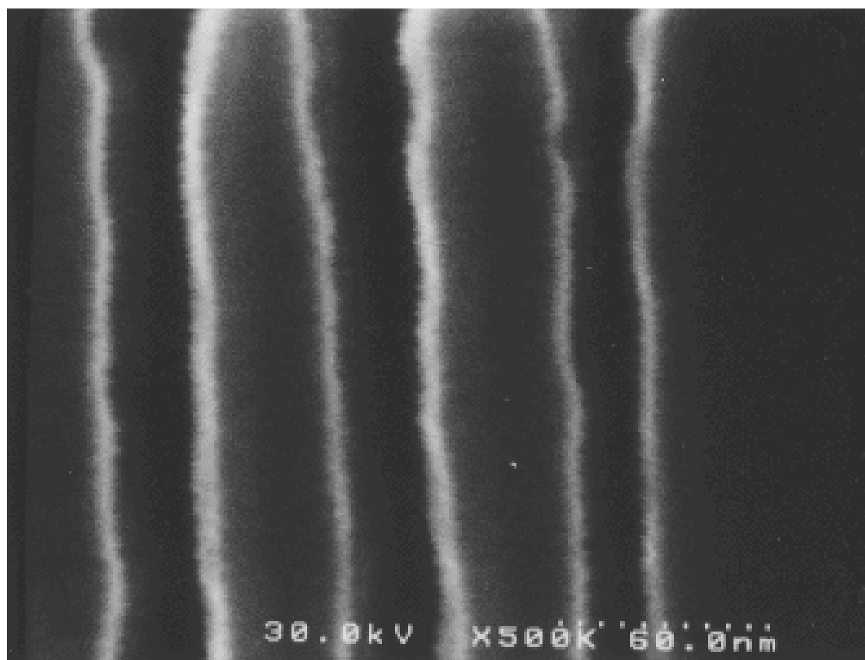

Figure 2.12: Etched lines in silicon patterned by electron-beam lithography and etching.

the electron spot size is in part due to scattering of electrons from resist molecules, and partially to generation of secondary electrons that spread out in every direction. These effects have been studied both experimentally and computationally using Monte Carlo analysis. Results indicate that beam spreading is inversely proportional to the electron source accelerating voltage. Higher accelerating voltage generally results in higher secondary electron yields, and implies that an optimal acceleration voltage exists for a given type of sample, taking into consideration the type of electron sensitive resist used, its thickness, and the secondary electron yield from the substrate [18]. In practice the accelerating voltage is determined by the equipment being used. Most electron microscopes are not capable of accelerating voltages larger than 30 kV. Production type electron-beam lithography systems use accelerating voltages in the range of 50 kV to 100 kV. These high voltages are beneficial for commercial systems because they allow greater process latitude, and can produce high aspect ratio features in thick resist layers [19]. The disadvantage to high acceleration voltage is the increase in pattern error as a result of proximity effect correction; certain areas will be overexposed as a result of electron scattering while exposing adjacent features. Lower acceleration voltages require less proximity effect correction.

2.6 Electron Image Projection System

Electron image projection system (ELIPS) is a technique that may solve the problem of low throughput of electron-beam lithography [20]. Instead of using a sharply focused electron-beam to draw exposure patterns in the resist, the ELIPS system uses a patterned electron emitter to simultaneously expose all of the desired features at the same time. Electrons emitted from the patterned electron emitter are accelerated toward the sample by means of a bias voltage applied between the emitter and sample. A magnetic field parallel to the electric field is used to prevent electrons from spreading and blurring the resulting image. Early attempts at developing this lithography system were not successful, due to an insufficiently uniform magnetic field over the sample surface.

Since this approach was first attempted, advances in superconducting magnets made stronger and more uniform magnetic fields possible. This lithography technique was attempted using a superconducting magnet from a NMR system with a bore diameter of 2.5 inches. This technique was successful in transferring patterns with features of 100nm. Performance at this level was difficult to achieve repeatably. The failure of this system to produce consistent results was most likely due to a combination of many factors. The electrons are emitted from the patterned electron emitter with random initial velocities. The electrons with an initial velocity not perpendicular to the sample substrate result in a blurring of the features on the patterned electron emitter. The amount of blurring is inversely related to the time required for the electron to travel from the emitter to the sample.

2.7 Conclusion

Lithography is the single most important step in building nanometer scale devices. The techniques presented here were developed in the process of this research. The most important aspect to keep in mind when implementing these techniques is what process steps limit the overall resolution, and why. For example in electron beam lithography, focusing the electron beam to the smallest possible circular spot is more important than optimizing exposure doses or development times.

The most valuable processes are those in which the resolution limiting process is one that is fairly easy to control. For example in undercut etching the undercut distance is determined by the etch rate during undercutting. If this process is well characterized, it is possible to obtain an accuracy of less than 50 nm.

The most important part of this work is the development of detailed shadow-masking and un-

dercut etching techniques that allow sub-micron patterning of some geometries obtained through photo-lithography. These approaches are more easily adapted to automated mass production of devices because they do not require the use of electron beam lithography. While this limits this technique to pattens of simple design, it achieves resolution comparable with the best electron beam lithography systems for a small fraction of the cost.

References

[1] Jack S. Kilby. Invention of the integrated circuit. *IEEE Transactions on Electron Devices*, 23(7):648–654, 1976.

[2] Gordon E. Moore. Cramming more components onto integrated circuits. *Electronics*, 38(8), April 1965.

[3] Kornelius Nielsch, Jinsub Choi, Kathrin Schwirn, Ralf B. Wehrspohn, and Ulrich Gösele. Self-ordering regimes of porous alumina: The 10% porosity rule. *Nano Letters*, 0(0):A–D, 2002.

[4] M. Barbic, S. Schultz, J. Wong, and A. Scherer. Recording processes in perpendicular patterned media using longitudinal magnetic recording heads. *IEEE Transactions on Magnetics*, 37(4):1657–1660, 2001.

[5] J. Wong, A. Scherer, M. Barbic, and S. Schultz. Perpendicular patterned media in an $(Al_{0.9}Ga_{0.1})_2O_3$/GaAs substrate for magnetic storage. *Journal of Vacuum Science & Technology B*, 17(6):3190–3196, 1999.

[6] Minoru Tsuda. Some aspects of the photosensitivity of poly(vinyl cinnamate). *Journal of Polymer Science: Part A*, 2:2907–2916, 1964.

[7] Minoru Tsuda. An interpretation of the optical sensitivity of poly(vinyl cinnamate). *Polymer Letters*, 2:1143–1146, 1964.

[8] L. M. Minsk, J. G. Smith, W. P. Van Deusen, and J. F. Wright. Photosensitive polymers. I. cinnamate esters of poly(vinyl alcohol) and cellulose. *Journal of Applied Polymer Science*, 2(6):302–307, 1959.

[9] E. M. Robertson, W. P. Van Deusen, and L. M. Minsk. Photosensitive polymers. ii. sensitization of poly(vinyl cinnamate). *Journal of Applied Polymer Science*, 2(6):308–311, 1959.

[10] Ivor Brodie and Julius J. Muray. *The Physics of Micro/Nano-Fabrication*. Microdevices Physics and Fabrication Technologies. Plenum Press, 1992.

[11] Chrome etchant CE-8002-A. Technical report, Transene Co. Inc., 10 Electronics Ave. Danveros MA 01923.

[12] LOR^{TM} lift-off resists. Technical report, Microchem Corp., 1254 Chestnut Street, Newton, MA 02464, 2002.

[13] *SPIE Handbook of Microlithography, Micromachining and Microfabrication*. SPIE.

[14] Haroon Ahmed. Single electron electronics: Challenge for nanofabrication. *Journal of the Vacuum Society of America B*, 15(6):2101–2108, November/December 1997.

[15] Shazia Yasin, D. G. Hasako, and H. Ahmed. Fabrication of <5nm width lines in poly(methylmethacrylate) resist using a water:isopropyl alcohol developer and ultrasonically-assisted development. *Applied Physics Letters*, 78(18):2760–2762, April 2001.

[16] Wei Chen and Haroon Ahmed. Fabrication of 5-7 nm wide etched lines in silicon using 100 kev electron-beam lithography and polymethylmethacrylate resist. *Applied Physics Letters*, 62(13):1499–1501, March 1993.

[17] Ilesanmi Adesida, Thomas E. Everhart, and R. Shimizu. High resolution electron-beam lithography on thin films. *Journal of Vacuum Science and Technology*, 16(6):1743–1748, November/December 1979.

[18] Ilesanmi Adesida and Thomas E. Everhart. Substrate thickness considerations in electron beam lithography. *Journal of Applied Physics*, 51(11):5994–6005, November 1980.

[19] Mark A. McCord. Electron beam lithography for 0.13 μm manufacturing. *Journal of Vacuum Science and Technology B*, 15(6):2125–2129, November/December 1997.

[20] IEEE. *Fabrication of Integrated Circuits Using the Electron Image Projection System (ELIPS)*, October 1969.

Chapter 3

Fabrication Procedure for Nanometer-Sized Fluid Channels and Electrodes

3.1 Introduction

This chapter reviews processing techniques that are most relevant to nanofabrication. Processing operations can be separated into individual steps that either add or remove material from the surface. Combining these basic functions with lithography techniques described in the previous chapter provide the basic set of tools necessary to build micro and nanometer-scale fluidic devices.

3.2 Thin Film Deposition

Thin film deposition is used to make the metal wires and insulating layers on integrated circuits. Many types of optical coatings including reflective metal films, dielectric anti-reflective coatings, and multilayer thin film mirrors are made using thin film deposition techniques. A wide variety of techniques exist for depositing thin films onto surfaces. Only the techniques that are most relevant to building nanometer-size devices will be considered here.

3.2.1 Thermal Evaporation

Thermal evaporation is by far the most widely used method of depositing thin films. A material is simply heated in a vacuum chamber until it begins to vaporize. The vapor then condenses on the surfaces inside the chamber. Any object exposed to the condensing vapor will be coated with a thin film of the material being evaporated. The usual method of heating the source material is to place

it in a wire basket or a metal "boat" that is resistively heated by passing a large electrical current through it, as illustrated in Figure 3.1 a [1, 2].

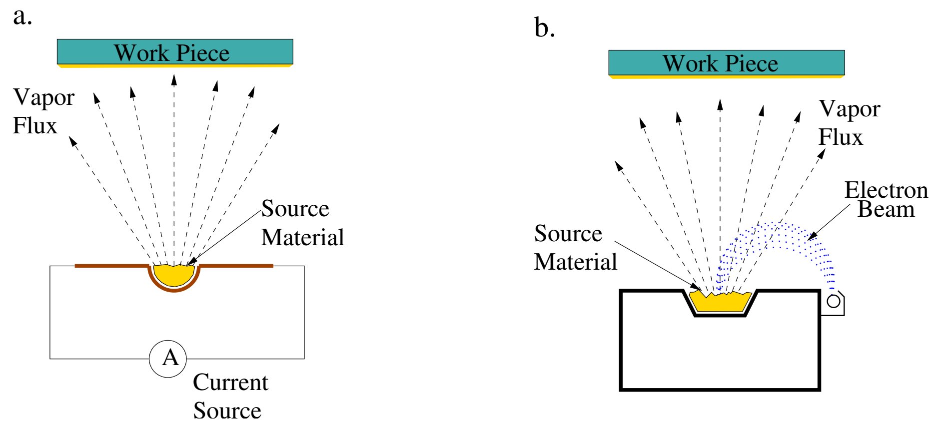

Figure 3.1: a. Thermal evaporation, b. Electron-beam evaporation.

3.2.2 Electron-Beam Evaporation

Electron-beam evaporation is a technique that uses an intense electron beam to heat the source materials and cause thermal evaporation(Figure 3.1 b.). It can be applied to more materials than thermal evaporation. Materials with high melting temperatures such as platinum and materials of low thermal conductivity such as silicon dioxide can be processed by electron beam evaporation. The method is also capable of evaporating materials at a rate much higher than thermal evaporation, thus it is useful for situations where a thick layer needs to be deposited. The intense vapor flux produced by electron beam evaporation allows rapid deposition [1, 2].

In a technique such as shadow mask lithography (Section 2.4) electron beam evaporation provides a great advantage. The intense material flux rate allows placing the sample far from the source while maintaining a reasonable evaporation rate. Placing the sample as far away from the source as possible also produces a clearly defined edge to the shadow, similar to a shadow produced by the intense flux of a collimated light beam. Evaporation from a shorter sample-source separation produces a fuzzy edge, similar to a shadow resulting from a diffuse light source [1].

The electron beam evaporator used in this work was designed to have a maximum spacing between the sample and the source of 25 cm. The shadow masks previously shown in Figures 2.6 and 2.5 were both made using this system.

3.2.3 Sputtering

Sputtering is a method that uses a plasma to remove material from one surface to be deposited on a second surface. Atoms or molecules are removed from one surface by bombarding it with ions from a plasma magnetically confined to this surface. The flux of material from the source surface condenses onto nearby surfaces creating a uniform coating (Figure 3.2) [3].

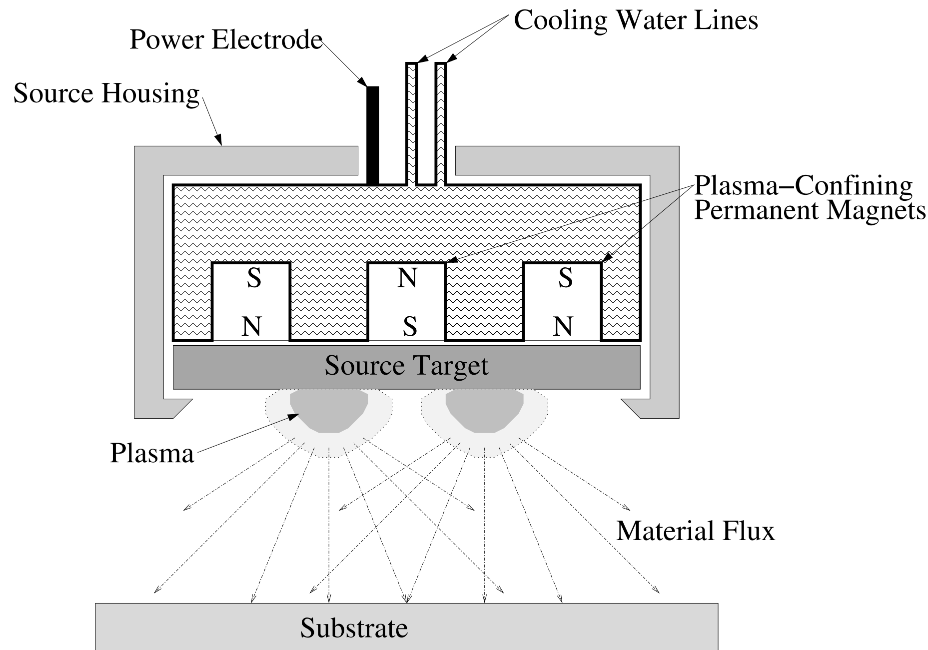

Figure 3.2: Sputtering.

Sputtering differs from evaporation in that the atomic velocities are more randomly oriented as they approach the sample surface. This explains why shadow effects seen in evaporation are normally not seen with sputtering. This difference arises from three factors; the size of the sputtering source, the sample-source spacing, and the vacuum level during deposition. The source size and sample-source spacing determine the amount of collimation of the flux. In electron beam lithography, flux collimation was achieved by using a small source placed far from the sample in a ultra high vauccum system. Sputtering uses a large source more closely spaced to the sample to achieve an opposite effect. The pressure in the vacuum chamber is greater for sputtering than for evaporation. Greater chamber pressure decreases the mean free particle path and increases their trajectory variation [2, 1].

Sputtering can deposit thin layers from a wide range of source materials because the source need not be heated to its melting point. The most common methods of sputtering are magnetron sputtering and ion beam sputtering. In magnetron sputtering, a plasma is generated by either a

large voltage, or a high power radio frequency (13.5 MHz) signal. The plasma is confined to the surface of the source material by a local magnetic field. In ion beam sputtering, an ion beam is accelerated at the source target. In both of these techniques the source material is removed from the source target through the collisions of energetic ions with the surface [3].

3.3 Etching

Etching is the basic method of removing material from a surface. Usually, it is necessary to remove material only in certain areas. The areas that are not to be etched are protected by an etch mask. In many cases, however, the etch mask material will be removed at the same time. One measure of the quality of an etch process is the selectivity ratio; the relative etch rate of the mask layer to the layer being etched.

3.3.1 Reactive Ion Etching

A plasma is started in a rare atmosphere of a reactive gas in a vacuum chamber (Figure 3.3 a). The ionization process also dissociates the reactive gas into smaller, highly reactive, ionized molecules. The variation in ion density creates a potential drop from the main body of the plasma to the lower plate on which the material to be etched is placed (Figure 3.3 b). The effect of this potential drop is to accelerate ions toward the surface. The high velocity ions impart kinetic energy to the surface that increases the reaction rate, resulting in a faster etch rate on horizontal surfaces than vertical features, making it possible to obtain sharp features with vertical walls (Figure 3.4) [2, 4, 5, 6, 7]. Figure 3.4 was made in a Materials Research Corporation reactive ion etching system under the following conditions:

- C_2F_6 flow rate: 25 sccm (standard cubic centimeters per minute)
- argon flow rate: 5 sccm
- chamber pressure: 35 mTorr
- electrode spacing: 3 inches (7.6 cm)
- power level: 60 Watts
- lower electrode voltage: 250 V
- time: 5 minutes

3.3.2 Ion-Beam Etching

Ion beam etching or milling is a very useful technique for creating nanometer-sized structures. It is appropriate for etching features less than 20 nm in width. Ion beam etching erodes organic resist materials very slowly, and results in vertical etch walls with little or no undercutting. The etch mechanism does not depend on chemical reactivity, making this technique suitable for patterning materials that would otherwise be problematic to etch.

Ion sources were originally developed as a method of spacecraft propulsion, and are commonly used for positioning satellites [8]. Using electrostatics to accelerate a beam of ions away from the spacecraft in turn results in a small motive force. Even though the acceleration provided by such a drive is very small when compared to rocket propulsion, it is possible to accelerate the spacecraft to high speeds over long distances in the vacuum of space. Because this type of propulsion does not require bulky chemical propellants, ion propulsion is optimum for long missions where it would not be practical to exclusively use chemical propellants.

Early in the development of ion propulsion systems it was noticed that the wall of the vacuum test chamber at which the ion beam was directed began to develop pits on the surface. Application of the ion beam technique to etching was quite obvious [9].

Ion beam production consists of a filament heated to a temperature resulting in thermionic emission of electrons. The electrons are accelerated toward the anode. A magnetic field influences their path so that instead of directly moving to the anode, they move in a circular orbit inside an

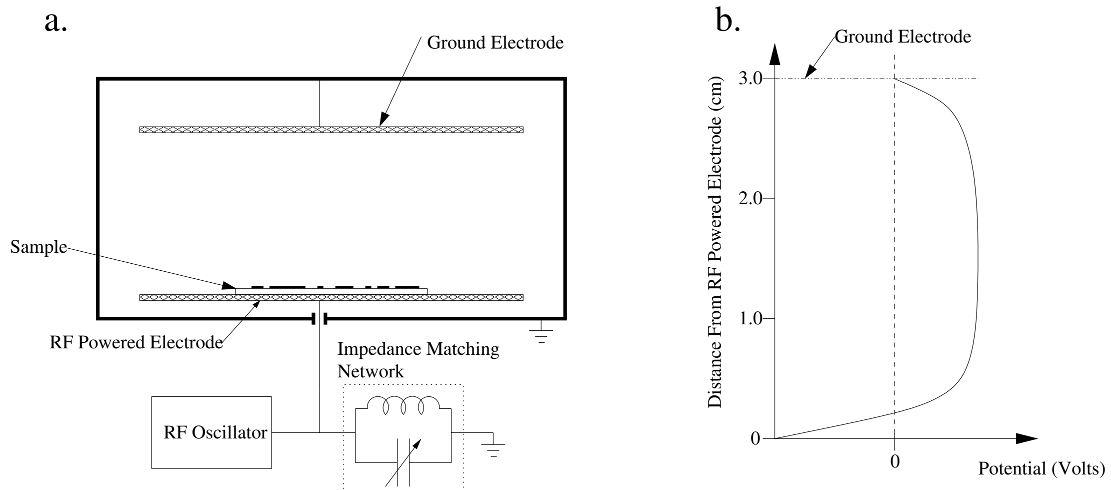

Figure 3.3: a. RIE etching chamber. b. Plasma potential profile between the capacitive plates of an RIE system.

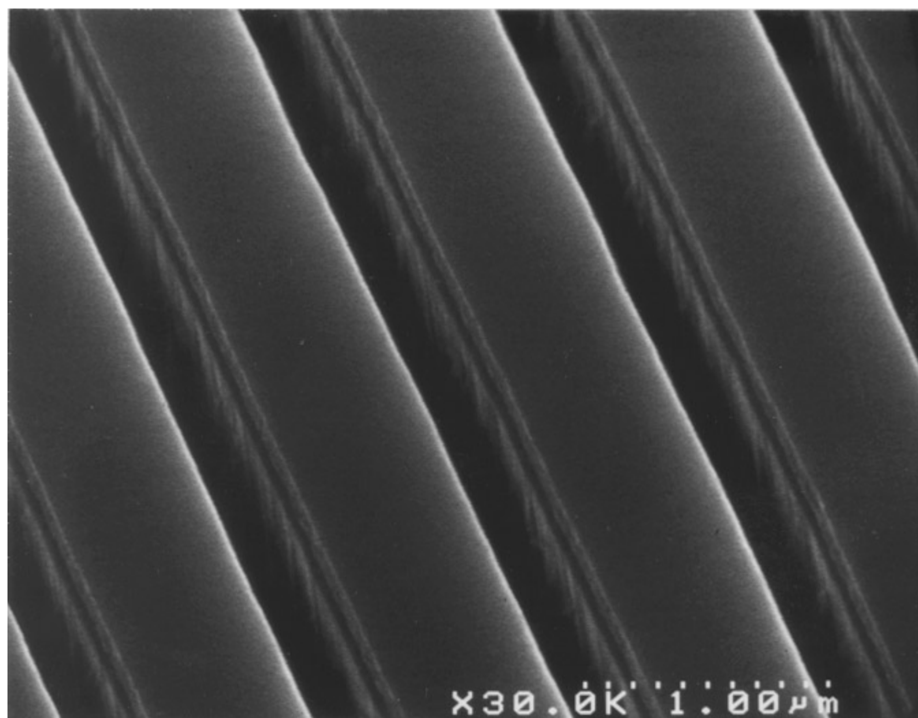

Figure 3.4: Channels etched in a fused silica microscope slide with a C_2F_6 reactive ion etching process.

anode cup. When a gas molecule or atom collides with an electron, it is ionized and loses one or more of its outer shell electrons. The ions then drift under the influence of the beam voltage toward the accelerator grids. The voltage differential across the accelerator grids accelerates these ions and collimates them into a beam directed towards the sample. In order to prevent excessive build up of positive charge on the sample surface, an electron flux is added to the ion beam to result in a net neutral charge. Electrons are added by a neutralizer filament through thermionic emission [10, 11, 12, 13]. Figure 3.5 shows the basic components of an ion beam source.

If a neutralizing filament is not used, charge will build up on the surface of the sample, and in a cloud of charged particles just above the surface. The presence of these charges will tend to decelerate and deflect incoming ions, thus reducing the etch rate. The exact charge distribution that results is very dependent on the sample material and its physical geometry. A consequence of the cloud is non-reproducible etch rates. Even a conductive sample that is connected to ground will tend to collect a charge cloud just above its surface. A second problem that can occur should the voltage differential be large enough is an electrical discharge between the cloud of charge and the sample surface. This creates very localized damage to areas of the substrate. The discharges are often so intense that they will vaporize the metal layers just underneath the resist. For an example

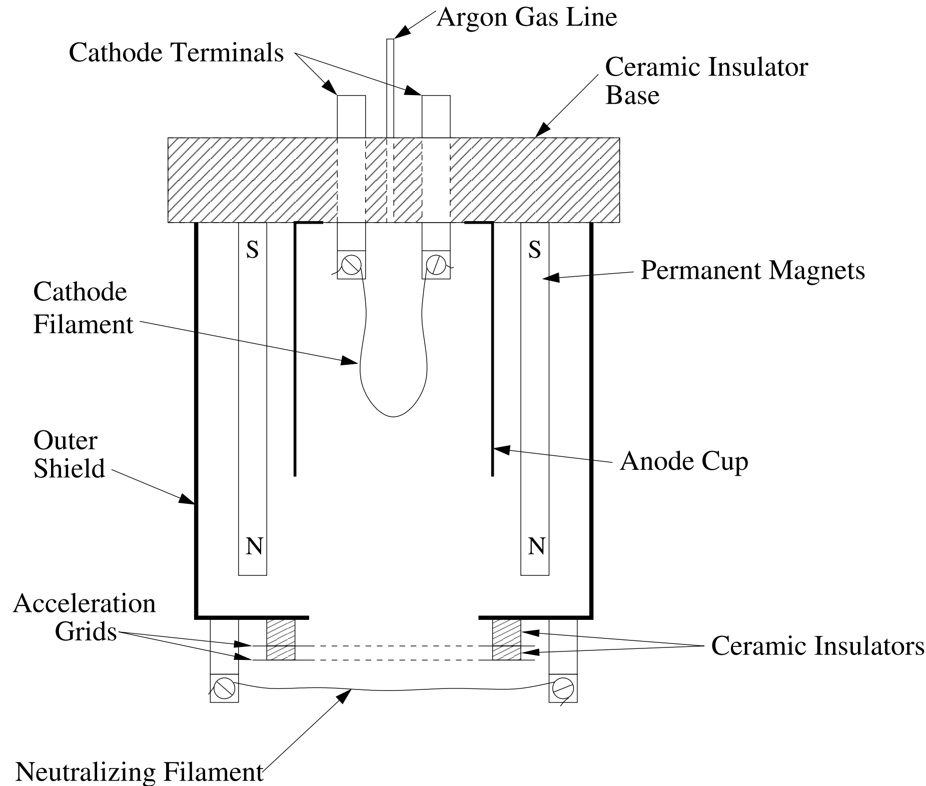

Figure 3.5: Schematic representation of an ion beam source.

of the effects of neutralizing discharges see the scanning electron micrograph of Figure 4.2.

The etching mechanism of ion beam etching is a process by which the kinetic energy of the ions is transferred to atoms on the surface. As the energy of the surface molecules increases, they undergo two important transitions. The first occurs when they have gained enough energy to break the bonds that are holding them to a specific surface location, but not enough energy to allow them to become free from the surface. The second transition occurs when the surface atom or molecules have sufficient energy to break free from the surface. With ion beam etching, the incoming ions have enough energy so that a single ion can remove many surface atoms. There is typically no specific chemical interaction between the ions and the material being etched as there is in reactive ion etching.

Once the molecules diffuse away from the surface either they are removed by the vacuum pump, or condense on nearby objects. The diffusion of the etch products away from the surface is not instantaneous, therefore a local density maximum exists in the vicinity of the surface. In addition, as the incident ions rebound after colliding with the surface, there is also a higher concentration of the ions from the original beam near the surface. Some of the ions from the incident beam will

collide with particles in the region near the surface and will be deflected away. This effect can be reduced by tilting the sample so that the beam is not perpendicular to the sample surface. The velocity component of the ion beam that is parallel to the surface will result in a net motion that will prevent the formation of a local density of particles near the surface by sweeping them off to the side. This can be seen in experiments where the maximum etch rate occurs at somewhere between 45° and 55° from normal. Figure 2.11 is an example of a pattern transferred into a gold layer using ion beam etching. Figure 2.11 was made using a custom built vacuum chamber equipped with a Commonwealth Scientific 2.5 cm diameter ion source operated under the following conditions:

- argon flow rate: 18 sccm
- chamber pressure: $2 * 10^{-4}$ Torr
- beam voltage: 500 v
- acceleration voltage: 100 v
- discharge voltage: 35 v
- beam current: 20.0 mA
- cathode current: 6.6 A
- neutralizer current: 6.46 A
- neutralizer emission current: 21.2 mA
- etch time: 60 seconds

3.3.3 Chemically Assisted Ion-Beam Etching

The etch selectivity of an ion beam etch process can be improved by adding a reactive gas to the ion beam. This modified version of the ion beam etch is termed chemically assisted ion beam etching (CAIBE). Typically, the gas forms volatile reaction products that can be removed at faster rates and consequently increase the sputter yield.

A nozzle above the sample is used to deliver a reactive gas into the ion beam, as illustrated in Figure 3.6. The reactive gas is entrained in the ion beam and directed at the substrate. The position of the nozzle relative to the substrate is an important parameter. Larger spacing will reduce the etch rate but increase uniformity. Smaller nozzle-sample spacing increases the etch rate, but in a

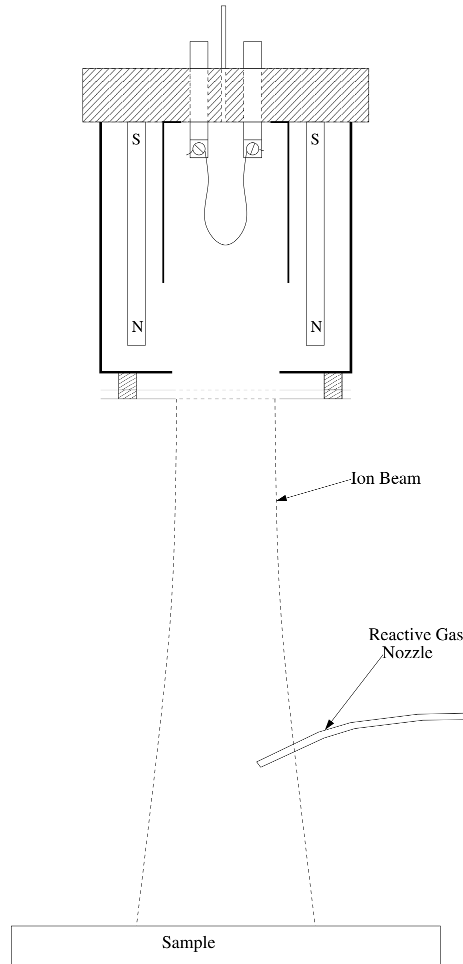

Figure 3.6: Schematic of the position of the reactive gas nozzles in the ion beam path.

smaller area, and may partially block the beam causing a shadow region with almost no etching. In large-scale commercial processes, reactive gas is delivered using a large number of nozzles just outside of the beam path [1]. Figure 3.7 shows a micrograph of 40 to 50 nm channels etched in silicon with a xenon difluoride (XeF_2) reactive gas added to an argon ion beam. Figure 3.8 is similarly made structure. Figures 3.7 and 3.8 were made using a custom built vacuum chamber equipped with a Commonwealth Scientific 2.5 cm diameter ion source, and a nozzle to inject XeF_2 gas into the ion stream. The operating conditions used for the structure in Figure 3.7 are:

- XeF_2 flow rate: 30 sccm
- argon flow rate: 64 sccm
- chamber pressure: $2 * 10^{-}4$ Torr

- beam voltage: 500 v
- acceleration voltage: 100 v
- discharge voltage: 35 v
- beam current: 10.0 mA
- cathode current: 7.6 A
- neutralizer current: 7.0 A
- neutralizer emission current: 12.0 mA
- etch time: 60 seconds

Figure 3.8 was created using very similar conditions.

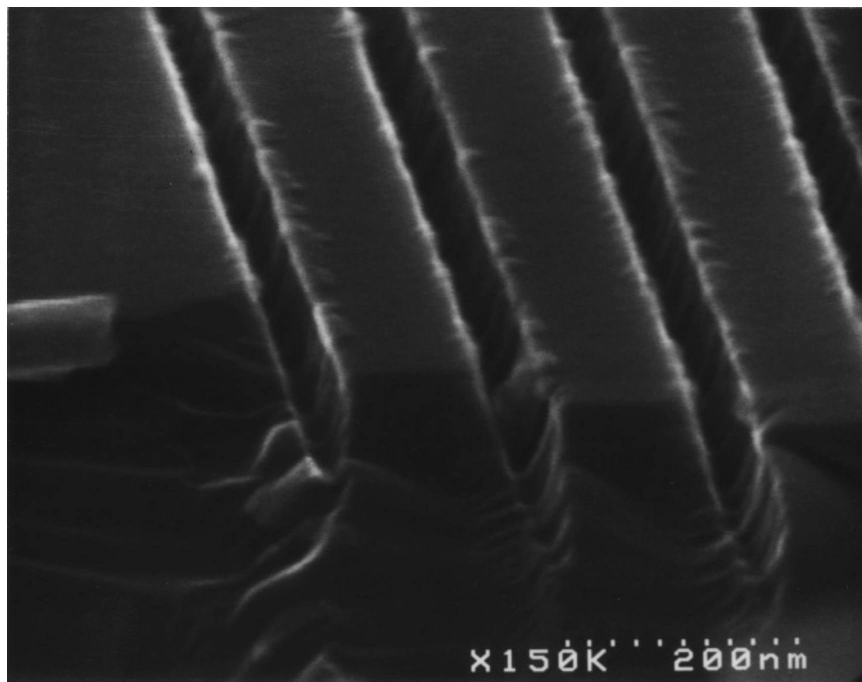

Figure 3.7: Oblique view of channels etched into silicon using an XeF_2 assisted ion beam etch.

3.4 Surface Cleaning

Surface cleaning is necessary to produce a high-quality etched specimen. Surface contamination, such as particles and chemical contaminants, can interfere with subsequent processing steps and

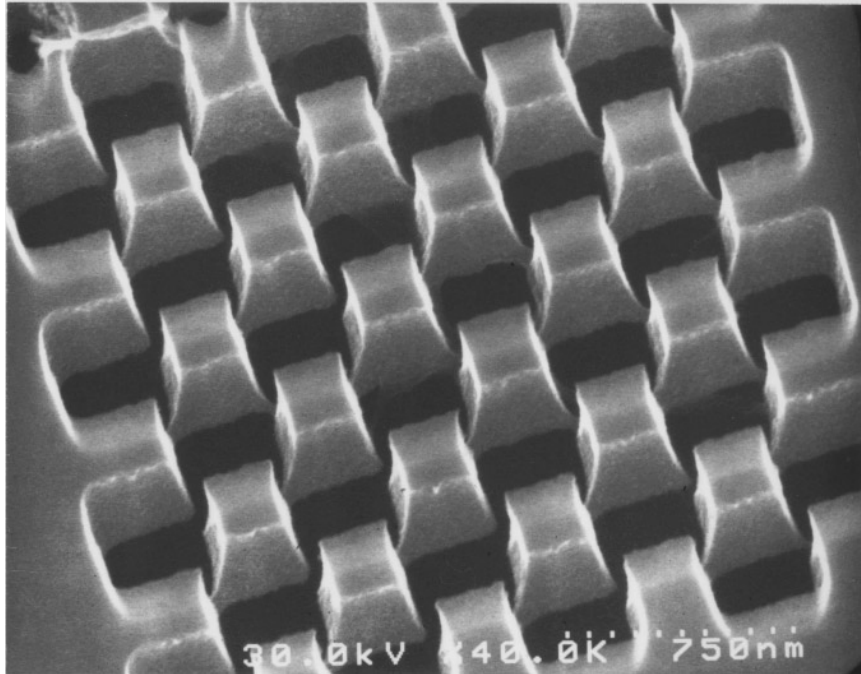

Figure 3.8: Oblique view of a checkerboard test pattern etched in the top layer of an SOI wafer.

adversely impact the final product quality. The success of each processing step depends in part on how diligently the surface is prepared and cleaned. Cleaning the surface of a particular sample requires knowledge of the subsequent processing steps. For example, if the first step is to deposit a layer of metal that will make the surface conductive, and act as an etch mask, then surface contaminants that will prevent the metal mask from adhering to the surface must be removed. Likely contaminants are grease or oil. In addition, particles must be removed to prevent blemishes in the etched pattern and interference with subsequent surface coating processes.

The simplest method of removing particles from the surface is to rinse the sample in deionized filtered water. This is an obvious step which at first glance does not require any further explanation. The process of rinsing a surface in water is so commonplace that it is often taken for granted, and if not done with extra caution, surface contamination left from the water washing can render all other cleaning steps ineffective. This caution is not intended to discourage using water; rather the message is to use water with extra precautions as described in the following paragraphs. Water is often considered one of the most universal solvents [14]. It's ionic nature makes it an excellent solvent for many common ionic compounds [15, 16].

The deionized water rinse works well only for large particles, and is generally not sufficient for our purposes. Of particular concern are particles less than a few microns in size. Particles in this

size range can be quite firmly stuck to the surface as a result of Van der Waals forces. Their large surface-to-volume ratio, small mass, and low hydrodynamic drag make them very difficult to remove with a simple water rinse. These particles can often be removed by placing the sample in a deionized water bath which is agitated ultrasonically. The ultrasonic bath uses piezo transducers to create high energy (100 to 250 W/cm^2) sonic waves with frequencies ranging from 20 kHz to 50 kHz. These intense sonic waves result in cavitation: formation and collapse of bubbles in the liquid bath. This cavitation creates shock waves with enough energy to dislodge particles from the surface.

The surface must be prepared to ensure that the metal mask has good adhesion. A mono-layer of oil will cause poor adhesion of the metal to the surface. Degreasing is a processing step that removes organic residue such as polymers, oils, and greases from surfaces. This is done with a three stage solvent bath, beginning with trichloroethylene, then acetone, and finally isopropyl alcohol or ethyl alcohol. The critical part of these steps is to transfer the sample from one bath to the next without allowing the trichloroethylene and the acetone to dry on the surface. Otherwise, a contaminant film which is often very difficult to remove will be left behind.

3.4.1 Radio Corproation of America (RCA) Cleaning Process

The RCA etch was developed by Werner Kern and Puotinen at RCA to remove film contamination from the surface of silicon wafers [2, 17]. This process was not designed to remove particle contamination from the surface, although when combined with ultrasonic or mega sonic agitation, particles can often be effectively removed as well [17]. The four steps outlined below describe the RCA cleaning process. The ratios given here are volume ratios of the reagents as purchased from the supplier, not absolute volume ratios of each chemical constituent. This is the common convention used in the literature for these types of recipes, and will be maintained here. The assumed concentrations of each reagent are listed in the footnotes.

1. *Preliminary Cleaning* – Remove any organics from the surface using an O_2 plasma, an ozone dry stripper, or a wet chemical etch such as 6 H_2SO_4[1]:1 H_2O_2[2]. This step should be followed by a rinse in deionized and filtered water with a resistivity of 18 MΩ-cm.

2. *RCA SC-1 (Standard Clean 1)* – This step is designed to remove any residual organic contaminants and some metals. This mixture contains 5 H_2O:1 NH_4OH[3]:1 H_2O_2. The mixture is

[1] H_2SO_4: Sulfuric acid 30% in water.

[2] H_2O_2: Hydrogen peroxide should be 30% in water, with no stabilizing additives. Stabilizing additives such as sodium phosphate, sodium stannate, or amino derivatives will recontaminate the surface to be cleaned [17].

[3] Ammonium Hydroxide concentration: 28.0–30.0%.

then heated to 75 to 80°C. The time duration of this step should be 10 to 15 minutes.

3. *Stripping of the Hydrous Oxide Film* – The sample is etched in a dilute solution (1%) of hydrofluoric acid for one minute.

4. *RCA SC-2 (Standard Clean 2)* – This step removes remaining atomic and ionic contaminants. The mixture contains H_2O:HCl[4]:H_2O_2 in the volume ratios 6:1:1 and is heated to 75 to 80°C. This step is followed by another 18 MΩ-cm water rinse.

3.5 Conclusion

The techniques described in this chapter form the basic set of tools for creating nano-scale devices. In this work variations on these processing methods are used to build all of the structures and devices.

[4]Hydrochloric Acid Concentration: 37%.

References

[1] Ivor Brodie and Julius J. Muray. *The Physics of Micro/Nano-Fabrication*. Microdevices Physics and Fabrication Technologies. Plenum Press, 1992.

[2] S. Wolf and R. N. Tauber. *Silicon Processing for the VLSI Era Volume 1 – Process Technology*. Lattice Press, 1986.

[3] H. H. Anderson, H. L. Bay, R. Behrisch, M. T. Robinson, H. E. Roosendaal, and P. Sigmund. *Sputtering By Particle Bombardment I Physical Sputtering of Single-Element Solids*. Springer-Verlag, Berlin Heidelberg New York, 1981.

[4] Evangelos Gogolides, Philippe Vauvert, George Kokkoris, Guy Turban, and Andreas G. Boudouvis. Etching of SiO_2 in fluorocarbon plasmas: A detailed surface model accounting for etching and deposition. *Journal of Applied Physics*, 88(10):5570–5584, November 2000.

[5] K. Sasaki, H. Furukawa, K. Kadota, and C. Suzuki. Surface production of CF, CF_2 and C_2 radicals in high-density CF_4/H_2 plasmas. *Journal of Applied Physics*, 88(10):5585–5591, November 2000.

[6] Y. J. Sung, H. S. Kim, Y. H. Lee, Y. J. Chae, S. H. ond Park, and G. Y. Yeom. High rate etching of sapphire wafer using $cl_2/bcl_3/ar$ inductively coupled plasmas. *Materials Science and Engineering B*, 82:50–52, 2001.

[7] Jae-Whan Kim, Yong-Chun Kim, and Won-Jong Lee. Reactive ion etching mechanism of plasma enhanced chemically vapor deposited aluminum oxide film in CF_4/O_2 plasma. *Journal of Applied Physics*, 78(3):2045–2049, August 1995.

[8] Marc D. Rayman, Philip Varghese, David H. Lehman, and Leslie L. Livesay. Results from the deep space 1 technology validation mission. *Acta Astronautica*, 47:475, 2000.

[9] Harold R. Kaufman. *Technology of Electron-Bombardment Ion Thrusters*, volume 36 of *Advances in Electronics and Electron Physics*. Academic Press, 111 Fifth Avenue, New York, New York 10003, 1974.

[10] H. R. Kaufman, J. J. Cuomo, and J. M. E. Harper. Critical review: Technology and applications of broad-beam ion sources used in sputtering. part i. ion source technology. *Journal of Vacuum Science and Technology*, 21(3):725–736, September/October 1982.

[11] H. R. Kaufman, J. M. E. Harper, and J. J. Cuomo. Developments in broad-beam, ion-source technology and applications. *Journal of Vacuum Science and Technology*, 21(3):764–767, September/October 1982.

[12] J. M. E. Harper, J. J. Cuomo, and H. R. Kaufman. Critical review: Technology and applications of broad-beam ion sources used in sputtering. part ii applications. *Journal of Vacuum Science and Technology*, 21(3):737–756, September/October 1982.

[13] J. L. Speidell, J. M. E. Harper, J. J. Cuomo, A. W. Kleinsasser, H. R. Kaufman, and A. H. Tuttle. The fabrication and use of silicon and gallium arsenide ion source extraction grids. *Journal of Vacuum Science and Technology*, 21(3):824–827, September/October 1982.

[14] R. E. Dickerson and Geis I. *Chemistry, Matter, and the Universe*. W.A. Benjamin, Inc., 1976.

[15] Linus Pauling. *General Chemistry*. Dover Publications Inc., 1988.

[16] R. Chang. *Chemistry*. McGraw Hill, Inc., fourth edition, 1991.

[17] W. Kern. The evolution of silicon wafer cleaning technology. *Journal of the Electrochemical Society*, 137(6):1887–1892, June 1990.

Chapter 4

Nanometer Fluid Channels

4.1 Introduction

In this research nanometer fluid channels are machined in a number of different materials. The motivation for investigating various material systems is to demonstrate a set of fabrication methods applicable to many situations. In addition to the general methods, some specialized techniques are also required, such as etching methods that are chemically reactive with the material in use.

Glass Fluid Channels:

Glass is in many ways an ideal material for micro and nanofluidics. It is optically clear, enabling devices to be analyzed using standard microscopy techniques including fluorescence microscopy. Many different varieties of glass are available with specific properties; for example some glass has a thermal expansion coefficient matched to silicon. Glass is readily available in highly polished plates or wafers that are compatible with many commercial semiconductor processing techniques. Finally, the methods of etching glass are established and well characterized.

For most of this research, a highly pure type of glass called fused silica is used. This grade of glass is commonly referred to as quartz. Normally the term quartz is reserved for crystalline material, but is often used incorrectly to describe vitreous material. Therefore care must be taken when obtaining material from various manufacturers. The fused silica used in this research was obtained either from VWR Scientific, or Esco Inc. The material obtained from these two sources could not be distinguished based on any properties relevant for building sub-micron channels (e.g. etch rate, surface roughness, fluorescence of impurities, etc...), therefore the source of material is not mentioned further in this text.

Silicon Fluid Channels:

Silicon is a material for which the techniques of micro and nano-fabrication have been thoroughly

studied and developed. Silicon is the most commonly used semiconductor for integrated circuits. The techniques of etching, ion implantation, thin film deposition, and lithographic patterning have been characterized and documented for silicon. Machining devices in silicon has the great advantage that many techniques and processes can be used. Here, the use of silicon as a material for building nanometer channels is considered.

Electron-beam lithographic patterning of silicon does not require a separate conductive layer underneath the electron resist to make the surface conductive. The low secondary electron yield of silicon-on-insulator (SOI) wafers make it possible to achieve high resolution electron-beam lithography without the use of proximity effect correction[1].

Polymer Fluid Channels:

Over the past decade, polymers have been one of the fastest changing areas of materials research. Polymers engineered with a wide variety of characteristics are being used in an increasing number of applications. Developing a reliable technique for building micro and nanofluidic devices with polymers will enable integration of many new features in fluid analysis systems.

From a fabrication point of view, the physical parameters of polymers that are important for etching and forming physical structures do not vary as much as physical parameters of different inorganic substrates. If a method of making fluid channels is well developed in a few different polymer systems, these techniques will require little variation in adapting them to a new polymer material. In this research, a few example polymers were used to demonstrate the feasibility of making sub-micron fluid channels from organic polymer systems.

4.2 Lithography

4.2.1 Electron-Beam Lithography

Because fused silica and most polymer materials are insulators, directly patterning the surface with electron-beam lithography is prevented by charge that accumulates on the sample. These charges deflect the primary electron-beam causing distortion in the final patterns. This can be avoided by coating the sample surface with a conductive material that will provide a path to ground for the excess charge that accumulates on the surface as it is irradiated with an electron-beam. The conductive layer chosen for this purpose is generally a thermally evaporated metal layer. The metal used for this purpose depends on the processing steps that follow. The pattern of the resist must be transferred through the metal layer in order to etch the substrate material.

For fused silica, this conductive layer is provided by coating the surface with a layer of gold 10 to 50 nanometers thick on top of a “sticking layer” of chromium 1 to 10 nanometers thick. The chromium is required to prevent the gold from flaking off the surface during processing. The adhesion of gold to glass is very low, however the adhesive forces between glass and chromium and between chromium and gold are sufficient to prevent the gold layer from peeling off.

Once a conductive layer is deposited, an electron beam resist, PMMA (polymethyl methacrylate) is coated on the surface. A cotton swab soaked in acetone is used to remove resist, exposing the gold layer of an area that will not be used. Care must be taken to use only as much acetone as necessary, since the development characteristics of the surrounding resist will be altered if partially dissolved in acetone. The exposed gold provides an electrical path to ground through the same metal clip that secures the sample during electron-beam exposure.

An alternative approach is to deposit a thin layer of gold on top of the electron-beam resist. If this gold layer is thin enough (less than 10 nm) it will be nearly transparent to the electron-beam. However, secondary electrons emitted from this gold layer will produce a slightly higher exposure dose, and a larger effective beam diameter than would be obtained without it. In addition, the tendency of thin gold films to aggregate into small particles will reduce the resolution if this technique is used. However, none of these effects will be noticeable unless the electron-beam is truly focused to a spot-size smaller than 50 nanometers.

In some cases it is not desirable to remove a small area of resist to provide a conductive path to ground. In this case a conductive path can still be created by depositing the gold layer by sputter deposition. Sputter coating uses a low pressure atmosphere of argon to create a plasma in which the ions are accelerated toward a target composed of the material that is to be deposited. The impact of the ions with this target removes atoms, or small particles of the material from the surface. Once the particles and atoms are released from the surface, they diffuse around the chamber until they condense onto a solid surface. Because this process is not carried out in a high vacuum, the mean free path of the particles and atoms is much shorter than the distance between the target and the sample. As a result, the particles collide many times with other particles in the gas before reaching a surface. When they finally do arrive at the surface, they have a fairly randomly oriented velocity. Because of this, sputter coating tends to coat vertical and slightly overhanging surfaces as well as flat horizontal surfaces. As a result, the edges of the sample will also be coated with a conductive layer of gold. In order to ensure that there is a highly conductive path to ground, the substrate is sputter coated with metal on both sides.

4.3 Etching Nanometer Fluid Channels

4.3.1 Transferring the Resist Pattern to the Metal Mask Layer

Ion beam etching is ideally suited for transferring the pattern of the resist to the metal etch mask layer because it is capable of transferring features as small as 20 nanometers to underlying metal layers. Additionally the etch rate of most organic resist materials is low compared to metals. The high selectivity of the etch rate of metals over resist materials puts less stringent requirements on the etching process conditions such as ion energy and etch duration. In practice the etching time can be longer than the minimum amount of time necessary to etch through the metal layer, without over etching and alteration of the fine pattern features. This process latitude makes ion beam etching a very valuable general purpose technique for sub-micron machining. Figure 4.1 is an example of a 50 nm wide line that has been removed from the metal etch mask by ion beam etching.

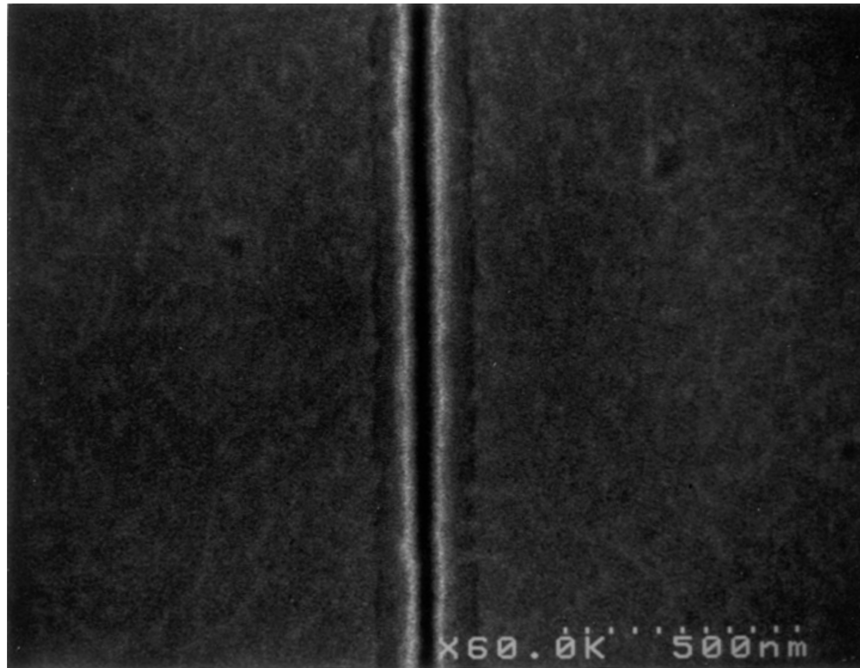

Figure 4.1: Line defined in PMMA that has been transferred into the metal etch mask by ion beam etching.

One aspect of ion beam etching that is not desirable is neutralizing discharges which cause surface damage unless the ion beam is neutralized by the addition of electrons to the beam. Neutralizing discharges are small electrical arcs that are triggered by a charge imbalance between the substrate and the region of space just above the sample. Grounding the metal surface with the sample clip does not help, as the exposed metal will be quickly etched, breaking the conductive path to ground.

Figure 4.2: Neutralizing arc damage on a fused silica wafer.

These discharges tend to have the highest density in areas of the sample where the resist is not present. This makes patterned areas of the resist most susceptible to this type of damage. The effect is local obliteration of any resist features and removal of entire regions of metal layers. Figure 4.2 shows an example of a neutralizing arc damage of the metal and resist layer of a fused silica substrate.

4.3.2 Etching Techniques for Fused Silica Fluid Channels

Structures larger than one micron are most easily etched with hydrofluoric acid. Hydrofluoric acid (HF) is the most common method of etching fused silica[2], and is used extensively when building fluid channels wider than one micron. When using HF to etch fused silica microchannels the channel profile develops rounded edges. The resulting channel dimensions are greater than mask dimensions by approximately twice the etch depth of the channel (see Figure 4.3 a). Etching with HF is most suitable for making channels that are shallow and have a width of more than about ten times the channel depth.

Creating sub-micron features in fused silica is done by reactive ion etching. Reactive ion etching has a tendency to quickly erode most common electron-beam resists and photoresists. Avoiding or minimizing unwanted mask layer erosion is done by transferring the resist pattern into an etch

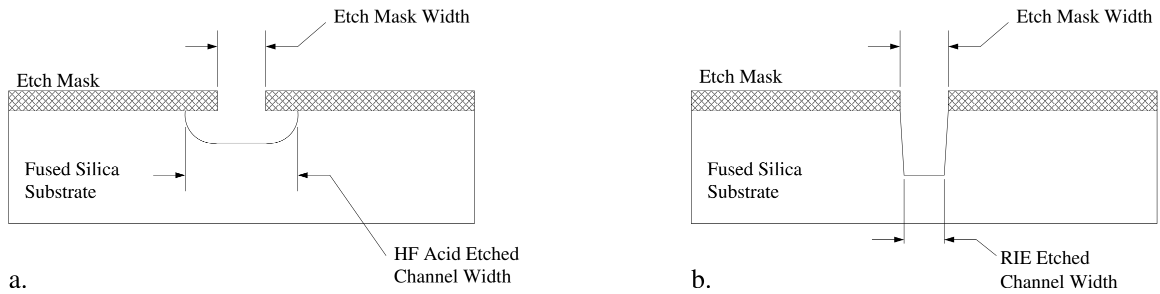

Figure 4.3: a. Etch profile of fused silica that would result from etching with hydrofluoric acid. b. Etch profile of fused silica resulting from RIE.

mask layer that has a lower etch rate than the fused silica. The metal layer under the resist used to increase surface conductive during electron-beam lithography can serve a second function as an etch mask for reactive ion etching. The resist pattern is transferred into the metal layer by ion beam etching prior to fused silica reactive ion etching.

Reactive ion etching (RIE) is used to etch the fused silica in situations where it is desired to make narrow channels[3, 4, 2]. Reactive ion etching generally does not result in a channel width greater than the etch mask width (Figure 4.3 b). Figure 4.4 is a scanning electron micrograph of channels etched using C_2F_6 in a parallel capacitor plate RIE system.

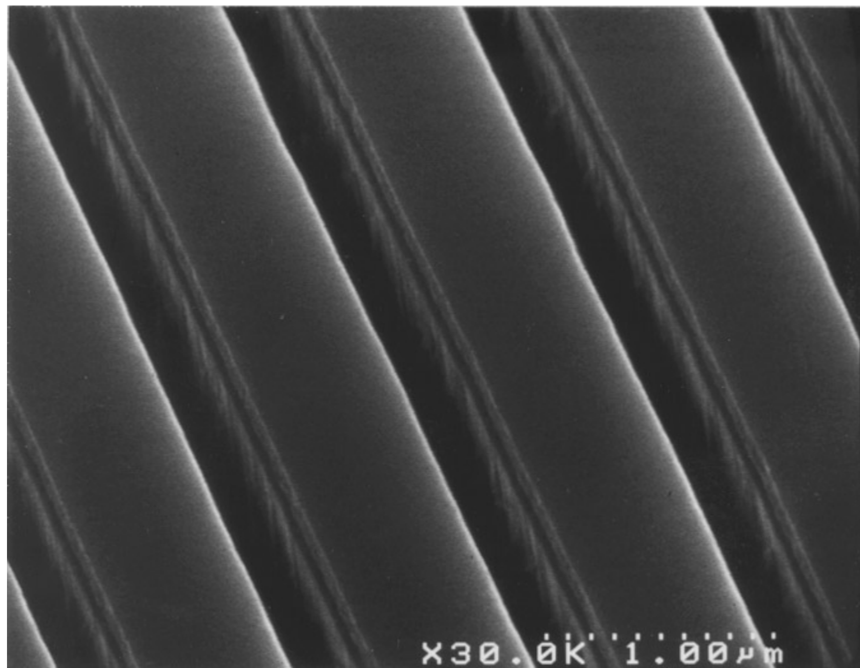

Figure 4.4: Channels in fused silica by a C_2F_6 reactive ion etching process.

4.3.3 Etching Techniques for Silicon Fluid Channels

Etching techniques such as XeF_2 chemically assisted ion beam etching (CAIBE) allows electron-beam lithography resists such as PMMA to be used directly as an etch mask. The relative etch rate of silicon to PMMA using this technique is greater that 5 to 1. Figure 4.5 is an example of a high resolution pattern machined in the top silicon layer of an SOI wafer. Figure 4.6 is an example of a fluidic channel etched in silicon using the same process.

Figure 4.5: Oblique view of the Caltech logo machined in the top layer of an SOI wafer using the same PMMA layer as the electron beam resist and the etch mask during XeF_2 CAIBE processing.

4.3.4 Etching Techniques for Polymer Channels

Polymer materials are easily etched in an oxygen plasma. For this research the etching was performed in an RIE system with a capacitively coupled plasma.

Acrylic Channels

One material that is used in a wide variety of applications is Lucite, or Plexiglas. Not only is this a very common material, but it is a polymer already widely used in nanofabrication. The traditional electron-beam resist PMMA is one specific type of this acrylic polymer. Figure 4.7 is an SEM image of channels made in PMMA by direct electron beam exposure followed by solvent development to remove the exposed regions.

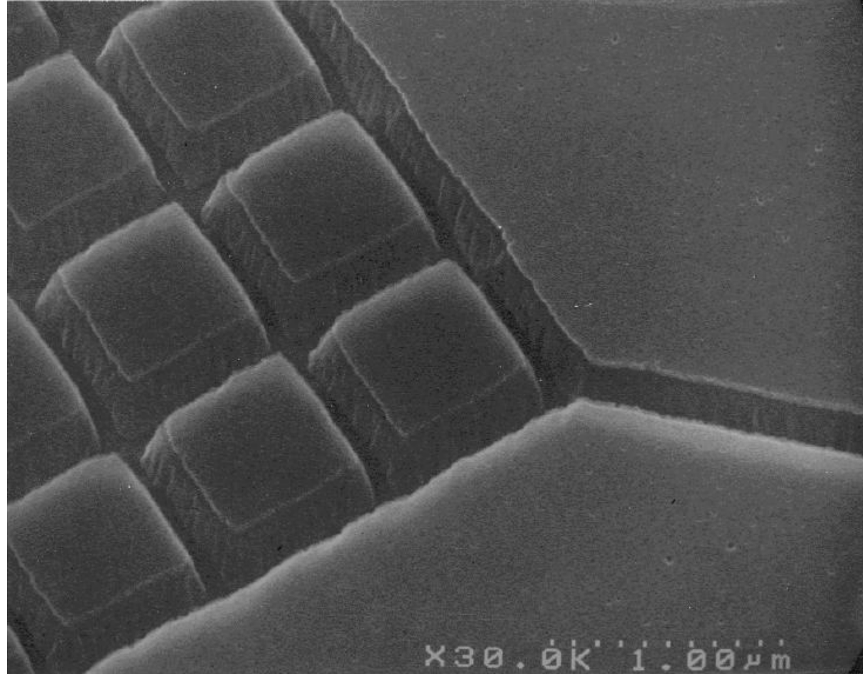

Figure 4.6: Entrance to a silicon fluid channel. The grid pattern on the left side of the image is a filter structure to prevent large particles from blocking the channel on the right.

Mylar® **Channels**

Mylar® is stretched as it is drawn into a thin film. This stretching process is carried out as the film is cooled down to room temperature, creating internal stress in the film. At room temperature the polymer chains cannot easily move past each other, so the internal stress does not result in deformation of the film. Once the film is reheated, the mobility of the polymer chains is increased, and a shrinkage of the film occurs. If film heating is not uniform, the film will crumple and fold over onto itself. This creates difficulties in machining structures in Mylar. It is essential to always keep the temperature of the film below the temperature at which deformation occurs.

Transferring the resist pattern to the metal etch mask with ion beam etching caused thermal damage in Mylar® films with 500 eV ion beam energy and a current density of approximately 4 mA/cm^2. One way to avoid Mylar® film damage is to etch the metal layer using argon gas in an RIE system. While the energy of the argon ions was roughly the same as in ion beam etching, the current density was sufficiently low to prevent over-heating the Mylar®. An alternative method is to construct a shield of aluminum foil to protect the surface except in the small region containing the patterns.

Mylar® film etching was done in an RIE etching system using oxygen etch gas. Adding a small

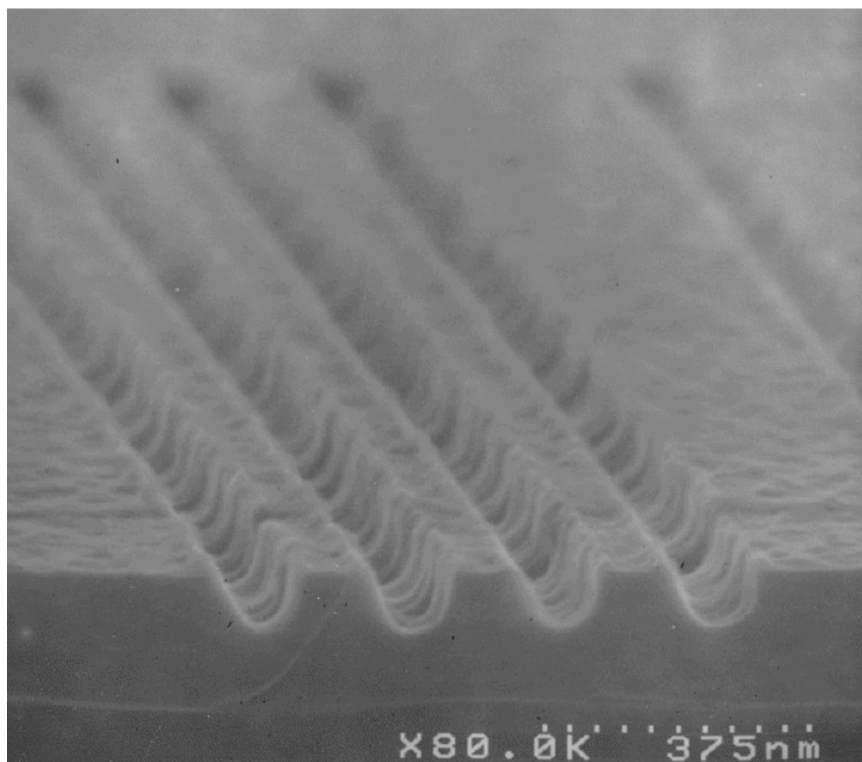

Figure 4.7: Channel defined in a polymethyl methacrylate layer by direct write electron-beam lithography.

quantity of argon to this plasma decreased etched surfaces roughness. Surface roughness in this type of etch is generally caused by redeposition of particles on freshly etched surfaces. The addition of argon to the plasma is believed to prevent redeposition as the energetic argon ions dislodge any redeposited particles. The flow rate of argon into the etching chamber was 10% of the flow rate for oxygen. Figure 4.8 shows the etch profile of a Mylar® sample resulting from a 10 minute Ar/O_2 reactive ion etch process. Figure 4.9 was etched in a Materials Research Corporation reactive ion etching system under the following conditions:

- O_2 flow rate: 70 sccm (standard cubic centimeters per minute)
- argon flow rate: 14 sccm
- chamber pressure: 35 mTorr
- electrode spacing: 3 inches (7.6 cm)
- power level: 80 Watts
- lower electrode voltage: 465 V

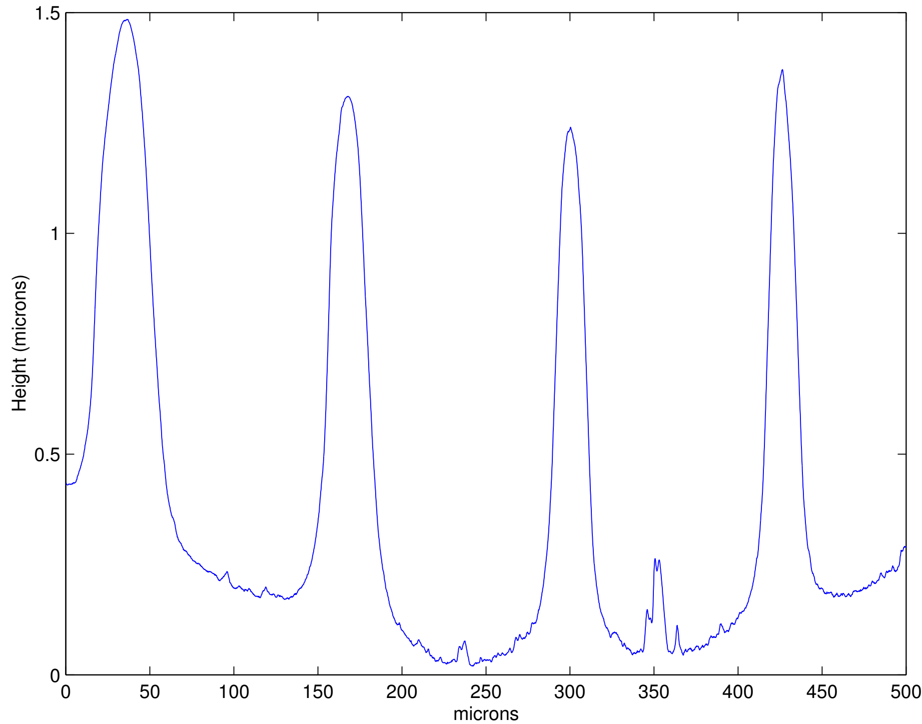

Figure 4.8: Etch profile of *Mylar*® after 10 minutes in an Ar/O_2 reactive ion etch.

- time: 60 seconds

Kapton® Channels

Kapton® is a resilient polyimide film with mechanical properties that can withstand temperatures in excess of 400 °C. The high chemical resistivity of Kapton® permits its use in a wide range of applications [5]. All of these properties make Kapton® a potential polymer material in which to build next-generation micro and nanofluidic systems. The fabrication procedures for machining fluidic channels in Kapton® are nearly the same as for Mylar®. The films used in these experiments were coated on one side with a silicone-based adhesive. The adhesive surface was used to attach test samples to silicon wafers. This gave the flexible films the mechanical stability necessary for electron-beam lithography.

Etching of Kapton® films was carried out in an RIE system using the identical mixture of oxygen and argon as in etching of Mylar® films. Figure 4.10 shows the surface profile of a film etched for 10 minutes. Figure 4.11 is a micrograph of an array of 50 nm channels etched in Kapton® film using the following conditions:

- O_2 flow rate: 70 sccm

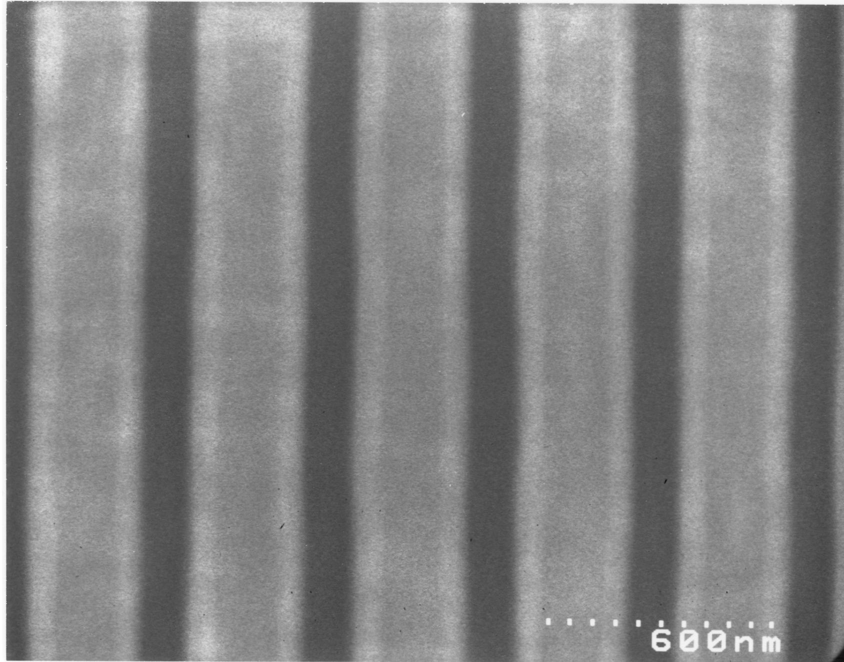

Figure 4.9: Channels etched in *Mylar*®using O_2 and Ar as the gas sources.

- argon flow rate: 14 sccm
- chamber pressure: 35 mTorr
- electrode spacing: 3 inches (7.6 cm)
- power level: 80 Watts
- lower electrode voltage: 450 V
- time: 60 seconds

One of the most common commercial uses for Kapton® is in the manufacture of flexible circuit boards. It serves as the insulating base material and mechanical support upon which metal wires are deposited. The established industry based on this type of manufacturing would be a great benefit to the development of fluidic devices integrated with electronics.

By heat sealing two pieces of Kapton® film together it is possible to fabricate hermetically sealed electronic circuit boards. It may be possible to heat seal fluidic channels machined in this material without collapsing or deforming the structures with the applied pressure by using sacrificial materials that could be removed after sealing the devices.

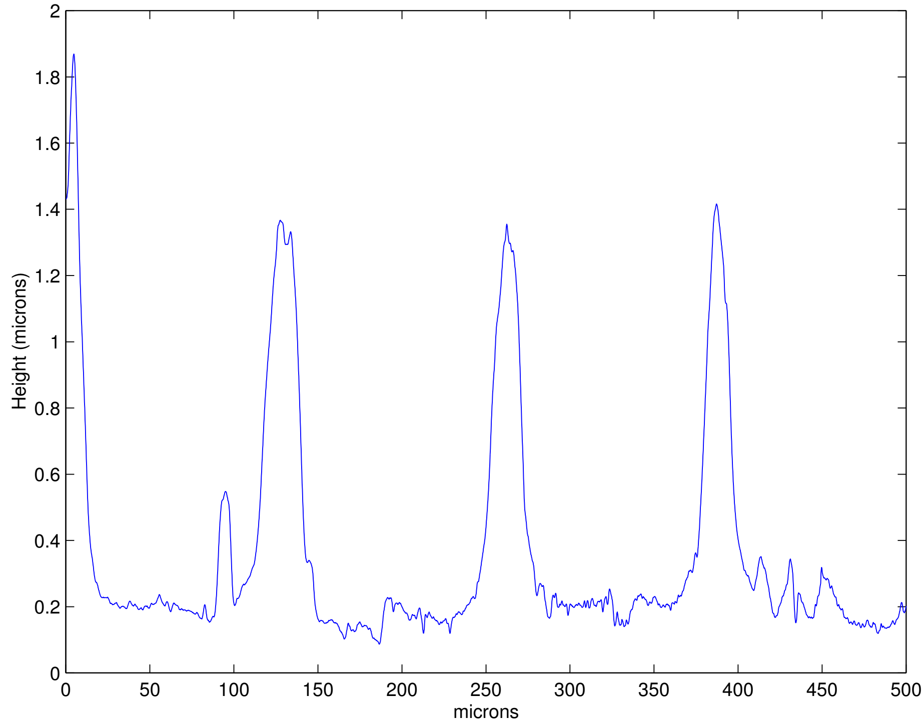

Figure 4.10: Etch profile of *Kapton*® after 10 minutes in an Ar/O_2 reactive ion etch.

4.4 Methods of Sealing Nanometer Fluid Channels

Fluid channels etched into the surface of a substrate need to be sealed in order to confine the fluid within the channel. The top layer used to seal the channel serves as the fourth wall of the channel, and therefore its surface properties can influence the fluid dynamics in the channel. Many techniques exist for bonding two glass slides, or bonding a glass slide to a silicon wafer. Most of these require some type of glass other than pure fused silica. In anodic bonding, the glass must have enough mobile ions that an electric current can be passed through it. In electrostatic bonding there must be enough ions present which are mobile at high temperatures, but held in position at operating temperatures of the device. Few of these methods are applicable to high purity fused silica because they all rely on certain modifications of the glass to facilitate the bonding. This section investigates a method developed for sealing fused silica channels by bonding two flat fused silica surfaces together.

4.4.1 Surface Preparation

The common feature of all of the bonding techniques discussed here is that two flat, polished pieces must be brought together under the proper conditions. The surfaces must be brought close enough

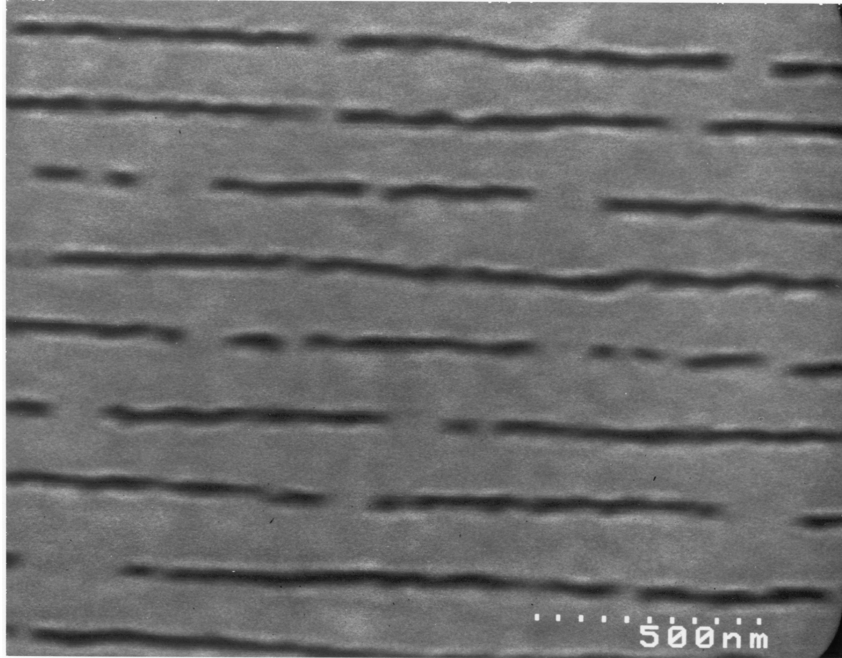

Figure 4.11: Channels etched in *Kapton*® using RIE with O_2 and Ar as the gas sources.

together that chemical bonds can bridge the gap between them. Both surfaces must be free from contaminants which may inhibit the chemical bonding, and have no large particles adhering that will prevent them from being brought into contact.

Removing chemical contaminants from surfaces is done by first removing the majority of surface contaminants before etching the glass in order to expose a fresh surface. A procedure specifically developed to clean silicon surfaces is the RCA etch discussed in Chapter 3. This process is also highly effective on silicon dioxide surfaces in a slightly modified form. One of the steps is a hydrofluoric acid etch, used to remove the thin surface oxide layer on silicon. When used on glass, this may cause unwanted surface roughness, or destroy micromachined features. Adapting the RCA etch for glass involves diluting the HF acid and reducing the duration of this etch.

Once the surfaces have been appropriately prepared, the next step is to bring them into contact with each other. This must be done without contaminating the clean surfaces. Allowing a meniscus of water to dry on the surface will concentrate any contaminants present in the water, and deposit them directly onto the surface that was just cleaned. One such method of avoiding surface contamination is to heat up the final water rinse almost to the boiling point, and then slowly remove the glass from the water. This must be done in an extremely clean environment, and all parts handled with clean tools. An alternative approach which does not require such stringent conditions is to place

the two surfaces in contact with each other prior to removing them from the final water bath. By pressing the two surfaces together an outward flow of water carries particles away from the interface. Provided the water is filtered and deionized (18 MΩ), and is kept under a laminar flow hood, this method has provided reliable and reproducible results for square 2.5 cm glass slides (6.25 cm^2 area).

4.4.2 Anodic Bonding

Anodic bonding is one of the more common techniques for bonding solid surfaces together. It is generally used to bond Silicon wafers to a glass cover slip. This is done by the application of an electrical current which locally heats the two surfaces through ohmic heating. This elevated temperature breaks local bonds and allows them to reform at the interface of the two materials. If the two surfaces are in close proximity, the new bonds will bridge the two surfaces together.

4.4.3 Fusion Bonding

One successful approach of bonding two surfaces is fusion bonding. This is done through breaking surface bonds by increasing the temperature above 800 °C. This is not a high enough temperature to break the Si-O bonds, but it is sufficient enough to remove the OH and H groups bonded to the surface. If two flat surfaces of silicon or glass are brought in close contact under these conditions, they will bond together. The surfaces must be clean and free from particle contaminants in order to form a complete bond. Due to the high temperatures involved, thermal expansion of the two surfaces being bonded together must be matched as closely as possible.

4.4.4 Room Temperature HF Bonding

The bonding approach used in this research was a room temperature HF bonding technique[6, 7]. In this process, two carefully cleaned glass surfaces are placed in contact with each other, and a small quantity of diluted HF is introduced at the interface. These two surfaces are held in contact for 24 hours to complete the bonding process[6].

The function of the HF is to break SiO2 bonds on the surface according to the reaction

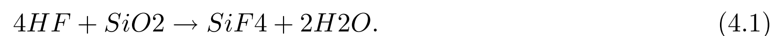

$$4HF + SiO2 \rightarrow SiF4 + 2H2O. \tag{4.1}$$

In this reaction, the products are not necessarily carried away. Instead, they are trapped at the interface unless they can diffuse out to the edges of the glass slides. For this reason it is difficult to

bond large surfaces with this technique.

4.5 Imaging Techniques for Fused Silica Fluid Channels

Imaging the finished fused silica channels in the scanning electron microscope requires that they must first be coated with a conductive metal layer prior to observation. Fine details are often hidden by this metal layer, but without it, the charging effects make observation nearly impossible[8]. In some cases it is possible to obtain a clean image by using high beam currents (greater than 100 pA) and low accelerating voltages. The micrograph in Figure 4.4 was taken with the metal etch mask still on the surface, but no additional metal was deposited. The side walls of the channels are uncoated fused silica. The detail visible on the walls is not typical of fused silica in a scanning electron microscope. There may be a small amount of surface contamination that was deposited during the reactive ion etch that enabled the details of the surface roughness to be discernible.

Atomic force microscopy was used as an alternative method to characterize nanofluidic channels. Figure 4.12 illustrates a fused silica channel surface map example obtained by atomic force microscopy.

4.6 Fluorescent Confocal Microscope Measurements

The purpose of this experiment was to study the motion of fluorescent labeled latex beads in fused silica nanofluidic channels. The results of these experiments are used in device design. In particular, methods of driving flow in nanometer size channels presented in the next chapter is based on the experimental results derived here. Another important result of these experiments is to demonstrate that particle and fluid mobility in sub-micron channels, although small, is large enough to be observable.

Electron-beam lithography was used to define arrays of lines from 100 nm (Figure 4.13) to 1 μm (Figure 4.15) in width. These patterns were then transferred to a metal etch mask by ion beam etching. The fused silica channels were then etched by reactive ion etching in a C_2F_6 plasma containing a small amount of argon.

Large connecting channels and fluid delivery reservoirs were defined using optical lithography and etched into the fused silica by hydrofluoric acid etching. Holes were drilled through the wafer using diamond drill bits and a slurry of abrasive aluminum oxide powder. Next the fused silica wafer was carefully cleaned using the RCA etch process and bonded to a similarly prepared cover

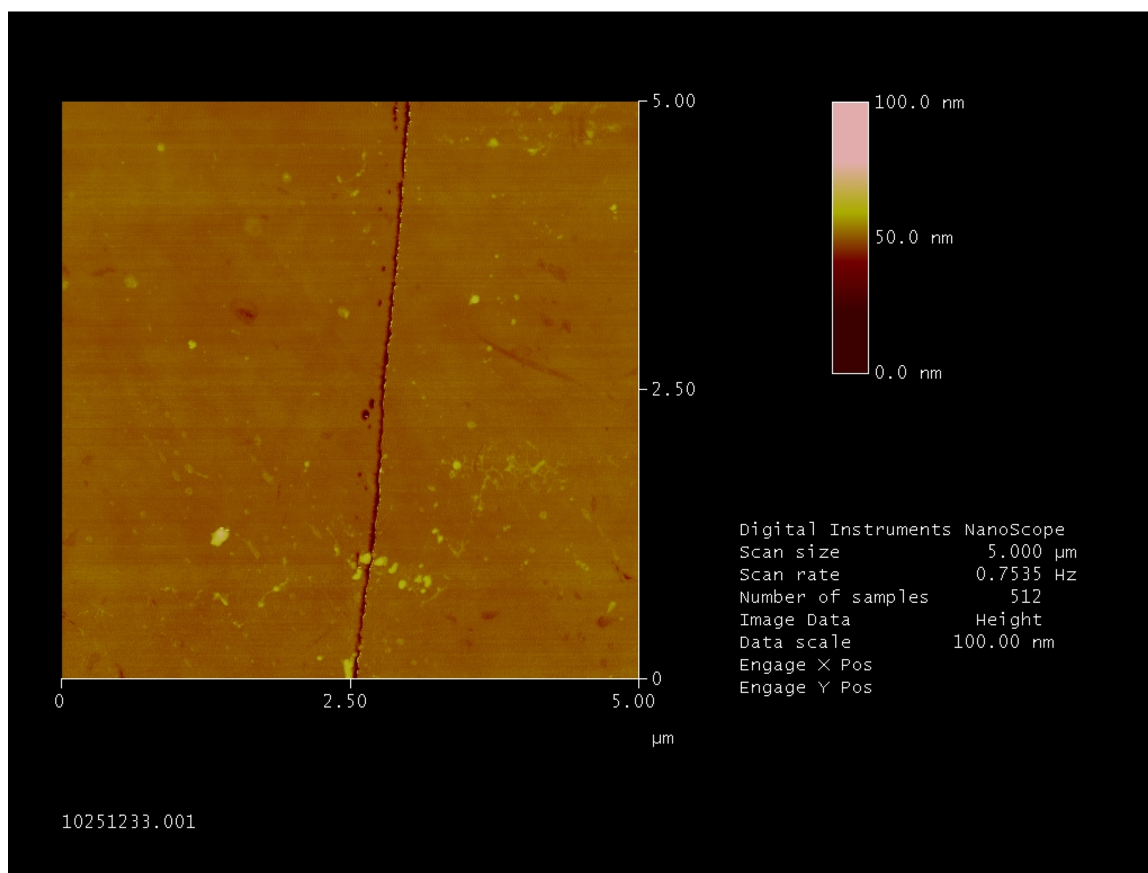

Figure 4.12: Surface map of channels in silicon dioxide obtained by atomic force microscopy.

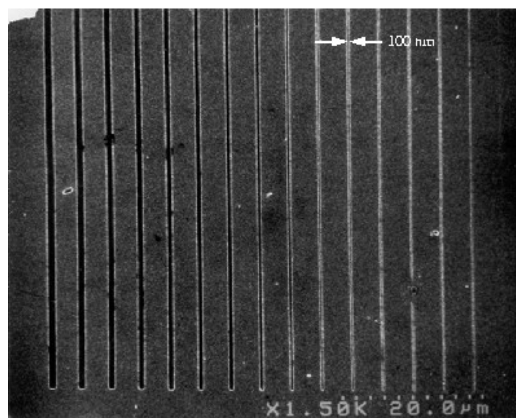

Figure 4.13: Fused silica fluid channels used in fluorescent confocal microscopy measurements.

slip using the room temperature HF bonding technique.

A drop of test solution was placed in each hole leading to a fluid reservoir. The holes were covered with microscope cover slips to reduce fluid evaporation.

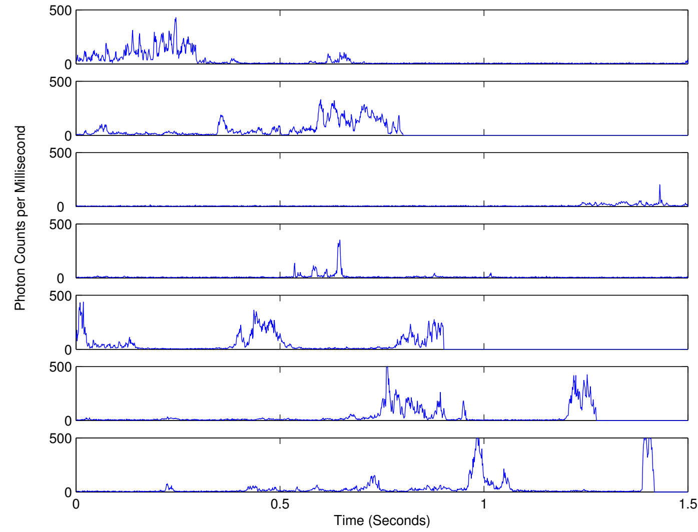

Figure 4.14: Fluorescent measurement on beads in the 100 nm wide, 100 nm deep channels shown in Figure 4.13.

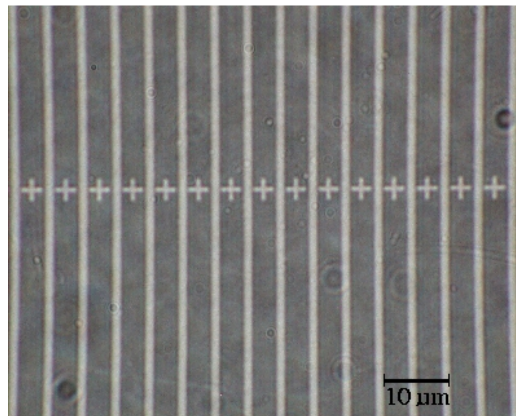

Figure 4.15: Fused silica fluid channels used in fluorescent confocal microscopy measurements. The channels are one micron wide spaced five microns apart. The row of "+" marks across the middle of the image are used in aligning the channels with the confocal microscope.

Measurements of fluorescent labeled latex spheres 63 nm in diameter moving in fused silica fluid channels were performed using a confocal microscope. Confocal microscopy is a technique that illuminates and collects light from a small region within a sample volume [9, 10, 11, 12].

The confocal microscope setup in Figure 4.17 was designed and built by Andrew Berglund [13]. It is designed to excite and collect a fluorescent signal from a small volume in the sample under investigation.

Figures 4.14 and 4.16 show results of fluorescent measurements at one position in two different channels. The peaks correspond to movement of fluorescent particles through the observation vol-

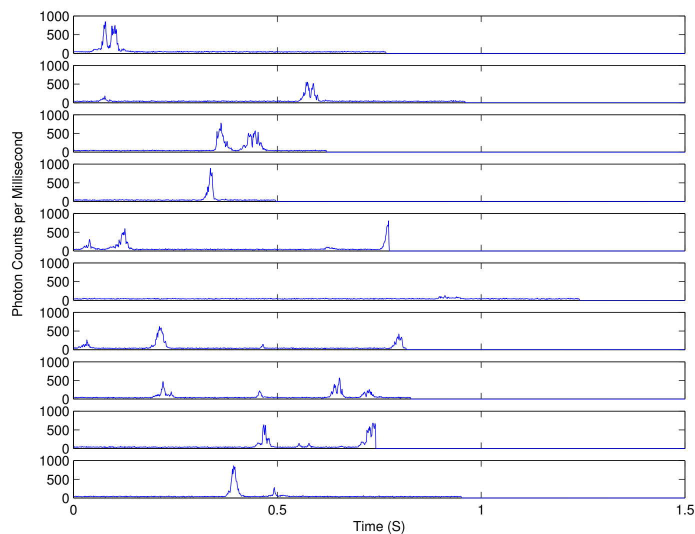

Figure 4.16: Fluorescent measurements on 63 nm beads in the 1 μm wide, 100 nm deep channels of Figure 4.15.

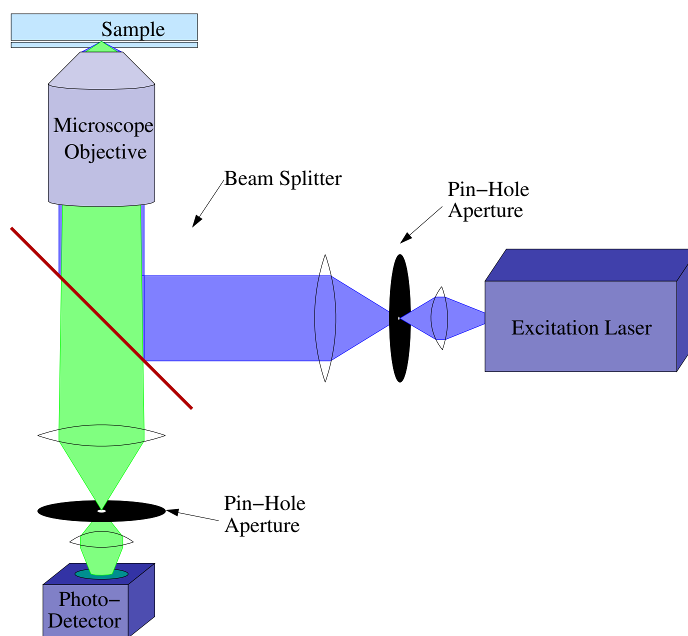

Figure 4.17: Confocal microscope configuration.

ume of the fluorescent confocal microscope. These experiments were performed with no pressure differential driving the flow, all particle movement was caused by Brownian motion.

4.7 Conclusion

The specific processing techniques presented here resulted from experimentation with many different approaches. These are the techniques that were found to be most suitable for building nanofluidic devices.

References

[1] Ilesanmi Adesida and Thomas E. Everhart. Substrate thickness considerations in electron beam lithography. *Journal of Applied Physics*, 51(11):5994–6005, November 1980.

[2] S. Wolf and R. N. Tauber. *Silicon Processing for the VLSI Era Volume 1 – Process Technology*. Lattice Press, 1986.

[3] Evangelos Gogolides, Philippe Vauvert, George Kokkoris, Guy Turban, and Andreas G. Boudouvis. Etching of SiO_2 in fluorocarbon plasmas: A detailed surface model accounting for etching and deposition. *Journal of Applied Physics*, 88(10):5570–5584, November 2000.

[4] K. Sasaki, H. Furukawa, K. Kadota, and C. Suzuki. Surface production of CF, CF_2 and C_2 radicals in high-density CF_4/H_2 plasmas. *Journal of Applied Physics*, 88(10):5585–5591, November 2000.

[5] Kapton® polyimide flim bulletin gs-96-7. Technical report, Du Pont High Performance Materials, P. O. Box 89, Route 23 South and Du Pont Road, Circleville, OH 43133, 2000.

[6] H. Nakanishi, T. Nishimoto, R. Nakamura, A. Yotsumoto, T. Yoshida, and S. Shoji. Studies on SiO_2-SiO_2 bonding with hydrofluoric acid. room temperature and low stress bonding technique for mems. *Semsors and Actuators A*, 79:237–244, 2000.

[7] Akihide Hibara, Takumi Saito, Haeng-Boo Kim, Manabu Tokeshi, Takeshi Ooi, Masayuki Nakao, and Takehiko Kitamori. Nanochannels on a fused-silica microstrip and liquid properties investigated by time-resolved fluorescence measurements. *Analytical Chemistry*, 74(24):6170–6176, December 2002.

[8] Y. C. Lin and Everhart T. E. Study on voltage contrast in SEM. *Journal of Vacuum Science and Technology*, 16(6):1856–1860, November/December 1979.

[9] R. Oldenbourg, H. Terada, R. Tiberio, and S. Inoué. Image sharpness and contrast transfer in coherent confocal microscopy. *Journal of Microscopy*, 172(1):31–39, October 1993.

[10] Jeff W. Lichtman. Confocal microscopy. In *Science's Vision: The Mechanics of Sight*, pages 76–81. Scientific American, Inc., 1998.

[11] Marcus Dyba and Stephan W. Hell. Focal spots of size $\lambda/23$ open up far-field florescence microscopy at 33nm axial resolution. *Physical Review Letters*, 88(16), April 2002.

[12] M. Minsky. Memoir on inventing the confocal scanning microscope. *Scanning*, 10(4):128–138, 1988.

[13] A. J. Berglund, A. C. Doherty, and H. Mabuchi. Photon statistics and dynamics of fluorescence resonance energy transfer. *Physical Review Letters*, 89(6):art. no.–068101, 2002.

Chapter 5

Pumping Liquids at Nanometer-Size Scales

5.1 Introduction

As the critical dimensions of fluid channels are reduced to sub-micron sizes, simply moving liquid through the channel becomes a substantial challenge. The traditional method of applying a pressure differential to either end of the channel to drive the flow is not very effective in nano-scale channels. This is due to increased interactions of fluid with the channel surfaces, and the fact that fluid viscosity in small dimensions differs dramatically from bulk fluids [1, 2]. For example, as the diameter of a fluid channel is decreased, the pressure differential necessary to maintain a certain flow velocity must increase. At some point the required pressure becomes unreasonably large [3].

5.2 Methods of Pumping Fluid in Nanometer Channels

This research requires control of particles and fluid in the channels under study. In an ideal situation, the particles move down the channel at an easily controlled velocity and do not exhibit random velocity fluctuations beyond what is expected from Brownian movement. Possible techniques of driving fluid include:

- Pressure Differential [4, 5, 6]
- Temperature Gradient [7, 8, 9, 10]
- Viscosity Gradient [7, 11, 12]
- Capillary Action [13]

- Electrolytic Gradient (osmotic flow) [14]
- Electrical Potential Gradient (Electro-Diffusion) [15, 16, 17, 10]
- Magnetic Driven Flow [18, 19]
- Acoustic Waves [20, 21, 22]
- Rectified Brownian Motion [23, 24, 25, 26, 27]
- Optical Radiation Pressure [28, 29, 30]
- RF Driven Flow

The principle of these techniques will be briefly discussed to compare their usefulness in various applications.

Pressure-Driven Flow:

Applying a differential pressure is the most common method of moving fluid through macroscopic water pipes and channels, and thus it is natural to consider this for micro-channels. Both Hagen (in 1839) and Pouseuille (in 1840) studied this problem in detail for fluid flow in capillary channels. The main assumption in both of their calculations was laminar or non-turbulent flow. Pouseuille studied this problem to understand how blood flows through capillary vessels in biological systems. The result of his analysis describes the flow velocity profile as having a parabolic cross section with a maximum flow rate in the center of the tube (Figure 5.1). The mathematical form of the Hagen-Pouseuille Law states that velocity of the fluid at a distance y from the center of a circular pipe of diameter d is given by

$$v = \frac{\Delta p}{4\mu l}(d/2 - y)^2, \tag{5.1}$$

where Δp is the pressure differential between two points separated by a distance l, and viscosity of the fluid is denoted by μ. This equation shows that the velocity of the fluid is zero at the pipe surface ($y = d/2$), and maximum velocity ($v_{max} = \frac{\Delta p}{16\mu l}d^2$) occurs at the tube center. The average velocity over the tube cross-section is $v_{avg} = \frac{\Delta p}{32\mu l}d^2$ [3].

The analytic solution of this problem assumes that the fluid layer adjacent to pipe walls has zero velocity. This assumption is often made in classical fluid mechanics. However, experimental results have shown that this assumption may not be valid for nano-scale fluid systems [2]. The second assumption is that shearing stress between adjacent layers is proportional to the rate of shear perpendicular to the direction of motion. The proportionality constant that relates rate of

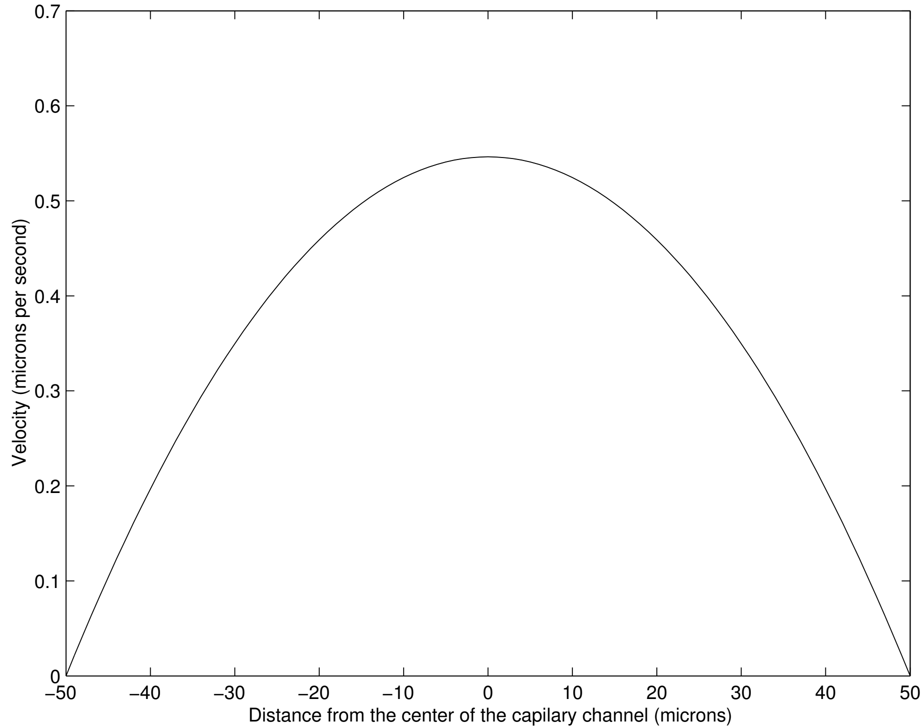

Figure 5.1: Velocity profile of pressure-driven flow in a capillary channel.

shear to shear stress is the fluid viscosity. There is evidence that viscosity derived for a bulk fluid does not directly apply to small volumes or to volumes of liquid near a solid interface [1, 2].

Temperature and Viscosity Gradient Driven Flow:

Thermophoresis is a well-known phenomenon that drives aerosol particles along a thermal gradient [31, 9, 32]. Convection currents due to thermal differences are observed in oceans, lakes and fluid containers. Temperature and viscosity gradient driven flow of thin liquid films on surfaces and in microfluidic systems has been demonstrated [7, 11, 12].

Capillary Flow:

Capillary action is a particularly interesting flow control method for microfluidics because it becomes more effective with smaller channels. Capillary action is primarily responsible for the initial filling of channels in micro- and nano-scale fluid systems [13]. Capillary flow is driven by a pressure differential that is dependent on the fluid surface tension, adhesive forces between the fluid and channel walls, and the channel diameter. The pressure differential is given by

$$P = \frac{2\gamma}{r}\cos(\Theta), \tag{5.2}$$

where γ is the surface tension of the fluid, r is the radius of the channel (for channels with circular cross-section), and Θ is the fluid-surface contact angle. The liquid-air interface velocity propagates at a velocity given by

$$v = \frac{Pr^2}{8\eta l}, \tag{5.3}$$

where P is the pressure given by Equation 5.2, η is viscosity, and l the capillary channel length [33]. A drawback of this approach is that once the channels are filled, the flow stops. Capillary action would be valuable for single use systems [34], but not for continuous flow, or reusable systems.

Osmotic Pressure:

Osmotic pressure differential arises from solute concentration gradients across porous membranes. The pores in a membrane consist of channels that selectively allow solvent to pass through, yet retain the solute. The selectivity is partially due to the physical size of the channels, and partially due to local electric fields that inhibit the flow of ionic solutes.

Electro-Osmotic Flow:

Electro-osmotic flow (EOF) is a method in which an electric field is used to move ions in the diffuse part of an electric double layer at a liquid-solid interface near channel walls. The motion of these ions drives the motion of the remainder fluid through viscous drag forces. This is the most promising alternative to pressure-driven flow in nanofluidic channels. One advantage to this technique is that plumbing special pressure control tubes onto a tiny chip is not required. This technique has been demonstrated by a number of different research groups using a variety of experimental setups [15, 35, 16, 17]. Remaining sections of this chapter will present how EOF was adapted in this research in sub-micron fluid channels.

Magnetic Flow:

The motion of magnetic particles suspended in fluid channels can be influenced with an externally applied magnetic field. One method of achieving precise control of these particles is to use electromagnet micro-probes. The work by Barbic et al. has demonstrated the ability to use this technique in a number of different types of fluid systems [19].

Acoustic Waves:

The Kundt tube is a device used to illustrate the concept of standing waves [36, 37]. It consists of a tube that is closed on one end and covered by an audio speaker at the other end [22]. The tube is filled with a lightweight powder such as cork dust. By exciting the speaker with a sine wave, a standing wave can be established in the tube. The dust in the tube collects at the nodes of the standing wave, and allows it to be visualized [38]. If the tube is made to have a speaker on each

end, the same effect would be seen if both speakers were driven with the same signal. If, on the other hand, the speakers were driven at slightly different frequencies, the group velocity of the wave inside the tube would no longer be zero. The node point would appear to move at a constant rate toward one of the speakers.

A similar concept has been demonstrated in capillary tubes filled with liquid by Araz, Lee, and Lal. They used ultrasonic transducers to set up standing waves inside a glass capillary tube. Particles suspended in the fluid collected at pressure node points. By varying the excitation frequency they were able to separate particles according to size [20, 21].

Another approach useful in microfluidics is a surface acoustic wave (SAW) device [39]. A channel molded in silicone rubber could be placed directly on a SAW device that would serve as the fourth wall of the channel. The Rayleigh wave on the SAW device surface could be used as a method of moving particles.

Rectified Brownian Motion:

The term Brownian ratchet refers to a general class of devices which perform some type of rectifying action to extract work out of randomly varying forces. Many variations of this approach have been used in microfluidic systems [23, 24, 25, 26, 27].

Optical Radiation Pressure:

The radiation force of a strongly focused light beam is sufficient to direct a particle's motion to the focus point of the light beam [28, 40, 41, 29, 30]. If this is used to move a particle in a channel, hydrodynamic coupling of the fluid with the particle will induce motion of the fluid in the channel as well [42].

RF driven flow:

Exciting an electromagnetic wave on a radio frequency transmission line in close proximity to a fluid channel could be used to interact with particles in the fluid. Particles with dielectric constants higher than water would be attracted to areas of higher field intensity, those with lower dielectric constants would be forced to areas of low field intensity. By controlling electromagnetic wave group velocity both the speed and direction of the particles could be controlled.

5.3 Conditions for Electro-Osmotic Flow (EOF) in Fluid Channels

In this section, a brief background of conditions necessary for sustaining EOF and controlling its properties is given. Next, an approach for how this can be implemented in channels built in silicon on insulator material is described. Finally the results of experiments performed to determine the effectiveness of this method are presented.

Electro-osmotic flow works by using an electric field to produce a motive force on ions in the solution of a capillary channel. The hydrodynamic coupling between those ions and the fluid will drive its motion and any neutral ions or particles that it contains [10, 35].

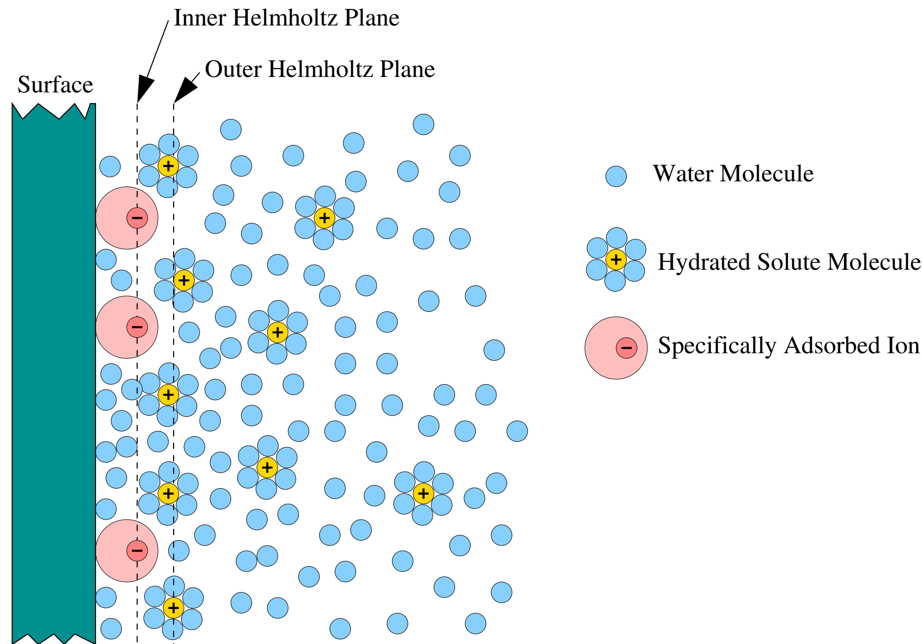

Figure 5.2: Electric double layer adjacent to a surface.

When an electric field is applied to an ionic solution, the ions in the bulk solution react by orienting themselves in a configuration that tends to cancel out, or reduce the magnitude of the electric field [43, 44]. However, the ions at or near a solid interface behave very differently as a result of the formation of the electric double layer [45].

The electric double layer begins to form when ions of the solution adsorb to the solid surface. This process can leave the solid surface with a net charge. These ions are called specifically adsorbed ions, because they must come out of solution and form a chemical bond with the surface. They must at least partially discard their hydration layer in order to come into close contact with the surface.

The specifically adsorbed ions create a sheet of charge which is very close to the solid surface, called the Helmholtz layer [45, 46, 47] shown in Figure 5.2.

The charge contained in the Helmholtz layer produces an electric field that attracts counter ions from the solution to the surface, and pushes away ions with the same charge sign as the Helmholtz layer. The counter ions will either become specifically adsorbed, thus reducing the charge of the Helmholtz layer, or they will become non specifically adsorbed. These latter ions are either not chemically reactive with the surface or not energetically able to discard their hydration layer in order to become specifically adsorbed. Because they retain their hydration layer, the effective radius of the non specifically adsorbed ions are larger than the atomic radius determined from crystal structures of ionic solids [43]. The presence of this hydration layer prevents the counter ions from approaching within a minimum distance of the surface. This minimum distance of approach defines the outer Helmholtz plane. The counter ions cannot form a charge density as high as the Helmholtz layer because of their mutual repulsion and also due to the presence of the hydration layer. As a result, the counter ions form a diffuse layer which extends into the solution [45, 48], and Figure 5.2.

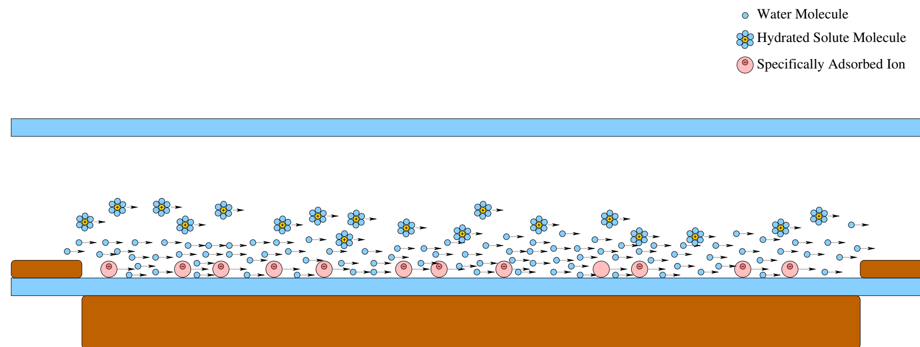

Figure 5.3: Electro-osmotic flow schematic illustrating water molecules, specifically adsorbed ions and hydrated solute molecules.

The configuration of the double layer is very important because it has created a layer of like charges that are spatially confined in a direction perpendicular to the surface through the local electric field from the Helmholtz plane, but not so tightly bound to the surface that they cannot move in directions parallel to the surface. The specifically adsorbed ions generally have a very low surface mobility because their movement along the surface would require continual breaking and reforming of chemical bonds. The surface mobility of the non specifically adsorbed ions increases as their distance from the surface increases, and these ions are free to move around. Because the majority of the ions in the diffuse layer are of one charge sign, it is not possible for them to negate

an externally applied electric field. If one applies an electric field parallel to the surface, the ions in the diffuse layer move under the force applied through this electric field creating a drift current (Figure 5.3).

It is important to observe that EOF is mainly a surface effect. The ions moving under the influence of the electric field are close to the surface of the channel walls. Ion flow in the diffuse layer will induce a flow in the rest of the fluid through hydrodynamic coupling. This will only work in small capillary channels with laminar flow characteristics. In large channels the hydrodynamic coupling would not be sufficient to drive flow throughout the channel. Thus EOF is not a valid method of driving fluid flow in fluid systems with large Reynolds numbers characteristic of turbulent flow.

5.3.1 Controlling the Properties of the Electric Double Layer

Properties of the electric double layer are essential for establishing electro-osmotic flow in capillary channels. This section presents a method which has been successfully used to control the properties of the electric double layer in order to control both direction and magnitude of EOF in a capillary channel [49].

Important parameters which determine properties of an electric double layer are the quantity of various ions dissolved in solution, their level of ionization, and their reactivity with the surface. The more relevant electric double layer property is ion density in the mobile part of the diffuse layer. This property is difficult to quantify because mobility and ion density in the diffuse layer varies continuously from the outer Helmholtz plane to the middle of the solution. Instead, a focus on the zeta potential, and the surface conductivity of ions in the diffuse layer is appropriate [16, 17]. Measurements of these quantities are relatively straightforward and related to the density and to the mobility of the diffuse layer ions. For simplicity, a "slipping plane" has been defined as the place where the ion mobility in the diffuse layer becomes significant. The voltage potential difference between the slipping plane and the bulk solution is defined as the zeta potential [48]. The zeta potential is important because its value is related to the magnitude of electro-osmotic flow [15].

The zeta potential can be influenced externally by either placing fixed charges in the walls of the channel, or by applying a potential to an electrode external to the channel walls. Schasfoort and his colleagues have done precisely this [15]. They demonstrated electro-osmotic flow in micro-fabricated channels in which both the direction and fluid flow rate were controlled simply by changing the potential applied to an electrode external and parallel to the channel walls.

5.3.2 Design of Electro-Osmotic Flow Channels

The required geometry for an EOF channel is one with cross-sectional dimensions less than a few microns. If the channel is made larger than this, the coupling between the electric double layer and the fluid in the channel will be too small to establish the required flow. The size of the channel at which this starts to become an issue is not a problem that will be addressed here, since the channels used in this study are smaller than many of the channels used in other EOF experiments.

The walls of the channel should be lined with a thin layer of electronic insulator material which is not chemically reactive with the solution that will be placed in the channel. Schasfoort used a free standing silicon nitride membrane that was a few hundred nanometers thick [15]. The electrodes used to apply the electric double layer control field were made from metal contacts deposited on top of these channels.

The approach used in this thesis research was to etch the channels into a conductive silicon surface. The silicon served as the control electrode, a second thin layer of silicon dioxide was grown on the surface as insulation between silicon electrode and solution which also provided a chemically inert, hydrophilic surface on the inside of the channel walls. This approach results in a simple geometry that lends itself to integration with other devices including electronics.

These channels can be sealed by anodic bonding of a glass plate to the top of the chip, or by adhering a piece of PDMS (silicone rubber) to the surface (Figure 5.4).

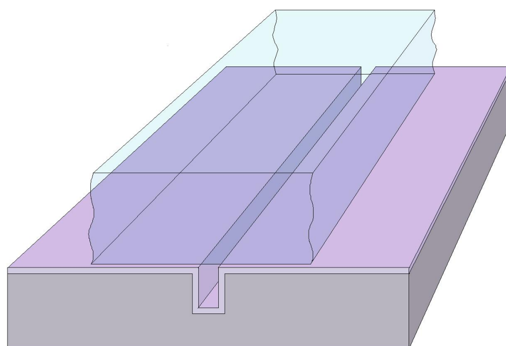

Figure 5.4: Channel etched in a silicon wafer and sealed with PDMS (silicone rubber).

While this geometry is sufficient for simply establishing electro-osmotic flow in a fluid channel, it would be even more useful if this geometry could be easily integrated with other components, such as capacitive electrodes placed on either side of the channel. The approach used in this work is to make the electrodes in the top silicon layer of a silicon-on-insulator wafer. The layer of oxide

below the top silicon layer will insulate the electrodes from the silicon substrate allowing them to be used for electrical measurements. The geometry of the electrodes have been designed such that they serve a second function as the side walls of the fluid channels. Figure 5.5 shows an example of how these same channels can be fabricated on a silicon-on-insulator wafer. The main difference of

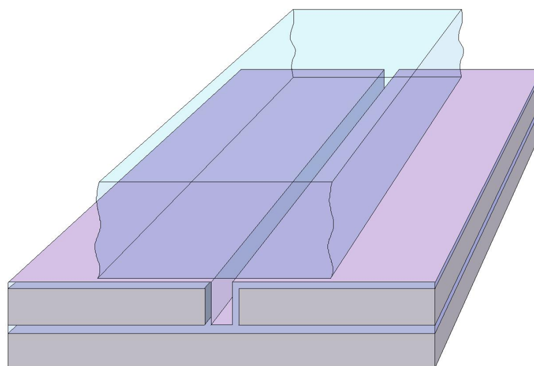

Figure 5.5: Channel etched in an SOI wafer and sealed with PDMS.

this geometry is that the control electrode is only on the channel bottom rather than on three sides. Applying a potential to the bulk silicon will result in a very different electric field inside the channel and will give rise to an electric double layer only on the bottom of the channel. The expected result of this would be a reduction of the magnitude of the EOF. This is acceptable as a design trade-off because this approach allows electrodes to be easily integrated with the channels.

If it becomes important to control the electric double layer on the vertical channel walls it is possible to apply a control voltage to the electrodes in the top silicon layer. This can be done because the control voltage will be a fixed potential and will not influence the small signal alternating current measurements of the electrodes.

The top silicon layer in Figure 5.5 will contain electrodes for sensing particles and molecules suspended in the channel fluid. This sensing will be done by exciting the electrodes with a small amplitude (<1 mV$_{p-p}$) signal. A variable control voltage can be added to this signal to control the electric double layer on the vertical channel walls.

The ability to independently control the voltage applied to the sides and to the bottom of the channel presents a very interesting situation that is worth looking at in more detail. If one wishes to control the motion of anions or molecules with a net negative charge, it may be possible to apply a positive potential to the bulk silicon wafer in order to attract the particles to the bottom of the channel. Once this is done, applying a lower potential, or even a negative potential to the sides of the

channel may result in an energy barrier that will prevent the charged particles from escaping from the channel and will also prevent new particles from entering. Using this approach, the channels would not have to be sealed on the top. Cleaning and reusing this type of channel could be done without disassembling a sealed device. In addition, introducing a test sample would be done by simply placing a drop of it on the surface.

5.3.3 Building the EOF Test Setup

To test the functionality of electro-osmotic flow, nine parallel 2.0 μm wide channels were defined through photolithography and subsequently etched into the top silicon layer of a silicon-on-insulator wafer (Figure 5.6). The reservoirs are placed at either end of a nanometer size fluid channel. The etching was performed using a custom built chemically assisted ion beam etching (CAIBE) system. This device ionizes Argon and accelerates the ionized gas with an energy of 500 eV. The beam travels a distance of 10 cm before reaching the sample. At a distance of approximately 2 cm above the sample, a sublimed vapor of XeF_2 is introduced to the ion beam. XeF_2 will spontaneously etch silicon isotropically. The effect of the ion beam is to increase the etch rate of the XeF_2 and to change the etch profile from being isotropic to having vertical side walls. Following this step the photo resist is removed in a plasma consisting of a mixture of argon and oxygen. In addition to removing photoresist from the surface, oxygen ions in the plasma assist in formation of a thin oxide layer on the freshly etched silicon surfaces.

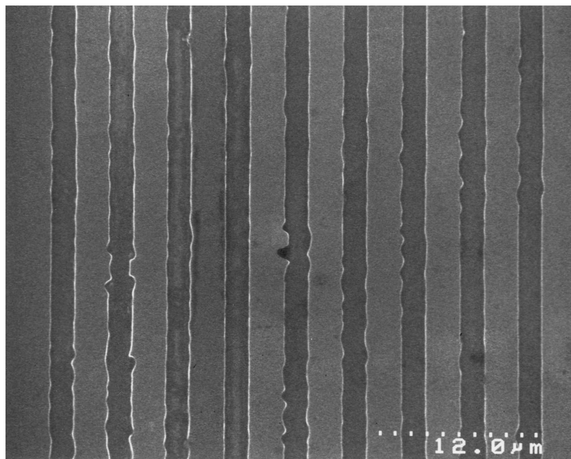

Figure 5.6: Scanning Electron Micrograph of the Channels.

Next a sealing layer of PDMS (GE Silicones RTV 656) was fabricated. First, the RTV 656 was mixed according to the directions from the manufacturer. Then the mixture was poured onto a 4

inch diameter silicon wafer that had been treated with a thin layer of TMCS (trimethyl chlorosilane) to allow the PDMS to be easily separated from the silicon wafer. The resulting PDMS material is approximately 4 mm thick. Two holes were made 1 mm in diameter and separated by 5 mm. The holes were punched using a piece of 12 gage stainless steel hypodermic tubing. Next a rectangle was cut out of the PDMS approximately the same size as the silicon chip with the channels in such a way that the holes would approximately line up with the fluid channels. This was cleaned in a warm bath of anhydrous methyl alcohol for 15 minutes. The bath was replaced every 5 minutes, and was heated just to the point where the methanol started to boil (about 90°C [50]). Upon removal from the methanol the PDMS was dried with nitrogen and placed on the SOI chip containing the channels. The holes in the PDMS were aligned with the channels with the aid of a dissecting microscope.

5.3.4 Measurement Circuit

The conductivity of fluid in the channel is measured by applying an AC signal at opposite ends of the channel and monitoring the resulting amplitude across a resistor placed in series with the channel. The resistor chosen in this case is a 1.00kΩ 1% metal film resistor. Frequency of the excitation signal is between 100 Hz and 1.5 kHz with an amplitude of approximately 3 volts.

Connections to the fluid channel are made by immersing a 25 μm diameter platinum wire in the PDMS fluid reservoirs as shown in Figure 5.7. These wires are connected to the measurement circuit by winding them around the connector terminals. The sample mounting stage is connected to the DC power supply that is used to set the control voltage. The silicon chip is clipped to this stage for mechanical support in addition to providing an electrical connection for the control voltage.

The 1kΩ resistor was chosen to be much smaller than the electrical resistance of the fluid channel, as a result the voltage drop across this resistor will be small in comparison to the applied signal. This voltage drop is measured with a lock-in amplifier[1]. The lock-in amplifier is set to differential input mode, input channel A is connected directly to the output of the function generator, and channel B is connected to the circuit node common to the 1 kΩ resistor and the fluid channel. The final measurement circuit configuration is shown in Figure 5.8.

5.3.5 Experimental Results of the EOF test setup

Testing these channels is done by measuring the ionic conductivity of different solutions placed in the channels as a function of the control voltage. Two 100 mM solutions of $NaCl$, and $NaSO_4$ were

[1] Model 5210 manufactured by Signal Recovery, formerly EG&G.

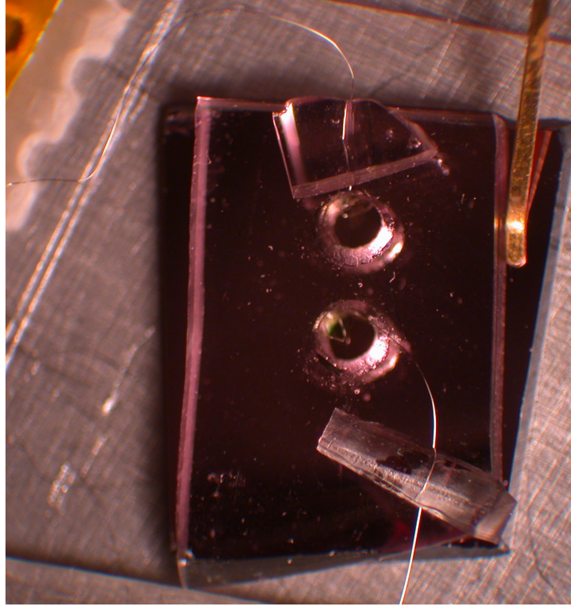

Figure 5.7: Photograph of the measurement setup showing PDMS reservoirs and platinum wire electrodes.

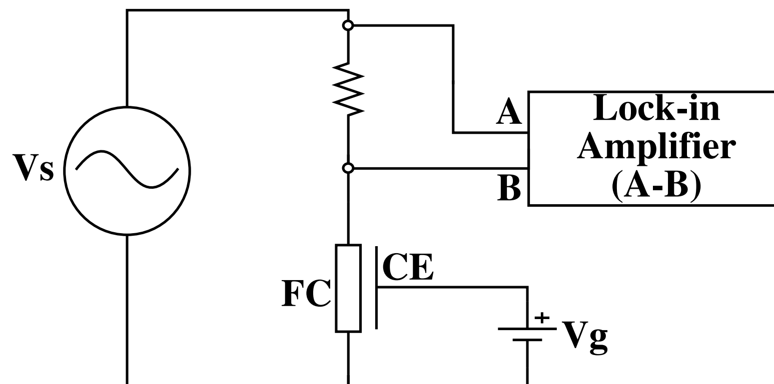

Figure 5.8: Measurement circuit; FC = fluid channel, CE = control electrode, Vg = control voltage to the back side of the silicon chip, Vs = excitation signal from the function generator.

prepared. The first two experiments measure the conductivity; first with deionized water, then with the 100 mM $NaCl$ solution in the channels. In each case 5 μl of test solution was placed in each fluid reservoir. The differential voltage across the $1k\Omega$ resistor measured with the lock in amplifier was used to calculate the conductivity of the channel for each data point using the equation:

$$Conductivity = \frac{1}{1k\Omega + 1k\Omega * 3.0V/V_{A-B}}, \tag{5.4}$$

where V_{A-B} is the amplitude of the voltage drop across the $1k\Omega$ resistor. The results of this measurement are shown in Figure 5.9. This measurement was taken at a frequency of 1.131 kHz.

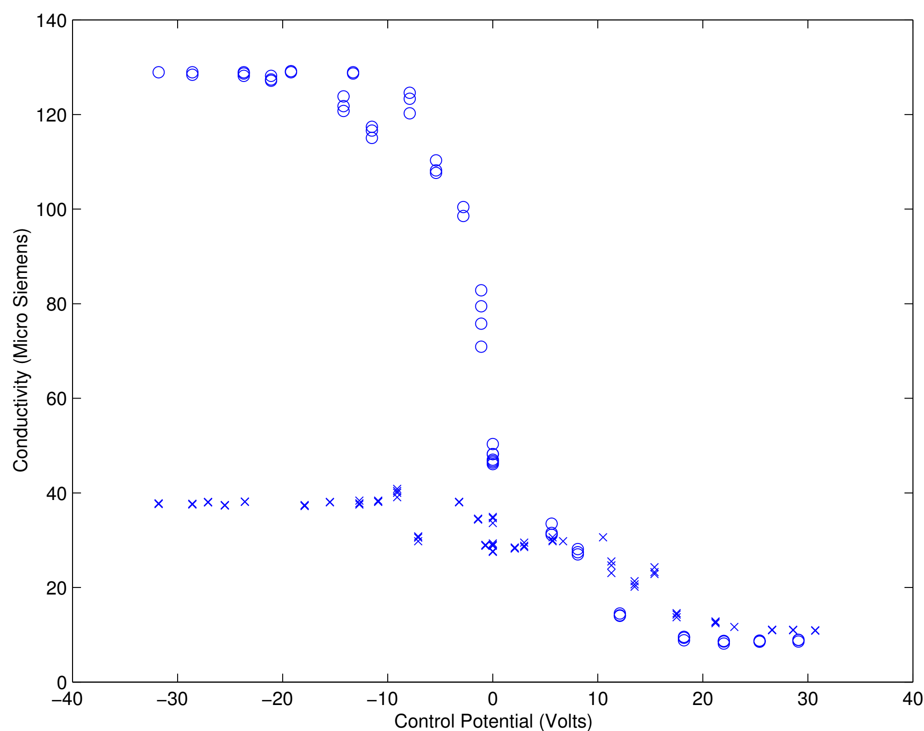

Figure 5.9: Conductivity of channels with 100 mM NaCl solution (x) and deionized water (o).

The second experiment demonstrates that the conductivity is a result of ions moving in the channel, instead of just along the interface between the PDMS and the silicon chip. This was done by first measuring the conductivity with the PDMS fluid reservoirs connected by the channels, and then moving the PDMS piece to an area of the same chip where there are no fluid channels. In both measurements the working fluid was a 100 mM solution of $NaSO_4$, and the measurement frequency was 400 Hz. Figure 5.10 shows the results of this experiment. This data has also been treated according to Equation 5.4.

5.4 Conclusion

Pressure driven flow may cause channels to clog as large particles are forced into narrow constrictions. Electro-osmotic flow applies a driving force only to particles and fluid within the channel, therefore decreasing chances of channel blockage. Control over flow rate and direction is far superior for EOF than for many alternative methods of driving fluid flow. The ability to drive flow in many channels

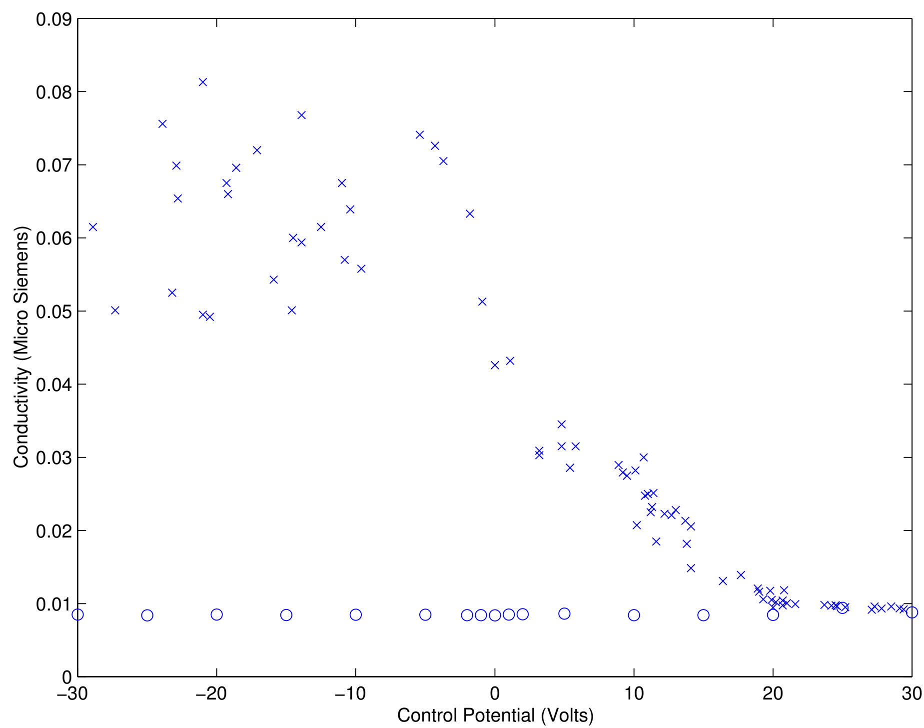

Figure 5.10: 100 mM $NaSO_4$ solution (x) compared against a control experiment in which no channels were present on the silicon chip (o).

simultaneously within a small area on a chip is another advantage of this technique.

Fluid sample introduction is done by placing a drop of solution in a fluid reservoir connected to the channel. This simplicity is a great advantage in developing miniaturized portable chemical analysis systems. This eliminates the need for complex and bulky fluid delivery systems.

References

[1] Liudmila A. Pozhar. Structure and dynamics of nanofluids: Theory and simulations to calculate viscosity. *Physical Review E*, 61(2):1432–1446, 2000.

[2] L. Cheng, P. Fenter, K. L. Nagy, M. L. Schlegel, and N. C. Sturchio. Molecular-scale density oscillations in water adjacent to a mica surface. *Physical Review Letters*, 87(15), October 2001.

[3] Russel A. Dodge and Milton J. Thompson. *Fluid Mechanics*. McGraw-Hill Book Company, Inc., New York and London, first edition, 1937.

[4] C. L. Hansen, E. Skordalakes, J. M. Berger, and S. R. Quake. A robust and scalable microfluidic metering method that allows protein crystal growth by free interface diffusion. *Proceedings of the National Academy of Sciences of the United States of America*, 99(26):16531–16536, 2002.

[5] Mark A. Unger, Hou-Pu Chou, Todd Thorsen, Axel Scherer, and Stephen R. Quake. Monolithic microfabricated valves and pump by multilayer soft lithography. *Science*, 288:113–116, April 2000.

[6] J. Liu, C. Hansen, and S. R. Quake. Solving the "world-to-chip" interface problem with a microfluidic matrix. *Analytical Chemistry*, 75(18):4718–4723, 2003.

[7] Phillip Espinasse. Light directs fluid flow. *OE Magazine*, 3(10):7,9, October 2003.

[8] Nicholas Garnier, Roman O. Grigoriev, and Micael F. Schatz. Optical manipulation of microscale fluid flow. *Physical Review Letters*, 91(5), August 2003.

[9] I. S. Abdul-Khalek and D. B. Kittelson. Real time measurement of volatile and solid exhaust particles using a catalytic stripper. *Society of Automotive Engineers*, (950236), 1995.

[10] Royal Eugene Collins. *Flow of Fluids through Porous Materials*. Reinhold Chemical Engineering Series. Reinhold Publishing Corporation, 1961.

[11] Susan Daniel, Manoj K. Chaudhury, and John C. Chen. Fast drop movements resulting from the phase change on a gradient surface. *Science*, 291:633–636, January 2001.

[12] Brett A. Buchholz, Wei Shi, and Annelise E. Barron. Microchannel DNA sequencing matricies with switchable viscosities. *Electrophoresis*, 23:1398–1409, 2002.

[13] Akihide Hibara, Takumi Saito, Haeng-Boo Kim, Manabu Tokeshi, Takeshi Ooi, Masayuki Nakao, and Takehiko Kitamori. Nanochannels on a fused-silica microstrip and liquid properties investigated by time-resolved fluorescence measurements. *Analytical Chemistry*, 74(24):6170–6176, December 2002.

[14] Bertil Hille. *Ionic Channels of Excitable Membranes*. Sinauer, second edition, 1992.

[15] Richard B. M. Schasfoort, Stefan Schlautmann, Jan Hendrikse, and Albert van den Berg. Field-effect flow control for microfabricated fluidic networks. *Science*, 286:942–945, 1999.

[16] Sarah Arulanandam and Dongqing Li. Determining ζ potential and surface conductance by monitoring the current in electro-osmotic flow. *Journal of Colloid and Interface Science*, 225:421–428, 2000.

[17] Liqing Ren, Carlos Escobedo-Canseco, and Dongqing Li. A new method of evaluating the average electro-osmotic velocity in microchannels. *Journal of Colloid and Interface Science*, 250:238–242, 2002.

[18] A. Hatch, A. E. Kamholz, G. Holman, P. Yager, and K. F. Bohringer. A ferrofluidic magnetic micropump. *Journal of Microelectromechanical Systems*, 10(2):215–221, 2001.

[19] M. Barbic. Magnetic wires in mems and bio-medical applications. *Journal of Magnetism and Magnetic Materials*, 249(1-2):357–367, 2002.

[20] C. Lee and A. Lal. Low-voltage high-speed ultrasonic chromatography for microfluidic assays. In *Proceedings of the Solid State Sensor and Actuator Workshop*, pages 206–209, Hilton Head Island, South Carolina, 2002.

[21] M. K. Araz, C. H. Lee, and A. Lal. Ultrasonic separations in microfluidic capillaries. In *Proceedings of the IEEE-UFFC Conference*, Hawaii, 2003. IEEE.

[22] R. B. Hastings and Yung-Yao Shih. Experiments with an electrically operated kundt tube. *American Journal of Physics*, 30:512–516, 1962.

[23] Deniz Ertas. Lateral separation of macromolecules and polyelectrolytes in microlithographic arrays. *Physical Review Letters*, 80(7):1548–1551, February 1998.

[24] Joel S. Bader, Richard W. Hammond, Steven A. Henck, Michael W. Deem, Gregory A. McDermott, James M. Bustillo, John W. Simpson, Gregory T. Mulhern, and Jonathan M. Rothberg. DNA transport by a micromachined Brownian ratchet device. *Proceedings of the National Academy of the Sciences of the United States of America*, 96(23):13165–13169, November 1999.

[25] Gary W. Slater, Hong L. Guo, and Grant I. Nixon. Bidirectional transport of polyelectrolytes using self-modulating entropic ratchets. *Physical Review Letters*, 78(6):1170–1173, February 1997.

[26] Alexander van Oudenaarden and Steven G. Boxer. Brownian ratchets: Molecular separations in lipid bilayers supported on patterned arrays. *Science*, 285:1046–1048, August 1999.

[27] R. Dean Astumian and Peter Hänggi. Brownian motors. *Physics Today*, 55(11):33, November 2002.

[28] A. Ashkin. Acceleration and trapping of particles with radiation pressure. *Physical Review Letters*, 24(4):156–159, January 1970.

[29] Thomas T. Perkins, Stephen R. Quake, Douglas Smith, and Steven Chu. Relaxation of a single DNA molecule observed by optical microscopy. *Science*, 264:822–826, May 1994.

[30] Steven Chu. Laser manipulation of atoms and particles. *Science*, 253:861–866, August 1991.

[31] Frascisco. J. Romay, Sho. S. Takagaki, David. Y. H. Pui, and Benjamin. Y. H. Liu. Thermophoretic deposition of aerosol particles in turbulent pipe flow. *Journal of Aerosol Science*, 29(8):943–959, 1998.

[32] N. P. Rao, N. Tymiak, J. Blum, A. Neuman, H. J. Lee, S. L. Girshick, P. H. McMurray, and J. Heberlein. Hypersonic plasma particle deposition of nanostructured silicon and silicon carbide. *Journal of Aerosol Science*, 29(5/6):707–720, 1998.

[33] Edward W. Washburn. The dynamics of capillary flou. *Physical Review*, 18(3):273–283, March 1921.

[34] David D. Cunningham. Fluidics and sample handling in clinical chemical analysis. *Analytica Chimica Acta*, 429:1–18, 2001.

[35] Benedict S. Gallardo, Vinay K. Gupta, Franklin D. Eagerton, Lana I. Jong, Vincent S. Craig, Rahul R. Shah, and Nicholas L. Abbott. Electrochemical principles for active control of liquids on submilimeter scales. *Science*, 283:57–60, 1999.

[36] Jearl Walker. *The Flying Circus of Physics*. John Wiley and Sons, Inc., 1977.

[37] Howard S. Seifert. A miniature kundt tube. *American Journal of Physics*, 7:421–422, 1939.

[38] Robert A. Carman. Kundt tube dust striations. *American Journal of Physics*, 23:505–507, 1955.

[39] Gordon S. Kino and John Shaw. Acoustic surface waves. *Scientific American*, 227(4):50–68, 1972.

[40] A. Ashkin. Atomic-beam deflection by resonance-radiation pressure. *Physical Review Letters*, 25(19):1321–1324, November 1970.

[41] A. Ashkin. Optical trapping and manipulation of neutral particles using lasers. *Proceedings of the National Academy of Sciences of the United States of America*, 94:4853–4860, May 1997.

[42] Cristina Rusu, Ronny van't Oever, Meint J. de Boer, Henri V. Jansen, J. W. (Erwin) Berenschot, Martin L. Bennink, Johannes S. Kanger, Bart G. de Grooth, Miko Elwenspoek, Jan Greve, Jürgen Brugger, and Albert van den Berg. Direct integration of mircomachined pipettes is a flow channel for single DNA molecule study by optical tweezers. *Journal of Microelectromechanical Systems*, 10(2):238–245, June 2001.

[43] Linus Pauling. *General Chemistry.* Dover Publications Inc., 1988.

[44] Edward M. Purcell. *Electricity and Magnetism.* McGraw-Hill, Inc., 1985.

[45] Allen J. Bard and Larry R. Faulkner. *Electrochemical Methods Fundamentals and Applications.* John Wiley and Sons, Inc., 2001.

[46] Achim Van Theemsche, Johan Deconinck, and Leslie Bortels. Numerical solution of electroosmotic flow in a "flow field effect transistor". *Analytical Chemistry*, 74:4919–4926, 2002.

[47] Achim Van Theemsche, Johan Deconinck, Bart Van den Bossche, and Leslie Bortels. Numerical solution of a multi-ion one-potential model for electroosmotic flow in two-dimensional rectangular microchannels. *Electrochimica Acta*, 48:3307–3312, 2003.

[48] Herbert A. Laitinen and Walter E. Harris. *Chemical Analysis An Advanced Text and Reference.* McGraw-Hill, Inc., second edition, 1975.

[49] R. Qiao and N. R. Aluru. Ion concentrations and velocity profiles in nanochannel electroosmotic flows. *Journal of Chemical Physics*, 118(10):4692–4701, March 2003.

[50] Susan Budavari, editor. *The Merck Index.* Merck & CO., Inc., 12th edition, 1996.

Chapter 6

Nanogap Capacitive Sensing Electrodes

6.1 Introduction

Electrodes with nanometer spacings can be used to detect a number of properties of liquids, solutions, and colloidal suspensions. Incorporating sensing electrodes in nanometer-size fluid channels is exciting from the point of view of system integration.

Effective electrode design must consider optimization of geometry to maximize the signal. This will depend on what is being measured, and the size scales necessary. Designing nanometer spaced electrodes for sensing application requires calculation of basic information such as order of magnitude capacitance, expected signal levels, and fabrication techniques. One key feature of this design approach is the use of matched nanogap electrode pairs. The advantage of using paired gap electrodes will become clear when the details of the measurement circuit are presented in the next chapter.

6.2 Nanogap Electrode Overview

Recent developments in nanometer spaced electrode applications have focused on measuring the properties of single molecules, or small ensembles of molecules. Nanogap electrodes have been used in single electron transistors, electrical tunnel junctions, particle detectors, and chemical sensors. The methods of building these structures as well as their application have been rapidly developing. Combining the nanometer spaced electrodes with sub-micron fluid channels presents the possibly of a new class of analytical instruments for interrogating fluid samples.

In this work, the primary concern is to measure electrode capacitance changes resulting from various contents of a fluid channel. Methods developed in this chapter for calculating electrode

capacitance are used in the electrode design.

Developing a method of electrically sensing particles requires a sensitive measurement system that can operate in a noise filled environment. Accomplishing this type of measurement requires modeling the electrode, suspended particles, and fluid interactions. The models described here are used in the next chapter to develop the measurement approach.

6.3 Nanogap Electrode Capacitance Calculations

The capacitance between two nanometer spaced electrodes can be calculated in a number of different ways. In this section two main approaches are considered. The first technique is an analytical calculation, the second is a finite element model of the device. Both of these approaches have advantages and disadvantages. The analytical solution makes some very drastic geometric simplifications, but it provides valuable insight into relationships of physical dimensions to capacitance values. Using finite element models allows investigating more representative geometries, resulting in greater accuracy and more quantitative results. Finally, these techniques will be used to estimate the capacitance change when a particle is present between a pair of nanogap electrodes.

6.3.1 Analytic Calculations

For an arrangement of electrodes, analytical methods of calculating capacitance are highly dependent upon the specific geometry of the situation. For many situations this is best approached through numerical integration. The drawback to numerical integration is that it does not provide the same level of intuition or illustrate as clearly how different parameters effect the end result as do analytical solutions. In the case of this problem, it would be very helpful to arrive at some analytical solution for a problem with a very similar geometry to the electrodes on either side of the channel. The objective of the analytical calculation presented here is to obtain an equation in order to develop physical intuition of capacitance between nanogap electrodes.

In discussing capacitance, the traditional approach is to consider a parallel plate system. The equation that describes the capacitance of two parallel plate conductors is

$$C = 4\pi\epsilon_0\epsilon_r\frac{A}{d}, \tag{6.1}$$

where ϵ_0 is the permeability of free space, ϵ_r the relative permeability of the material between the capacitor plates, with areas given by A and separated by a distance d. The derivation of this equation

assumes fringing fields at the edges of the plates can be neglected. This assumption is valid in cases where the plate spacing is small compared to the plate dimensions. However it no longer holds for nanogap electrode geometries, where the conductor spacing is within an order of magnitude of the conductor dimensions (see Figure 6.1).

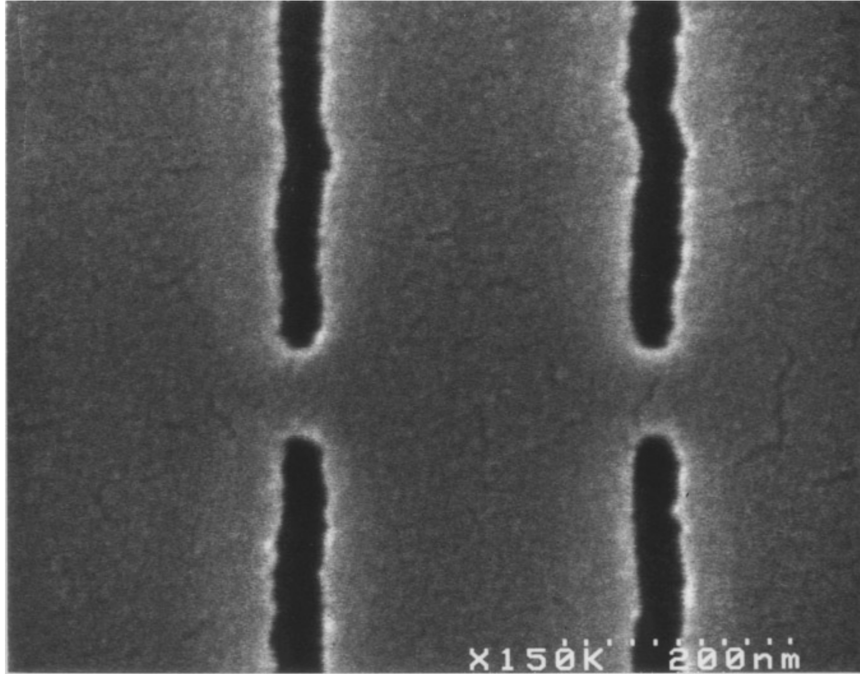

Figure 6.1: Electron-beam lithography used to define electrodes with a spacing of approximately 50 nm.

By approximating the electrode tips as spherical conductors (Figure 6.2) the geometry is greatly simplified, however errors result. This geometry is useful for analytical calculations to estimate the capacitance. In the finite element method calculations, the errors resulting from this approximation

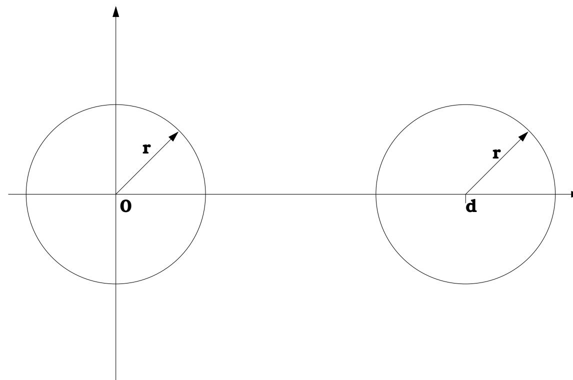

Figure 6.2: Geometry for electrode calculation.

are quantified.

The method of image charges is a technique where a charge distribution in free space is arranged to create equipotential surfaces corresponding to the surface of the conductors [1]. The total charge placed within each equipotential surface is then used to calculate capacitance. In this way, introducing the conductors will not influence the electric fields set up by the point charges.

For the simplified case of two spheres, this approach rapidly converges to a stable solution with a small number of point charges. First a charge q_1 is placed at the center of the first sphere. Setting this surface to the desired potential is done by adjusting the magnitude of this charge. This charge results in an equipotential surface at the first sphere with the potential given by:

$$V = \frac{q_1}{4\pi r \epsilon_r} \tag{6.2}$$

where r is the radius of the sphere. To simplify the calculations, this is set to one volt by making q_1 equal to $r4\pi\epsilon_r$.

As a result of this charge, the surface of the second sphere is not an equipotential surface. This is corrected by placing a charge of appropriate magnitude $q_2 = -q_1 r/d$ (d is the spacing between the sphere centers) and position $p_2 = d + r^2/d$.

Next a point charge is placed in the first sphere to return its surface to an equipotential of one volt. This process is repeated until a sufficient accuracy is achieved. Table 6.1 lists an example Matlab™ code implementing this algorithm.

The capacitance between the spheres is then calculated according to the equation:

$$C = \frac{(q_1 - q_2)/2}{(v_1 - v_2)}, \tag{6.3}$$

where q_1 and q_2 is the total charge placed within the first and second spheres, respectively. The denominator, $(v_1 - v_2)$ is the potential difference between the two spheres.

6.3.2 Finite Element Modeling of the Capacitance Between Two Spheres

Calculating capacitance using a finite element equation solver can provide quantitative results requiring fewer geometrical simplifications in comparison with an analytical approach. This is done with FlexPDE™ [2], a software package from PDE Solutions Inc.

```
epsilon_0=8.85418781761e-12; %Farads per meter
epsilon_r=1.00059; %Relative dielectric constant of air Purcell P.350
v1=1; %Volts. Potential of sphere 1
v2=0; %Volts. Potential of sphere 2
a=1e-6; %Radius of sphere 1 in meters
b=1e-6; %Radius of sphere 2 in meters
c=4e-6; %Distance between the centers of the spheres in meters
q1(1)=a*v1*4*pi*epsilon_0*epsilon_r;
p1(1)=0;
q2(1)=-b*q1(1)(c-p1(1));
p2(1)=c-b^2(c-p1(1));
for i=2:100,
q1(i)=-a*q2(i-1)p2(i-1);
p1(i)=a^2p2(i-1);
q2(i)=-b*q1(i)(c-p1(i));
p2(i)=c-b^2(c-p1(i));
end
capacitance=(sum(q1)-sum(q2))(2*(v1-v2))*10^18 %capacitance in attofarads
```

Table 6.1: Matlab code for calculating the capacitance between two spheres using the method of image charges[1].

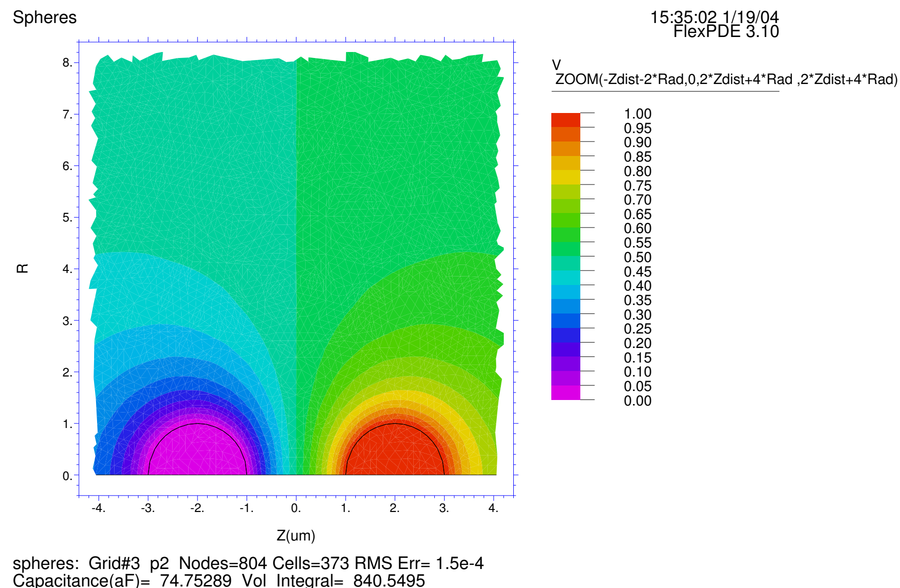

Figure 6.3: Finite element model results showing the potential distribution between two spheres used to calculate their capacitance of 74.75289 aF.

6.3.3 Finite Element Modeling of the Capacitance Between a Pair of Nanogap Electrodes

Due to the radial symmetry of the problem investigated here, a full three-dimensional solution is not necessary. Instead the problem is solved in cylindrical coordinates. Surface and volume integrals

are independent of the θ coordinate, so this part of the integral becomes simply 2π. The geometry

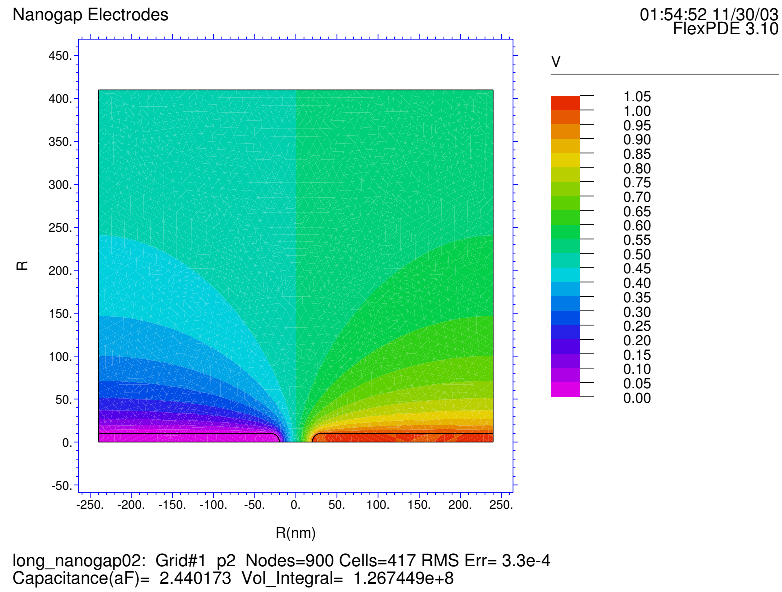

Figure 6.4: Finite element model calculation of the potential distribution between two nanogap electrodes and the capacitance of the system.

considered is that of one of the pair of electrodes in Figure 6.1. One conductor is set to ground potential, the other is set to one volt. Laplace's equation

$$\nabla^2\Phi = 0, \tag{6.4}$$

where Φ is the potential is used to calculate the electric field due to the potentials of the conductors [3]. The energy stored in the electric field is the volume integral

$$U_E = \frac{1}{2}\int_V \vec{D} * (\nabla\Phi) dV, \tag{6.5}$$

where $\vec{D}$ is electric flux density and $\vec{E} = \nabla\Phi$ is the electric field. The capacitance is calculated from the energy stored on a capacitor charged to a potential V [4];

$$U_E = \frac{1}{2}CV^2. \tag{6.6}$$

6.3.4 Change in Nanogap Electrode Capacitance in the Presence of a Nano-particle

By monitoring the capacitance of a set of nanogap electrodes, it is possible to detect particles drifting past the electrodes by measuring momentary electrode capacitance changes. In this section, finite element modeling is used to calculate the change in capacitance, and thus the signal level that is expected.

The presence of a metallic particle between two electrodes does not necessarily imply an increase in capacitance. The details of whether the capacitance should increase, decrease, or stay the same are highly dependent on the relative physical dimensions involved. To illustrate this, consider the simple case of the parallel plate capacitor (Equation 6.1). Much of our intuition about capacitance is derived from the equation for a parallel plate capacitor. This equation assumes that the fringing fields at plate edges contain a negligible portion of the total capacitive energy. In the case of nanogap electrodes, this is no longer a valid assumption, and this equation does not apply.

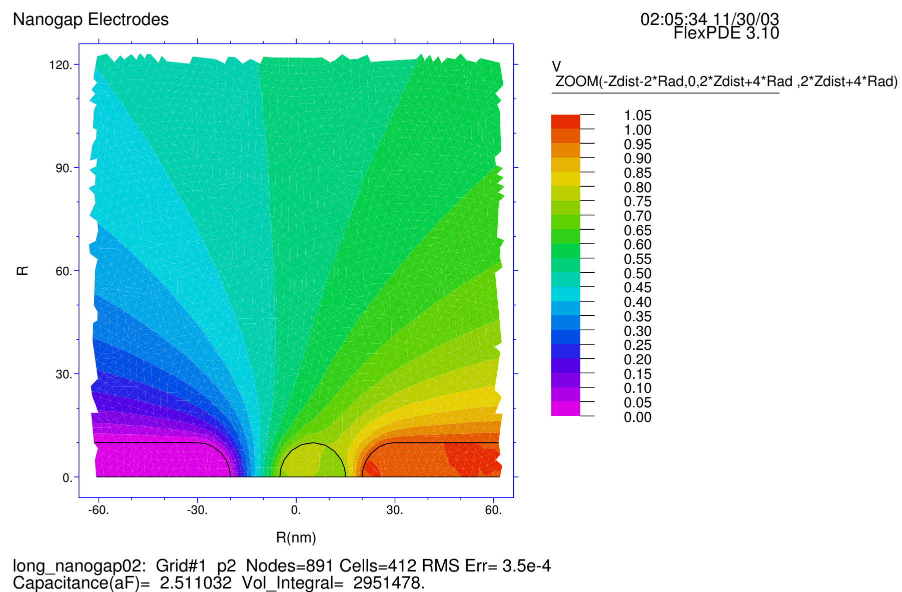

Figure 6.5: Finite element model calculation of the potential distribution between two nanogap electrodes with a particle present between them offset 5 nm to the right of center.

The geometry of Figure 6.1 was used to calculate the change in capacitance expected when a 20 nm diameter gold particle is present between the electrodes. A sample calculation result is shown in Figure 6.5. In this particular example the particle position is offset by 5 nm from center. The capacitance change is dependent on the particle position. The minimum change (1.1% increase)

occurs when the particle is equidistant from both electrodes, and maximum (6.2% increase) when the particle is in contact with one electrode.

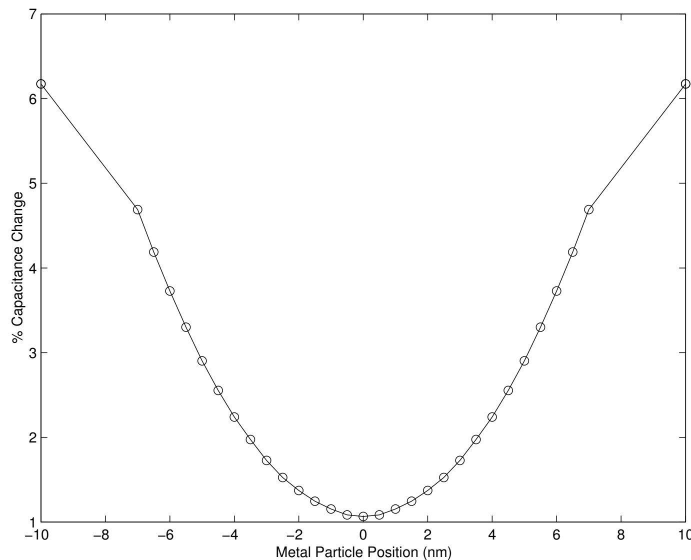

Figure 6.6: Calculated capacitance change as a function of particle position between the nanogap electrodes from the finite element model simulations.

Capacitances in the attofarad range can be measured using sensitive bridge circuits such as the Andeen-Hagerling AH2700A [5], and the General Radio 1615-A [6]. However, measuring changes of a few percent of these capacitances would push the resolution limits of these instruments. The next chapter will investigate circuit configurations that allow this measurement to be performed.

6.4 Nanogap Electrode Design

This section reviews a number of important design considerations for nanogap electrode measurement systems. The designs considered here employ reference capacitors value matched to the nanogap electrode capacitance. This simplifies balancing of the sensitive bridge circuits described in the next chapter, and eliminates a number of parasitic capacitances that interfere with measurements.

The fabrication approach used in this research is electron-beam lithography and shadow evaporation. The electrodes used in this work are designed to be integrated with fluid channels from 20 to 100 nm wide made with electron-beam lithography or shadow masking.

Measuring attofarad capacitances is exceedingly difficult in practice. In fact there are only a few commercial capacitance bridges which claim attofarad resolution [5, 6]. One of the reasons for this difficulty is that in many measurement systems, the parasitic capacitances of the cables alone can be

on the order of picofarads. Also, the smallest available reference capacitor that has sufficiently low loss and stability of its capacitance value is 10 pF [7, 8]. The goal of this measurement, however, is not to obtain a measurement of the gap electrode capacitance absolute magnitude, rather the objective is only a measurement of the relative capacitance change as particle pass by the gap electrodes. Therefore, the reference capacitor can be machined on the same chip as the fluidic channel and the gap electrodes (Figure 6.7). If the general form of the reference capacitor and the gap electrode are made with similar geometries, matching their values can be done without having an explicit knowledge of the exact capacitances. This approach also reduces some of the parasitic capacitance of the cables that would be necessary with a reference capacitor not integrated on the same chip as the device.

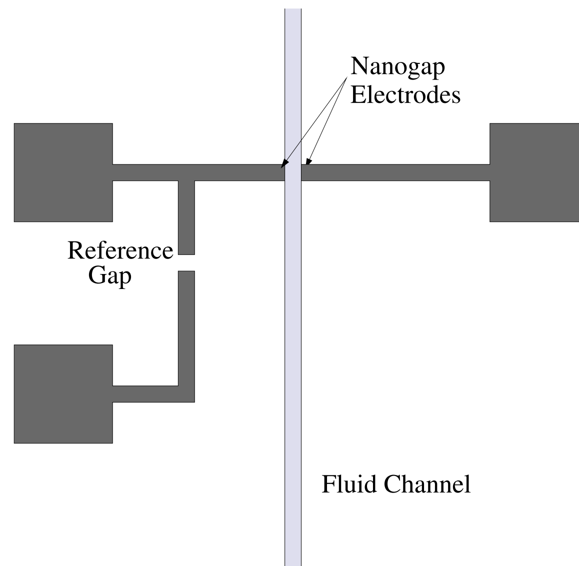

Figure 6.7: Possible configuration in which a reference gap electrode is machined on the chip at the same time as the sensing nanogap electrode.

The drawback to this approach is that each device must be made for a specific permittivity of the working fluid. If the working fluid is an electrolytic solution, the real component of the impedance of the gap electrodes will not be compensated for by the reference capacitor. The best way to ensure matching of the impedance between the reference gap and the measurement gap is to fill the reference gap with the same working fluid as the measurement gap.

By building the reference capacitor on the same channel as the gap electrodes as shown in Figure 6.8, the problem of matching the capacitance of the two capacitors is greatly simplified. This geometry will enable close matching of the capacitors in a wide variety of different liquids with

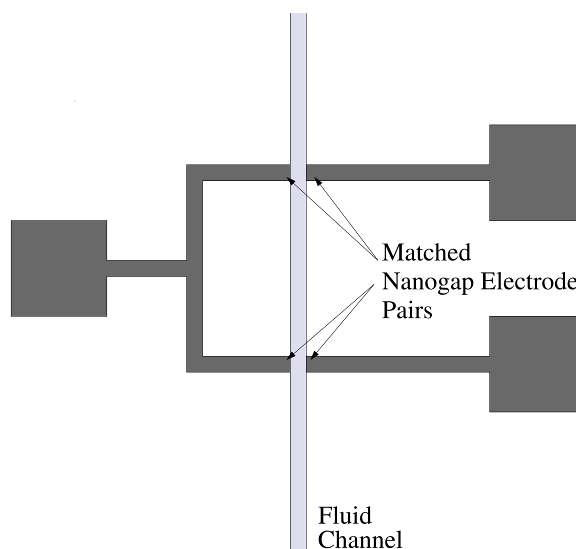

Figure 6.8: Configuration using a pair of nanogap electrodes on the same fluid channel.

different permeabilities. The electrical measurement of this circuit will show signals from both pairs of gap electrodes. The response of one electrode will be positive, the other will be negative. The difference in sign allows the signal from one electrode to be separated from the signal from the other electrode. The passage of a single particle will result in two pulses; one positive and one negative. This situation can be used to advantage while analyzing the data, because the time separation between the positive and negative pulses can be used to calculate the speed at which the particle moves down the channel.

6.5 Conclusion

The calculations present the expected capacitance values of nanogap electrodes. In performing measurements with these electrodes, the percent change in the capacitance value is what will ultimately determine signal levels.

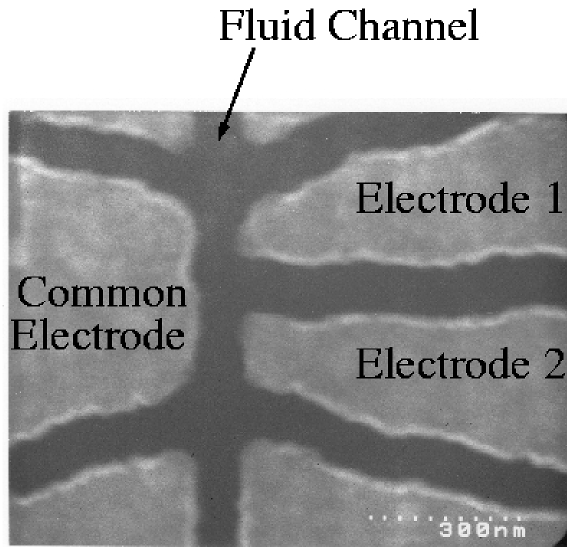

Figure 6.9: Example of a device containing a matched pair of nanogap electrodes with one electrode in common. The substrate material is Kapton®.

References

[1] William R. Smythe. *Static and Dynamic Electricity.* McGraw-Hill Book Company, Inc., 1939.

[2] Flex PDE™. Technical report, PDE Solutions Inc.

[3] Simon Ramo, John R. Whinnery, and Theodore Van Duzer. *Fields and Waves in Communication Electronics.* John Wiley & Sons, Inc., third edition, 1993.

[4] J. David Irwin. *Basic Engineering Circuit Analysis.* Macmillan Publishing Company, fourth edition, 1993.

[5] Andeen-Hagerling, 31200 Bainbride Road, Cleveland, Ohio 44139-2231 U.S.A. *AH2700A 50Hz-20kHz Ultra-precision Capacitance Bridge*, 2001.

[6] Massachusetts General Radio Company, West Concord. Capacitance bridge. *The Review of Scientific Instruments*, 33(11), November 1962.

[7] Yicheng Wang. Frequency dependence of capacitance stantards. *Review of Scientific Instruments*, 74(9):4212–4215, September 2003.

[8] Neil M. Zimmerman, Mahmoud A. El Sabbagh, and Yicheng Wang. Larger value and SI measurement of the improved cryogenic capacitor for the electron-counting capacitance standard. *IEEE Transactions on Instrumentation and Measurement*, 52(2):608–6, April 2003.

Chapter 7

Electrical Measurement

7.1 Introduction

The capacitance calculations performed in the previous chapter predict small capacitance values of the electrodes. The presence of conductive particles between a pair of nanogap electrodes results in a 1% to 6% capacitance increase. This section investigates a number of capacitance measurement approaches in order to select the optimum measurement approach.

7.2 Types of Measurement Circuits

There exist many techniques for measuring capacitance. The objective of this section is to briefly introduce common measurement circuit approaches and select the most promising for use with nanogap electrodes [1]. The selection criteria are resolution, accuracy, stability, and ability to monitor small changes in capacitance value. For measuring capacitance changes of nanogap electrodes as particles move through the gap, a circuit that is sufficiently sensitive to detect the resulting change in capacitance is critical.

7.2.1 Charge/Discharge Technique

Capacitance is the property that relates the amount of charge on a condenser to its voltage potential,

$$C = Q/V, \qquad (7.1)$$

where C is capacitance, Q the charge, and V the potential difference. Capacitance is measured by comparing the voltage potentials of an unknown capacitor with a known capacitor when they contain the same quantity of charge. In practice this is done by placing a fixed, but unknown quantity of

charge on the unknown capacitor, and measuring its potential. Then that entire quantity of charge is transferred to a precisely known reference capacitor, and its potential is measured. The unknown capacitance (C_{meas}) can then be calculated from the voltage ratio (V_{ref}/V_{meas}) and the reference capacitor value (C_{ref});

$$C_{unknown} = C_{ref} \frac{V_{ref}}{V_{meas}} \tag{7.2}$$

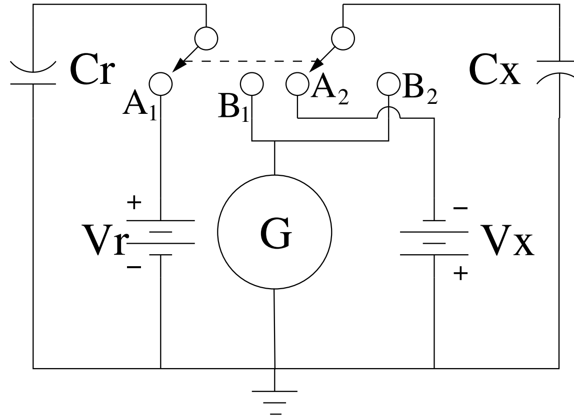

Figure 7.1: Charge/discharge circuit proposed by Lord Kelvin.

Lord Kelvin described a variation of this circuit in which both the reference capacitor and the capacitor being measured are charged with approximately equal and opposite quantities of charge (Figure 7.1). Once charged, the two switches in Figure 7.1 are moved to positions B_1 and B_2 connecting the capacitors together, if the charges on each capacitor are truly equal, no current pulse will be measured. The voltage to which each capacitor is charged is varied until no current pulse is measured in the galvanometer [2].

This is a simple and reliable method of measuring capacitance, however the method is not appropriate in this research for a number of reasons. First, this circuit is more suited to measuring fixed capacitor values, while the present research requires continuously monitored capacitance [1]. Second, this approach becomes less useful at lower capacitance values where effects due to stray capacitances become significant. The expected capacitance values for this research are on the order of femtofarads or smaller. For these capacitance ranges, the charge/discharge method is not practical. A circuit which is more immune to stray capacitances would be preferred. Finally, in practice this circuit is not very sensitive to small changes in capacitance. This is especially true in the present case where the potential difference across the unknown capacitor must remain below the level which would break down the fluid in the electrode gaps.

7.2.2 Oscillator Circuit Methods

Oscillation methods of capacitance measurement use the unknown capacitor as part of the feedback loop of an oscillator circuit (Figure 7.2). The advantage to this technique is that frequency of the oscillator is the measured parameter from which capacitance is calculated. Frequency can be measured with a high degree of accuracy. This type of circuit, however, is sensitive to stray capacitances and is not suited to measurement of absolute capacitances. This circuit is extremely valuable in monitoring small changes in a capacitance value. For example Green and Cunliffe used this type of circuit to obtain a resolution of 10^{-17} F [3]. To achieve this they used a feedback circuit to adjust bias voltage on a voltage controlled capacitor to keep the circuit tuned to optimum conditions. The capacitance values encountered in this research would result in high oscillation frequencies. The high loss component would make the quality factor[1] of the inductive-capacitive feedback circuit low, resulting in a less accurate frequency measurement.

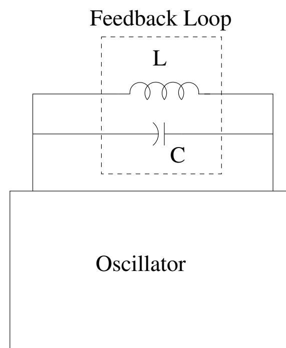

Figure 7.2: Oscillator capacitance measurement circuit.

7.2.3 Inductive-Capacitive Resonator Circuit

The inductive-capacitive (LC) resonator circuit places a known inductor in parallel with the capacitor that is to be measured (Figure 7.3). This configuration is commonly known as a “tank circuit.” The unique property of this circuit is its well defined resonance frequency; $f = \frac{1}{\sqrt{LC}}$. Measuring the circuit peak frequency response is done by monitoring amplitude response while sweeping the frequency of a sinusoidal excitation signal. Low capacitance values and high loss components result in a low quality factor of the resonator circuit. This means that the resonant peak will not be well defined, as a result lower accuracy measurement of the resonant peak frequency will result. Nanometer scale electrodes are expected to have small capacitance values with high loss components.

[1]The quality factor, or Q-factor is defined as the ratio of total stored energy to the input energy of one cycle.

This will result in a high resonance frequency with a poorly defined peak. Therefore this approach is not practical for nanometer scale electrode systems.

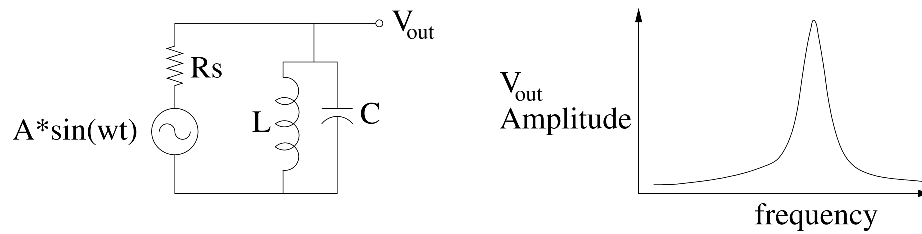

Figure 7.3: Inductive-capacitive resonator circuit.

This circuit can also be used to measure the change in a capacitive value by exciting the circuit just below the resonance peak and monitoring the response amplitude. If the capacitance increases by a small amount, the response amplitude will increase by an amount proportional to the resonance peak slope of the circuit.

7.2.4 AC Bridge Circuit

An AC (alternating current) bridge circuit (Figure 7.4 b) is similar to a Wheatstone bridge (Figure 7.4 a). Circuit sensitivity depends on how closely the bridge is matched, and the type of null reading device used. A high level of accuracy is possible by using synchronous detection (Lock-in amplifier) for reduced noise sensitivity. Parasitic capacitance can still be significant in some situations. Because two capacitors are being compared, the influence of parasitic capacitances can be made negligible by careful circuit construction to ensure that parasitic capacitances are matched as closely as possible. One way of ensuring this is to build the reference capacitor on the same chip as the sensor electrodes.

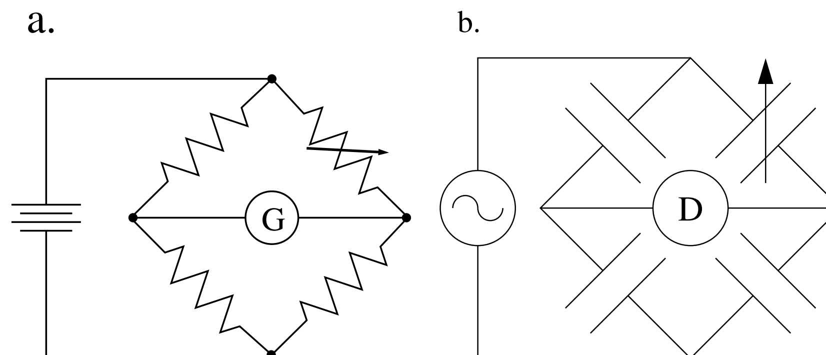

Figure 7.4: a. Wheatstone bridge for comparing resistances, G is a galvanometer. b. AC capacitance bridge for measuring capacitances, D is a phase sensitive detector.

In much of the present work, measuring an absolute capacitance value was not necessary. Instead, sensing very small relative changes in the sensor capacitors was extremely important. If this circuit can be balanced closely enough, the sensitivity can be made quite high. By building the reference capacitor on the same chip as the sensor electrodes, it is possible to match their values by simply adjusting their geometries. Even then, using external circuit components to fine tune the balance of the bridge may still be necessary.

The half of the AC bridge circuit that does not contain the capacitor being measured can be replaced with any type of variable impedance device. For practical purposes, constructing a variable capacitor with the required levels of accuracy and linearity is difficult. This half of the circuit could easily be replaced with a resistive divider circuit which uses a calibrated decade resistor. A similar approach is to use a precision ratio transformer. This device is very similar in operation to a decade resistor, however it has greatly increased linearity and stability. For example the precision decade potentiometer model number DP 1211 from Tegam has a linearity of ± 15ppm, and their model DT72A decade transformer has a linearity of ± 0.9ppm. The next section will describe these concepts in greater detail.

7.3 Precision Ratio Transformer Balancing of the AC Capacitance Bridge

The precision ratio transformer (PRT) is a variable transformer with a precisely adjustable turn ratio. Commonly available PRTs usually have a turn ratio that is adjustable with up to seven digits of precision. One common use of the PRT is in calibrating test and measurement equipment. The linearity and gain of an amplifier (e.g. the vertical deflection amplifier in an oscilloscope) can be measured by using a PRT to generate a signal with an amplitude that is a known fraction of the amplitude of a reference signal. The output is then measured with the amplifier and compared to the input. The PRT is an entirely passive device containing no amplifiers, its linearity and precision is only dependent on the physical construction of the transformer coils [4, 5].

Each decade of the precision ratio transformer consists of eleven sections of wire wound around a common magnetic core. In order to ensure linearity of the device, each section of wire must be as close to the same length as possible, and must be wound around the core the same number of times. The most important part of construction is that before wires are wound on the core, they are first loosely braided and twisted together. This achieves two objectives: first it makes sure

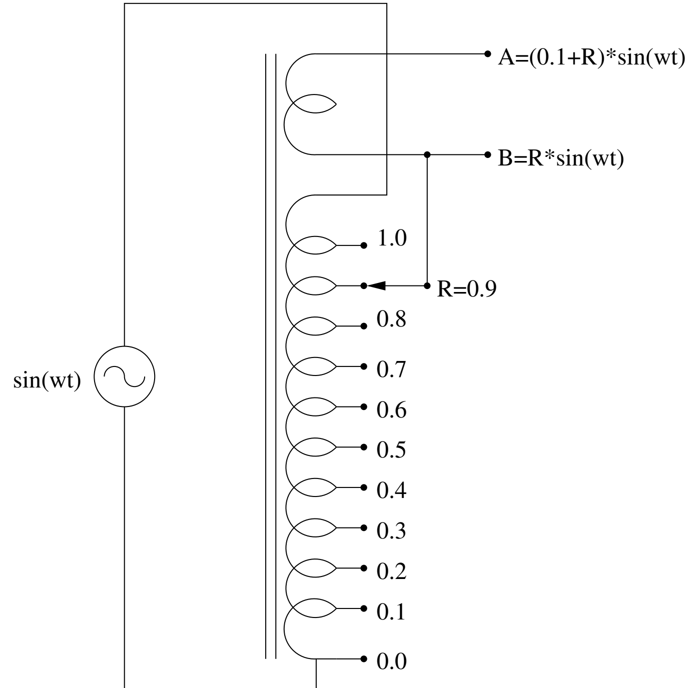

Figure 7.5: Single decade ratio transformer.

that every loop of wire sees almost the same magnetic flux, and second, it helps to ensure that any unwanted signals have nearly the same effect on the induced current in each coil. The drawback of this approach is that the capacitance between the coils can be quite large. As a result, the optimum operational frequency of most PRTs is less than 1 kHz. While they can be used at higher frequencies, their performance is reduced. Problems with different phase shifts and capacitive coupling between coils can lead to increased nonlinearities.

Each decade of the PRT requires 10 equal coils to achieve the output ratios of 0.0, 0.1, ... 1.0. The signal from the first ratio transformer is used to excite the common mode of the next decade transformer. The eleventh coil is used to excite the next decade transformer with a difference mode signal amplitude 10% of the first coil. Only the difference mode signal will give rise to a magnetic flux in the transformer core. In Figure 7.5 the top (secondary) coil with wires labeled "A" and "B" is used to excite the next decade transformer primary coil. Notice that the difference mode with which the next decade will be excited is $\frac{1}{10} * \sin(\omega\tau)$. The secondary will also be excited with the common mode signal $R_1 * \sin(\omega\tau)$. The output tap of the primary coil of the second decade will be $R_1 + \frac{1}{10}R_2 \sin(\omega\tau)$. Figure 7.6 shows an example with three decades. Notice that the output in this case is $(R_1 + R_2\frac{1}{10} + R_3\frac{1}{100}) \sin(\omega\tau) = (0.6 + 0.04 + 0.009) * \sin(\omega\tau)$.

In addition to calibrating test and measurement equipment, precision ratio transformers are

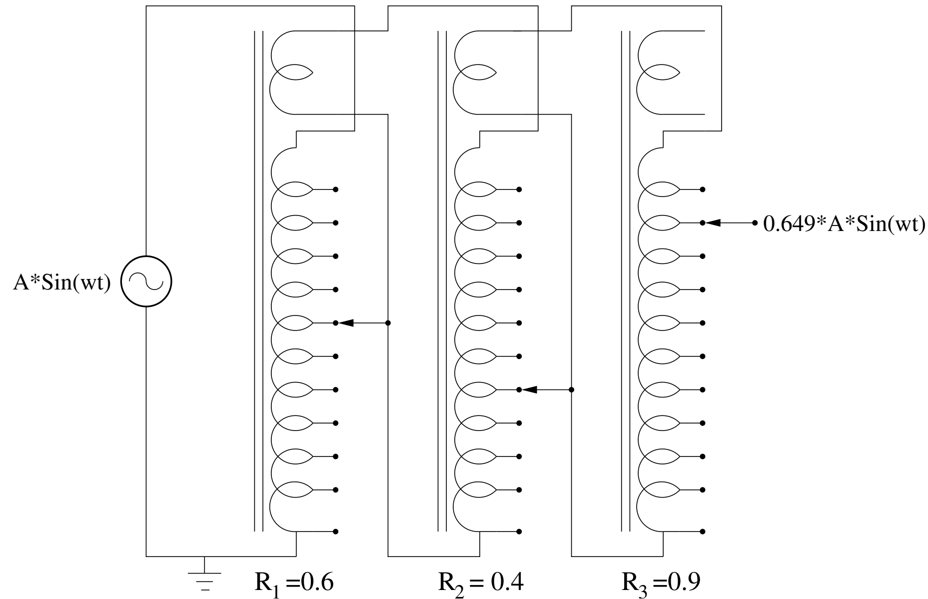

Figure 7.6: Three decade ratio transformer showing connection scheme for cascading multiple decade transformers.

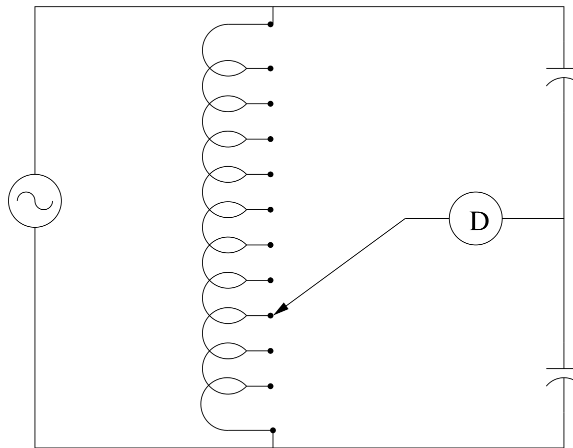

Figure 7.7: Ratio transformer balanced capacitance bridge.

widely used to balance AC bridge circuits. The first commercial bridge that used this type of arrangement was the General Radio 1615-A [6]. This bridge was unparalleled in accuracy because it did not use a variable capacitor to balance the bridge as did most of its predecessors [7]. The approach is limited in accuracy by how well the variable capacitor is calibrated. In addition, variable capacitors are typically air gap capacitors which tend to drift with temperature and humidity changes.

The method of applying a ratio transformer in this research has the configuration shown in Figure 7.7, which is a simplified schematic depiction of the ratio transformer. Although this explicitly shows

only one coil, the experiments employed either a three or seven decade ratio transformer. The two capacitors in Figure 7.7 can either be the two matched sensor capacitors on the chip, or one sensor capacitor and one reference capacitor.

7.4 Capacitance Measurement Circuit Results

To test the ability of a ratio transformer to balance a capacitance bridge, the following experiment was devised. A pair of multiple gap capacitors, and a channel was constructed with three glass microscope slides and aluminum foil. This setup was used to detect the presence of a small ball bearing rolling down the channel.

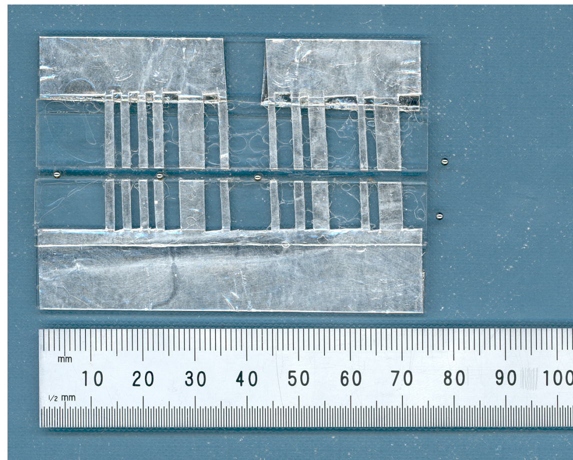

Figure 7.8: Device for testing the capacitance circuit.

The electrodes are made from aluminum foil with an adhesive backing. The aluminum foil is then placed on microscope slides so that the electrode “fingers” wrap around the edge of the slide. One slide was made with two electrically isolated electrodes, the other was made with a single electrode. The “fingers” on both slides were made to line up as closely as possible, as shown in Figure 7.8. These two slides were then glued to a third slide to keep their spacing fixed and to provide a channel for ball bearing travel. The channel was partially filled with silicone oil (Dow Corning type 705) to limit the bearing speed enough to enable accurate correlation of bearing position with signal response. The electrodes were then connected to the measurement setup as shown in Figure 7.9.

In this experiment electrode capacitances were closely matched, so that balancing the bridge with a ratio transformer was not necessary. To demonstrate this, the electrodes were connected to the measurement setup as shown in Figure 7.11.

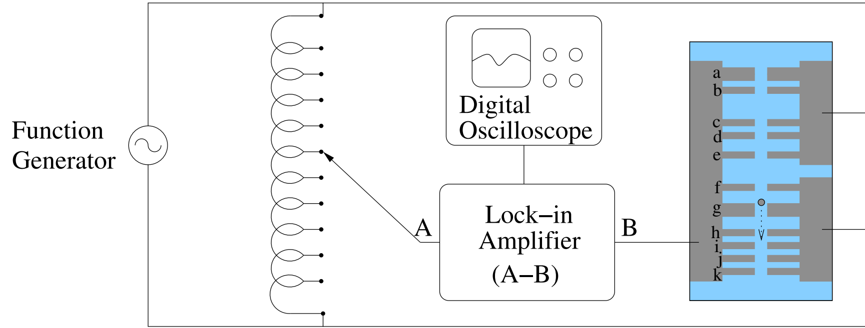

Figure 7.9: Circuit connections for capacitance circuit testing using a precision ratio transformer to balance the AC bridge.

The measurement results from this circuit are shown in Figure 7.10. Note that the signal peak spacing can be compared to the electrode spacing of the device.

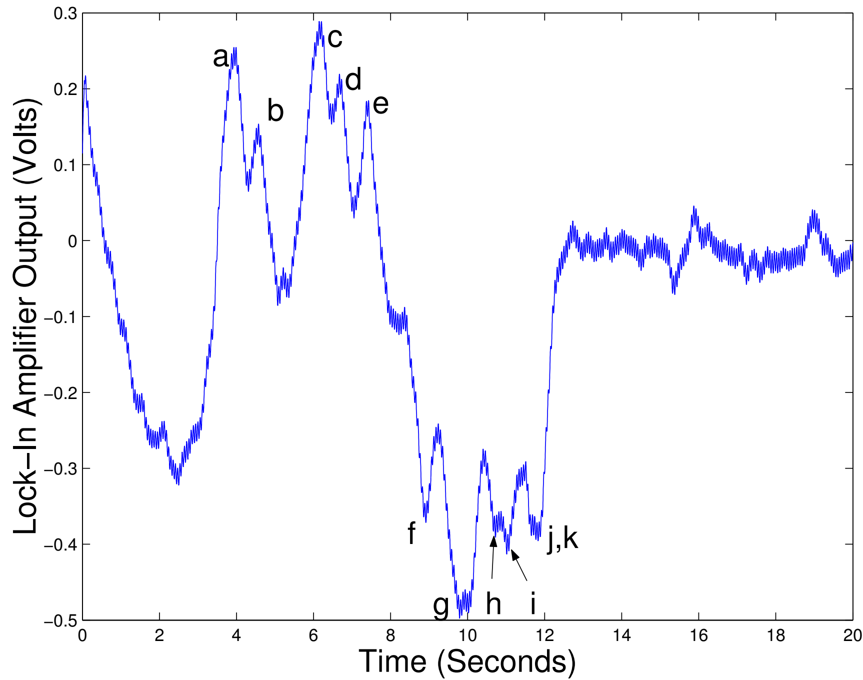

Figure 7.10: Measurement results of circuit in Figure 7.9.

7.5 Nanogap Electrode Measurements of Gold Particles in Solution

Nanogap electrode measurements were performed on nanogap electrodes to test the ability to sense gold particles in solution. Control experiments were first performed using only deionized water. Then a number of dilute suspensions of particles were tested. No technique of driving the fluid, such as electro-osmotic flow, or pressure driven flow were utilized. Particle movement past the electrodes

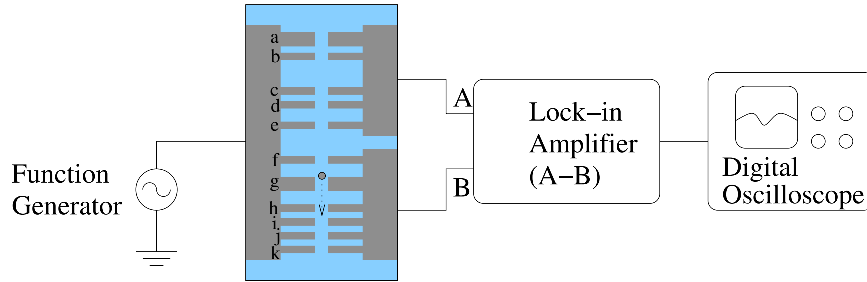

Figure 7.11: Circuit connections for capacitance circuit testing using a half bridge configuration with no means of balancing the bridge.

The measurement results from this circuit are shown in Figure 7.12. Here the signal peak spacing is more clearly defined than in the previous experiment. This circuit contains fewer connecting cables that the previous circuit, and is therefore less susceptible to noise.

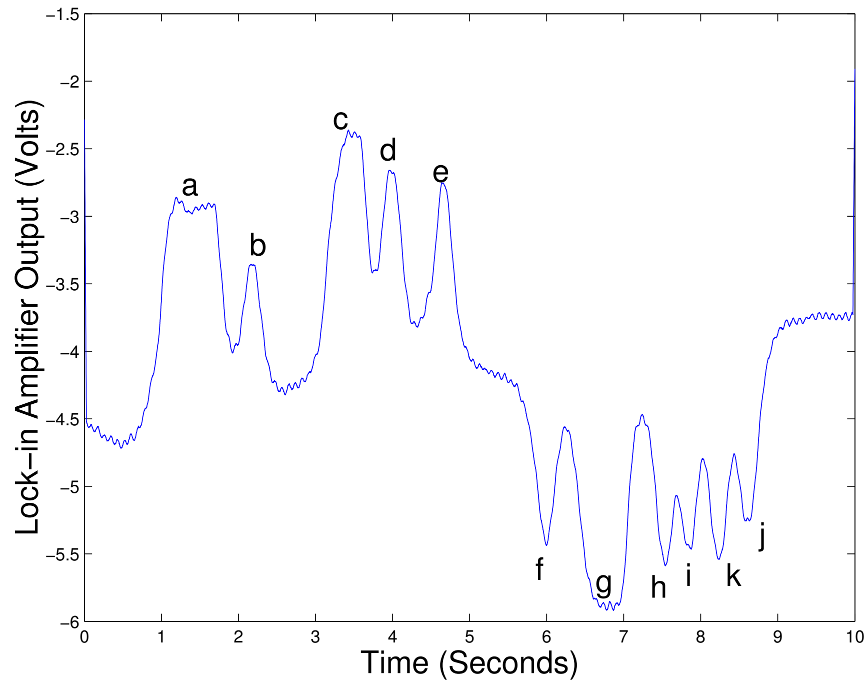

Figure 7.12: Measurement results of circuit in Figure 7.11.

was driven by Brownian motion.

The electrode-channel system used consisted of two channels intersecting at right angles (Figure 7.13). The thermally evaporated electrode metal consisted of 10 nm of chrome and 50 nm of gold. Pattern definition was done with electron-beam lithography on a layer of PMMA covering the metals. After exposing and developing the PMMA, the gold and chrome were etched using ion beam etching. The electrode metal also served as the etch mask for the underlying material. Channels were etched in fused silica substrates. The etching method was reactive ion etching with C_2F_6 as the etch gas.

A small amount of argon was used to improve the etch uniformity by removing any redeposited materials through sputtering. These channels were sealed using a small piece of silicone rubber (PDMS) placed on top of the electrodes. The device was then placed on an electrical probing station and connected as shown in Figure 7.14.

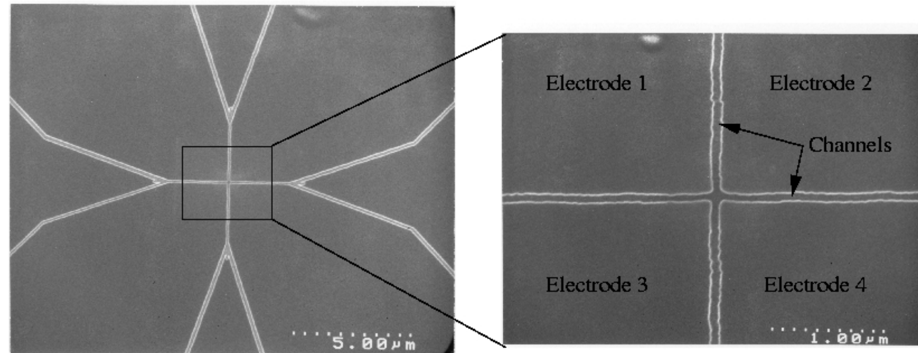

Figure 7.13: Device used to test nanogap electrode sensing of gold particles in solution.

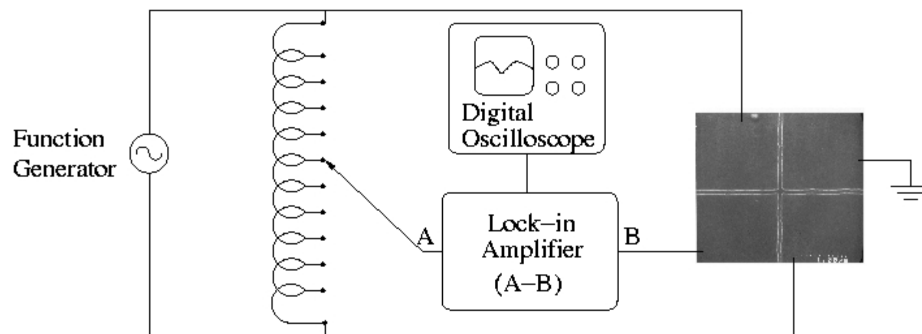

Figure 7.14: Circuit connection for performing measurements on the nanogap electrodes.

Figure 7.15 shows the results of this experiment. In the measurement with 20 nm gold particles present, a number of signal peaks are present with 0.25 to 0.5 second time durations. These could be due to the gold particles passing through the nanogap electrodes.

These measurements show a possible detection of gold particles. However both experiments show a similar slowly varying drift in the background level that make conclusive statements about detecting gold particles difficult. The most likely source of the slowly varying background level is the bridge circuit drifting out of balance. This may be attributed to the test solution seeping into various parts of the device, gradual changes in the electric double layer, or an accumulation of gold particles near the electrodes. While performing these measurements, it was necessary to manually balance the circuit many times each minute.

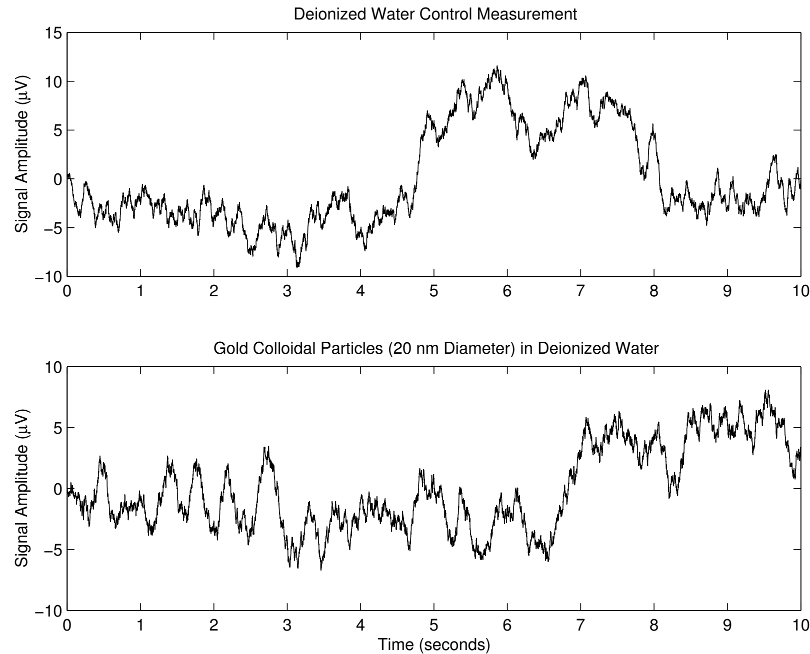

Figure 7.15: Electrical measurement of the nanogap electrodes in Figure 7.13.

In order to improve this type of measurement it will be necessary to design a bridge that will automatically maintain balance of the bridge to compensate for drift. One way to accomplish this is by utilizing a digitally programmable ratio transformer such as the PRT-73 (manufactured by Tegam Inc.) controlled by a low-pass filtered output signal of the lock-in amplifier. An alternative method would be to use voltage controlled capacitors such as varicaps or reverse biased PN-diodes to balance the bridge. Appopriately filtered lock-in amplifier feedback signals would be used to set the bias voltages necessary to maitain bridge balance.

7.6 Conclusion

This chapter discussed several geometrical configurations of nanpgap electrode systems and means of building an electrical circuit to illustrate the measurements possible with these devices. Successful circuits were AC bridge and AC capacitance bridge circuits balanced by a precision ratio transformer. Also discussed as guidance were circuits not recommended for this application, such as charge-discharge technique, oscillator circuit methods and inductive-capacitive resonator circuits. Measurement data obtained with nanopgap electrode systems during this investigation were reported. These included illustration of measurement results that demonstrate using the ratio transformer to balance an AC bridge (Figures 7.9 and 7.10), an example of improving signal clarity by

using matched capacitance electrodes (Figures 7.11 and 7.12), and measurements with gold particles in solution (Figures 7.13, 7.14, 7.15) . The difference in signal quality and signal response detail of deionized water versus gold particles in solution was significant, and is sufficient evidence that these nanogap electrode systems may be the basis for important additional research.

References

[1] S. M. Huang, A. L. Stott, R. G. Green, and M. S. Beck. Electronic transducers for industrial measurement of low value capacitances. *Journal of Physics E: Scientific Instrumentation*, 21, 1988.

[2] Arthur Whitmore Smith, Ph.D. Smith. *Electrical Measurements in Theory and Applications*. McGraw-Hill Book Company, Inc., third edition, 1934.

[3] R. G. Green and J. M. Cunliffe. A frequency-modulated capacitance transducer for on-line measurement of two-component fluid flow. *Measurement*, 1(4):191–195, 1983.

[4] Toshiaki Aoki and Katsumi Yokoi. Calibration of a ratio transformer. In *Proceedings of the NCSL Workshop & Symposium*, pages 701–707, 9-1, Takakura-Cho, Hachioji, Tokyo 192, Japan, 1995. Measurement Standards Center, Hewlett-Packard Japan Ltd.

[5] Prt-73 schematic. Technical report, Tegam, Ten Tegam Way, Geneva, Ohio, 44041.

[6] Massachusetts General Radio Company, West Concord. Capacitance bridge. *The Review of Scientific Instruments*, 33(11), November 1962.

[7] Boonton Electronics Corporation. Capacitance bridge. *The Review of Scientific Instruments*, 30(6), June 1959.

Chapter 8

Conclusions

In summary, this research has investigated methods of fabricating nanofluidic channels in a variety of materials systems. The ability to build sub-micron fluid channels in a variety of polymer materials may become a key part of fluidic analysis systems. Current development of polymers which are electrically and optically active will assist the integration of nanofluidic systems with a variety of analytical techniques.

Miniaturization of nanofluidic based instruments would benefit from a fluid handling system more versatile than pressure based actuation. This research has successfully demonstrated the ability to use electro-osmotic flow in sub-micron channels. This was chosen over the other fluid handling methods discussed because of ease with which this can be integrated with electronic devices.

Development of fabrication methods that allow integration of nanometer sensing electrodes with the fluid channels were demonstrated. Preliminary measurements have shown promising evidence that nanogap electrodes integrated with fluid channels may be capable of detecting the motion of gold particles. In order to verify this with certainty it will be necessary to correlate the electrical measurements with simultaneous optical measurements.

Future work in this area could use more complex electrode geometries in order to multiplex the signals of many individual gaps onto one signal line. Building electrodes with multiple gaps in unique binary code sequences could also be used to improve signal-to-noise ratio by deconvolving the signal with a predetermined function that represents the electrode configuration. The experiment to test the measurement setup anticipated this approach by utilizing electrodes configured in a non-periodic binary pattern (see Figure 7.8). A similar approach is effective for optimizing bandwidth usage, and avoiding problems of multi-path interference in radio communications using code-division multiple-access [1]. Binary coded nanogap electrodes would provide multiple measurements on individual particles, and to track the positions of multiple particles simultaneously.

References

[1] (Guu-Chang) Yang and Wing C. Kwong. *Prime Codes with Applications to CDMA Optical and Wireless Networks.* Mobile Communications Series. Artech House, Boston, London, 2002.